AWARD NUMBER: W81XWH-09-1-0299

TITLE: Photoacoustic Imaging of Epilepsy

PRINCIPAL INVESTIGATOR: Huabei Jiang, Ph.D.

CONTRACTING ORGANIZATION:
University of Florida
Gainesville, FL 32611

REPORT DATE: April 2014

TYPE OF REPORT: Final

PREPARED FOR: U.S. Army Medical Research and Materiel Command
Fort Detrick, Maryland 21702-5012

REPORT DOCUMENTATION PAGE

Form Approved
OMB No. 0704-0188

1. REPORT DATE *(DD-MM-YYYY)*	**2. REPORT TYPE**	**3. DATES COVERED** *(From - To)*
April 2014	Final	1Apr2009-31Mar2014

4. TITLE AND SUBTITLE

Photoacoustic Imaging of Epilepsy

5a. CONTRACT NUMBER

5b. GRANT NUMBER:
W81XWH-09-1-0299

5c. PROGRAM ELEMENT NUMBER

6. AUTHOR(S)

Huabei Jiang, Ph.D.

email: hjiang@bme.ufl.edu

5d. PROJECT NUMBER

5e. TASK NUMBER

5f. WORK UNIT NUMBER

7. PERFORMING ORGANIZATION NAME(S) AND ADDRESS(ES)

University of Florida

Gainesville, FL 32611

8. PERFORMING ORGANIZATION REPORT NUMBER

9. SPONSORING / MONITORING AGENCY NAME(S) AND ADDRESS(ES)

U.S. Army Medical Research
and Materiel Command
Fort Detrick, Maryland

10. SPONSOR/MONITOR'S ACRONYM(S)

11. SPONSOR/MONITOR'S REPORT NUMBER(S)

12. DISTRIBUTION / AVAILABILITY STATEMENT

Approved for public release; distribution unlimited

13. SUPPLEMENTARY NOTES

14. ABSTRACT

This research is aimed at developing a new imaging approach, called "Photoacoustic tomography (PAT)", for non-invasively tracking dynamical changes during seizure occurrence. The project will develop imaging hardware and software, and conduct phantom/in vivo experiments to achieve the proposed goals. We have fulfilled the statement of work proposed. The real-time PAT system completed in Years 1 and 2 provides us a platform for performing the extensive phantom and animal experiments proposed for the coming years. In year 3, we implemented reconstruction codes and we performed simulation and phantom experiments to evaluate the software developments. In year 4, the real-time PAT system constructed in this project coupled with the light-weighted cap interface has provided us a platform for performing extensive animal experiments in freely moving rats. In Year 5 we completed the proposed Tasks 6 and 7 for continuous recording of EEG and PAT over a long period of time to monitor seizure activity continuously to characterize changes during interictal, ictal and post-ictal periods when a spontaneous seizure occurs. We analyzed the images from the in vivo experiments and wrote the final report. We completed any unfinished experimentation during these months such that we have a sufficient number or rats monitored with EEG and PAT to reach statistical significance.

15. SUBJECT TERMS

Photoacoustic imaging, photoacoustic tomography, epilepsy, seizure

16. SECURITY CLASSIFICATION OF:			**17. LIMITATION OF ABSTRACT**	**18. NUMBER OF PAGES**	**19a. NAME OF RESPONSIBLE PERSON**
a. REPORT	**b. ABSTRACT**	**c. THIS PAGE**			USAMRMC
U	U	U	UU	92	**19b. TELEPHONE NUMBER** *(include area code)*

Table of Contents

Introduction

Approximately 2.5 million Americans live with epilepsy and epilepsy-related deficits today, more than disabled by Parkinson disease or brain tumors. The impact of epilepsy in the US is significant with a total cost to the nation for seizures and epilepsy of approximately $12.5 billion. Epilepsy consists of more than 40 clinical syndromes affecting 40 million people worldwide. Approximately 25 percent of individuals receiving antiepileptic medication have inadequate seizure control; however, 80% individuals with medication resistant epilepsy might be cured through surgery if one were able to precisely localize the seizure focus. The proposed research will significantly advance our ability to localize such foci, and thereby offer curative epilepsy surgery for this devastating disease. Photoacoustic tomography (PAT) uniquely combines the high contrast advantage of optical imaging and the high resolution advantage of ultrasound imaging in a single modality. In addition to high resolution structural information, the proposed PAT is also able to provide functional information that are strongly correlated with regional or focal seizure activity, including blood volume and blood oxygenation because of the high sensitivity of optical contrast to oxyhemoglobin and deoxyhemoglobin concentrations. The hypothesis of the proposed research is that PAT offers the possibility to non-invasively track dynamical changes during seizure occurrence. The overall goal of this research is to advance a finite element based photoacoustic tomography method for epilepsy imaging, using both laboratory and in vivo experiments. Specifically, in this project we propose**:** (1) To design, construct and test a transducer array system for both 2D and 3D PAT imaging; (2) To advance reconstruction algorithms and associated image enhancement schemes for quantitative PAT; (3) To evaluate and optimize the integrated functioning of the hardware and software components of the transducer array-based system, using simulation and phantom experiments; (4) To test and validate the PAT system using a well established animal model of temporal lobe epilepsy.

Body

This report describes work accomplished in 4 years (plus 1 year no-cost-extension) of the project. As outlined in the approved Statement of Work (SOW), the tasks during this period of time include: Task 1 (Months 0-24): Purchase and calibrate Ti:Sapphire tunable laser; design and test PVDF transducers; design and test data acquisition subsystem; assemble the entire photoacoustic tomography (PAT) system; Task 2. (Months 18-24) Design, build and test the animal interface Task 3 (Months 0-24): Implement reconstruction codes and associated enhancing schemes including dynamic dual meshing, total variation, advanced regularization techniques, adaptive meshing, initial parameter optimization and reconstruction of absolute optical absorption coefficient for quantitative high resolution functional PAT. Task 4. (Months 12-24) Calibrate the imaging system; conduct simulation and extensive phantom experiments using the system for evaluation of the reconstruction codes and associated enhancements. Task 5. (Months 25-42) Implement reconstruction codes in the areas of advanced boundary conditions, 3D algorithms and parallelization of 3D codes; perform simulation and phantom experiments to evaluate the software developments. Task 6. (Months 25-42) Conduct animal experiments for evaluating the PAT imaging system. Task 7. (Months 43-48) Analysis of the images from the in vivo experiments.

The sections below consist of (1) Hardware development (2) System Development and evaluation (3) Software Development (4) Animal experiments (5) Rat Model of Temporal Lobe Epilepsy (6) Analysis of the images from the in vivo experiments that reflect the tasks associated with the SOW during Months 0-48.

1. Hardware Development (Task 1)

We have completed the design of the proposed array based PAT system based on the extensive modeling and testing of the key components needed for the proposed system using the existing single transducer scanning system.

In Fig. 1a, the designing work for an array based PAT system is shown.

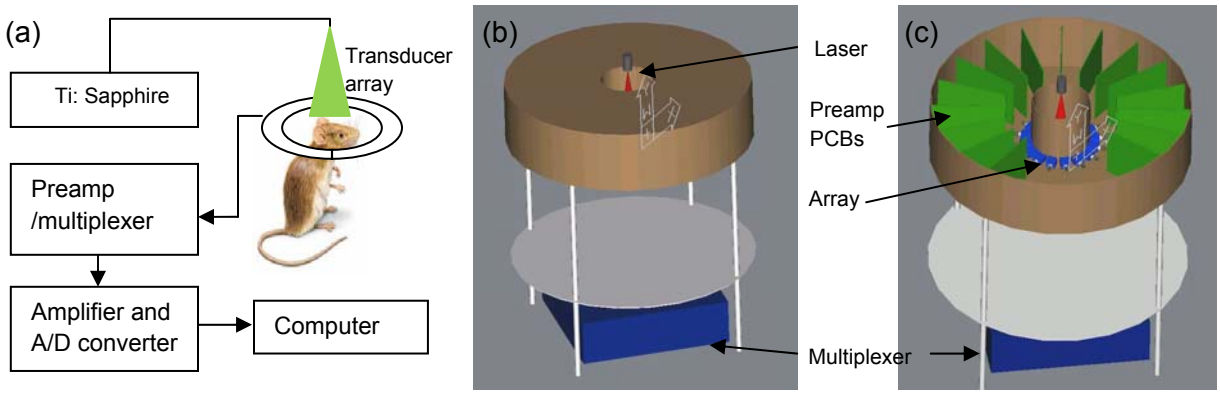

Fig. 1 (a) Schematic of the PAT system. (b) and (c): 3D display of the system/measurement chamber with (b) and without (c) the top covered.

Accomplished goals in the first year of the project are summarized as follows:

1. We completed the design for an array based PAT system, which is the most important part of Task 1.
2. We developed three novel schemes that can enhance our current reconstruction software.
3. We conducted phantom experiments that confirmed our software enhancement.

For more details please see the full progress report of the first year.

2. System Development and Evaluation (Tasks 1, 2, 3 and 4)

In the second year, we achieved the following goals:

1. We have completed the construction of the proposed an array based real-time PAT system, and calibrated and tested the system using extensive phantom experiments.
2. We have built the animal interface and successfully tested it for *in vivo* imaging of rat brain.
3. We have conducted phantom experiments that confirmed our software enhancement.

Figs. 2a and 2b show the photograph of the completed PAT system. As shown in Fig. 2a, a tunable Ti:Sapphire laser (part A) is used to provide 690-950nm near- infrared (NIR) laser pulses with a full-width half-maximum (FWHM) value of 8-25ns pulse width with a repetition rate of 10Hz for generating photoacoustic signals. The 5 MHz full-ring transducer array (part B) is used for recording the photoacoustic signals. A home made pre- amplifier (part C) receives the signals from the transducers and transmitted the amplified signals to A/D board (part D) which are then stored in the computer (part E).

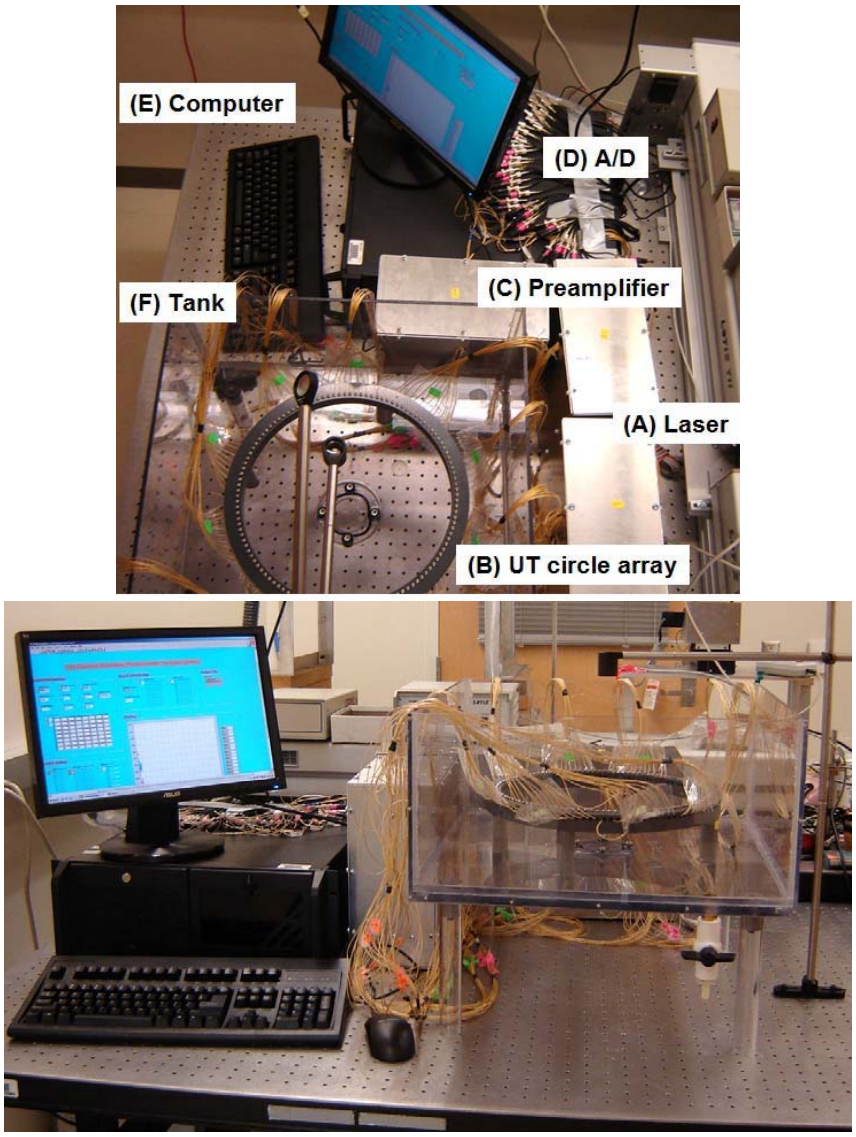

Fig. 2. Photograph of the real-time PAT system. (a): Top view. (b): Front view.

We have made a significant progress that has fulfilled the statement of work proposed for Year 2 of this project. The real-time PAT system completed in Years 1 and 2 provides us a platform for performing the extensive phantom and animal experiments proposed for the coming years.

In Task 3, we implemented 6 image enhancement schemes. In Year 1, 3 schemes including total variation (TV), advanced regularization techniques, and adaptive meshing were developed successfully. In Year 2, the remaining 3 schemes, including dynamic dual meshing, initial parameter optimization, and reconstruction of absolute optical absorption coefficient for quantitative high resolution functional PAT have been implemented as proposed.

For more details please see the full progress report of the second year.

3. Software Development (Task 5)

We have completed the software development proposed for Year 3 including advanced

boundary conditions, 3D algorithms, parallelization of 3D codes, and their testing using simulation and phantom experiments.

4. Animal Experiments (Task 6)

In Year 3 we conducted extensive animal experiments to evaluate the PAT system constructed in Years 1 and 2. We were able to image the functional anatomy of a focal seizure noninvasively and in real time at a spatial resolution of ~150μm (Figs. 3).
In this real time PAT system (**Fig. 3a**), light from a Ti: Sapphire laser tunable from 690 to 950 nm was delivered to the cortical brain surface through an optical fiber. Part of the energy of each laser pulse was detected by a photodiode for calibration. A 192-element full-ring transducer array was used to capture the photoacoustic signals generated by the laser light. All the 192 channels were equipped with preamplifiers and secondary stage amplifiers for optimized signal-to-noise ratio. A 3:1 electronic multiplexer coupled with 64-channel analog-to-digital converters completed the 192-channel data acquisition, providing an imaging speed of 0.33 s/frame primarily limited by the 10 Hz laser repetition. The spatial resolution of PAT is inversely related to the bandwidth of the ultrasonic transducer. In our PAT system each ultrasonic detector had a 5 MHz central frequency, a 70% nominal bandwidth, and a diameter of 6 mm (Blatek, Inc., PA, USA), resulting in a spatial resolution of 150μm.

We first tested the PAT system accuracy by imaging a living rat brain with both the scalp and skull intact. Results indicate that the noninvasive PAT image of the rat cortical vasculature correlated with the anatomical location of each vessel (**Figs. 38b, c**).

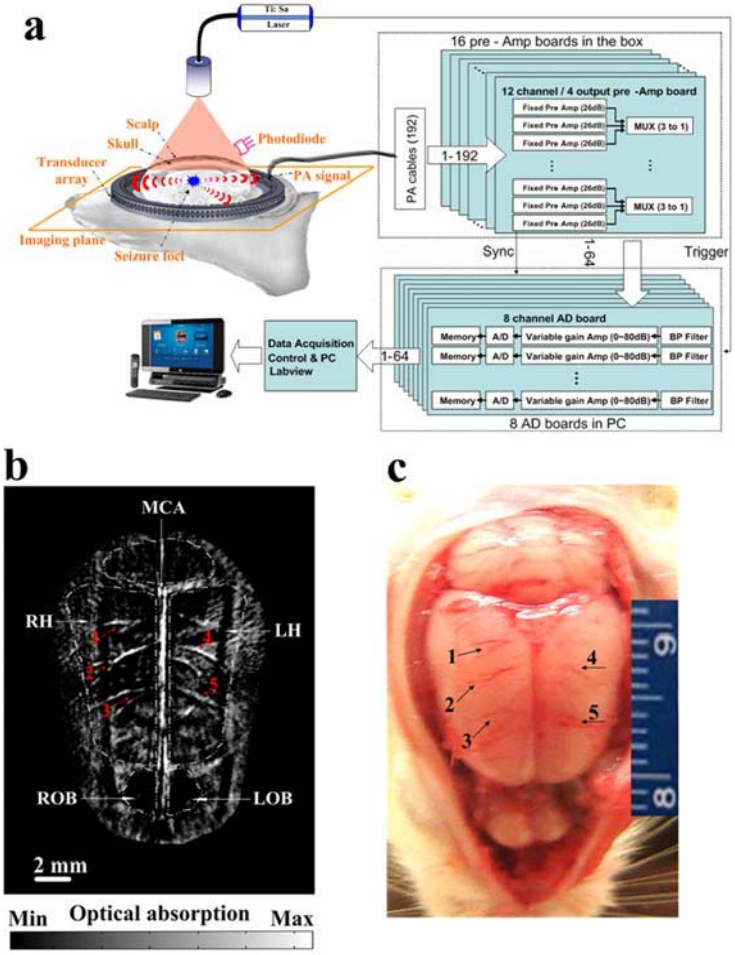

Figure 3 Real-time PAT system for seizure dynamics. (a) Schematic of the real-time PAT system. A 192-element full-ring transducer array was used to capture the PA signal during seizure onset. **(b)** Noninvasive PAT imaging of a rat brain *in vivo* with the skin and skull intact. MCA, middle cerebral artery; RH, right hemispheres; LH, left hemispheres; LOB, left olfactory bulbs; ROB, Right olfactory bulbs. **(c)** Open-skull photograph of the rat brain surface acquired after the PAT experiment. Numbers 1–5 indicate the corresponding blood vessels in the PAT image and rat brain photograph.

Accomplished goals in the third year of the project are summarized as follows:

1. We have developed the advanced boundary conditions scheme, and implemented the 3D reconstruction codes and their parallelization which allowed efficient high performance PAT image reconstruction.
2. We have conducted simulation and phantom experiments that confirmed our software enhancement.
3. We have performed extensive *in vivo* experiments using the rat epilepsy model to evaluate the PAT system we developed in this project. The results show that we were able to image the functional anatomy of epileptic foci noninvasively and in real time at a spatial resolution of ~150μm.

For more details please see the progress report of the third year of the project.

5. **Rat Model of Temporal Lobe Epilepsy (Task 6)**
   During months 37-48 of this project, we have successfully developed and validated the rat model of temporal lobe epilepsy.

Accomplished goals in the fourth year of the project are summarized as follows:

1. We have developed and validated a rat model of temporal lobe epilepsy.
2. We have performed extensive *in vivo* experiments to achieve concurrent EEG and PAT recordings. Interesting results are obtained that may be significant for seizure prediction and for neurovascular coupling studies.
3. We have designed and constructed a light-weighted animal/transducer interface that can be used for chronic monitoring of freely moving animals.

After many trials and errors in Year 4, we have successfully fabricated such light-weighted transducer array (PVDF film transducers) and light delivery subsystem (plastic based light delivery). As shown in Fig. 4, a cap interface firmly attached to the rat head will allow us to chronically monitor seizure activity in freely moving rat. The cap interface weights only ~7g in total (see Fig. 10b). In Year 5 of the project (i.e., 12-month no-cost-extension), this light-weighted cap interface coupled with all other preparations described in this report will allow us to complete the proposed Tasks 6 and 7.

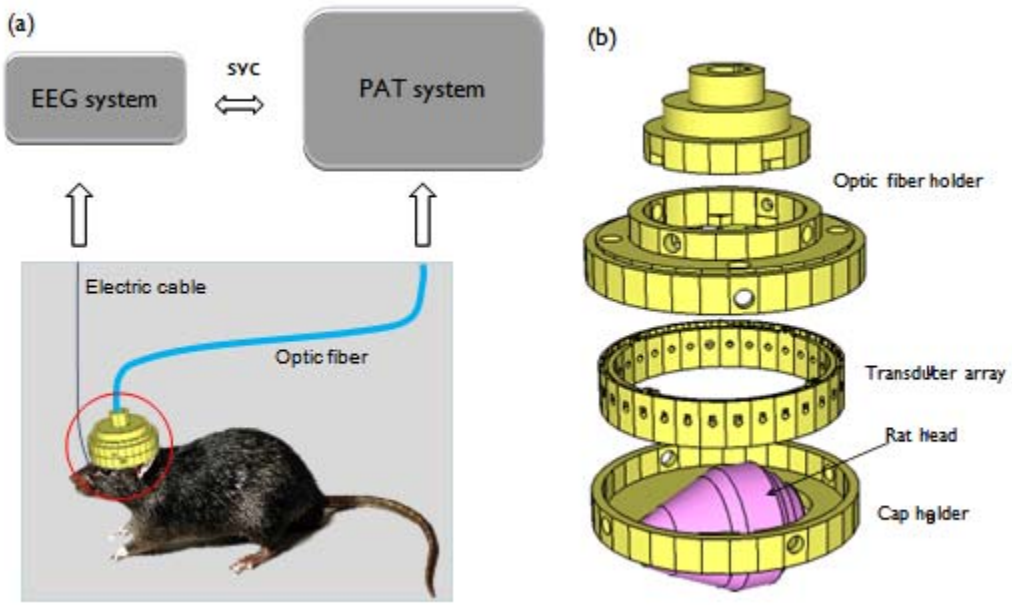

Fig. 4 (a) PAT/EEG system/cap interface for chronic monitoring/imaging of freely moving rats. (b) Schematic detail of the cap interface

For more details please see the progress report of the fourth year of the project.

6. Analysis of the images from the in vivo experiments (Task 7)

In this section, the accomplished goals in the year 5 of the project are presented in details.

6.1. Experimental setup

The main feature of the photoacoustic system is the sparse spherical array which is consisted of 192 discrete transducers, as shown in Fig. 5. The transducers were mounted on a custom fabricated white ABS spherical interface with a distance of 71.6mm from the center of the array, and formed into seven layers. Each transducer had a central frequency of 5MHz and a reception bandwidth of greater than 80%, resulting in an almost isotropic spatial resolution about 0.2mm. The active area of the transducer was 3mm in diameter, and the angular acceptance was about 15 degree. The signal from the 192 transducers was amplified by 16 homemade preamplifier boards and coupled into a 64 channel parallel data acquisition system with 3:1 multiplexing, as indicated with three different colors.

Rats were elevated to the center of the spherical interface through a chamber fixed at the tank bottom, whose top was about 15 mm beneath the interface center, and a transparent plastic wrap was used to cover the chamber top. The spherical transducer array was placed in the water bath, acoustically coupled to the rat head with ultrasound gel. Laser beam was delivered through a concave lens resulting a homogenously illumination on the rat head. In this study, two wavelengths of 1064nm and 710nm were used. The 1064nm light was from a Q-switched Nd:YAG laser, and the 710nm light was from a tunable Ti:sapphire laser. The light intensity on the rat head was about 50mJ/cm2 for 1064nm, and 4mJ/cm2 for 710nm, all below the ANSI exposure limits (ANSI Z136). Both the two lasers operate at 10Hz, so that one complete set of 3D PAT data can be recorded in 0.33s.

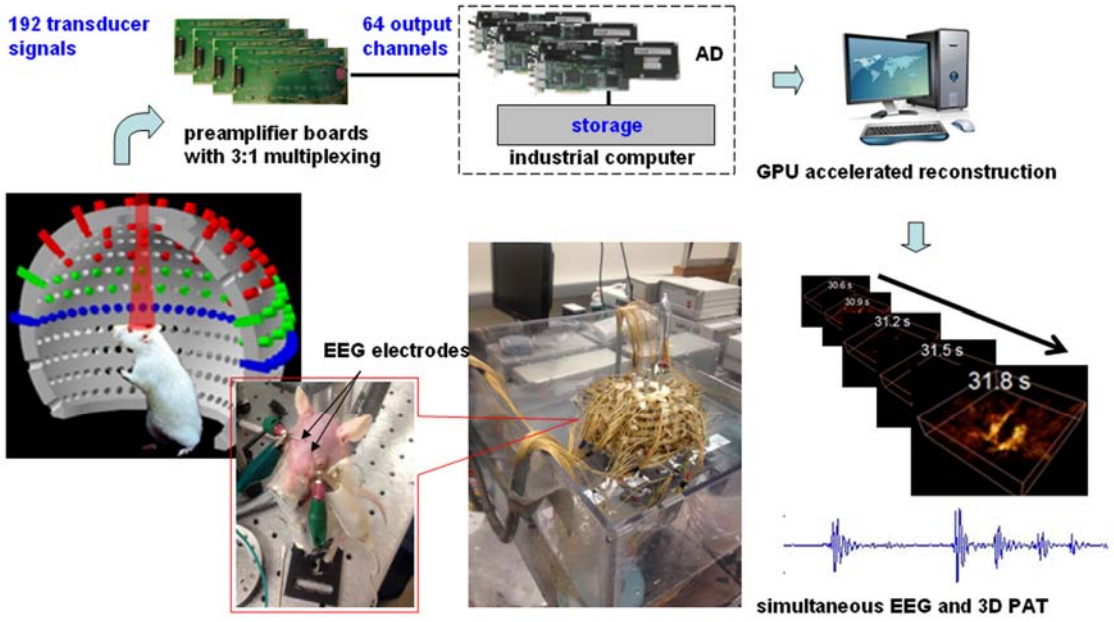

Fig. 5 Experimental setup of the combined system. The anaesthetized rat was elevated to the center of the spherical transducer array for simultaneous PAT and EEG recording. The 192-channel signals were collected and multiplexed with 3:1 into a 64 channel DAQ system, and with a 10Hz laser, a frame rate of 3.3f/s is achieved. Then the collected data is stored for later GPU accelerated reconstruction using 3D delay&sum code ;

Two syringe needles were inserted about 2mm into the front cortex of rat brain served as EEG electrodes. One electrode was chosen as reference and ground, while the other one was used as signal channel. The EEG signal was amplified (RA16PA, TDtucker-Davis Tech.) and recorded (RZ5 Bioamp Processor, TDtucker-Davis Tech.) with a sampling rate about 50kHz. Both the two electrodes were firmly glued on the rat head and the EEG cable was tightly tied on the animal holder to avoid noise induced by any possible unnecessary movement of the operators. The PAT system gave synchronize signal to the EEG system for synchronization.

6.2 Animal preparation

Two groups of rat experiments (n=16 rats, about 35~45g, with 8 rats for 1064nm and the other 8 rats for 710nm) were carried out. The rats were firstly anaesthetized with about 0.25ml Urethane (0.25g/mL) and the hair on the top head was shaven. A syringe containing 0.04g/ml pentyienetetrazole (PTZ) with a scalp needle was inserted in the rat abdomen and fixed with glue. This was to easy the intraperitoneal injection later in the experiment, which has already been established. The rat was immobilized on a custom made plastic holder with ear bar using glue tapes. Two EEG electrodes were inserted, and then the rat was elevated into the center of the spherical transducer array. The seizure process was recorded for 25min, and PTZ was administrated with a dose of 0.5mL at 5min. The injection of the drug lasted about 30s. All rats kept alive through the whole data recording process. All the animal procedures performed were in accordance with the approved University of Florida IACUC protocols.

6.3 Data processing

With a frame rate of 3.3f/s, there were 5000 complete sets of PAT data for the 25min experimental time. Before doing 3D reconstruction and processing, 2D time series images were reconstructed with the signals from the 64 transducers in the lowest layer of the array, which were indicated with blue in Fig.5. Then all 2D time series were first screened for movement artifacts using a movie function, although rats were completely paralyzed during experiments. In our experiments, only 3 out of 8 rats for the 1064nm didn't satisfy this condition, while all the 8 rats for 710nm were quantified. Then 3D images were reconstructed using 3D delay&sum algorithm, which was accelerated by GPU parallel technique. The resulted 3D images had a voxel number of 201×201×101 representing a 10×10×5mm volume, and the negative voxel values were set to zero. The reconstruction speed is about 0.97s for one frame. Amira (from Visage Imaging, Inc.) was used to render the 3D images.

There were two sources of noise in the EEG signal, a strong sharp 10Hz noise from the Q-switch of the laser, and the 60Hz alternating current noise. For de-noising, the data deteriorated by the Q-switch was replaced with adjacent data, and the 60Hz alternating current noise is removed by filtering out 58-62Hz in frequency domain (Fig. 6 b). Then the EEG data was applied with a low pass filter of 100Hz, and transformed into a 300000 point signal for the 25min EEG recording, corresponding to sampling rate of 200Hz.

6.4 Neurovascular coupling study

Because the 1064nm and 710nm light were mainly absorbed by oxy-hemoglobin (HbO2) and deoxy-hemoglobin (Hbr) in the tissue respectively, with reasonable approximations the PAT signals from them can be taken as the total volume change of those two absorbers. For neurovascular coupling study, averaged signals from specific anatomical regions of interest

(ROI) are compared to that from the superior sagittal sinus (SSS) as well as the EEG signal. The PAT signals were expressed as the percentage changes from the baseline, which is defined to be the average value over first 4min of the recording. Next, we further investigated the correlation relationship between these signals. We also calculated the correlation coefficient of every voxel with the SSS, and got the negative correlation map following the seizure onset to identify important regions in the brain. We choose the PAT signal from the SSS because it's well distinguished in the reconstructed 3D images and has the highest SNR. In this step, the reconstructed 3D image was applied with a moving window of 9-voxel wide cube for averaging to improve the low SNR due to the limited number of transducers. Finally, the granger causality networks between the SSS, hippocampus, and cortex at different times were calculated. All the acquired results were examined by experts in the neurology.

6.5 Results

The EEG signal was stable before the drug injection. Ictal discharges were induced shortly after the injection of PTZ, which were characterized by the low-amplitude fast activity with high amplitude (Fig. 6 A). The epileptic pattern progressively increased in amplitude in the following 2 to 3 minutes. As the seizure evolves, it gradually turned into clonic paroxysmal discharges of lower frequency. 2D plot of the time-frequency power map of the EEG signal shows that a mixture of lower signal frequency particularly in 1–3 Hz was seen throughout the seizure, and

higher frequency power components (up to ~4–6 Hz) were stronger early in the seizure and

gradually decreased in power (Fig. 6 B). This is close to results in other publications. Seizures were induced successfully in all the 16 rats, and they were similar in the shape and amplitude. The injection time is easily distinguished as isolated high amplitude spikes around 5min in the EEG signal.

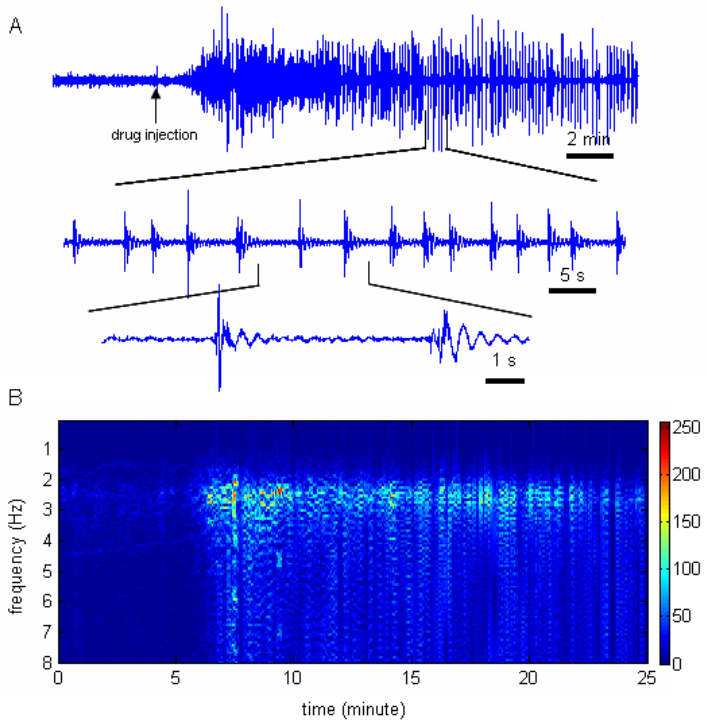

Fig. 6 Electrophysiology of PTZ induced seizure. (a) An example of EEG traces. The arrow highlights the time of PTZ injection. The seizure always starts with synchronized high-frequency oscillations that increase in amplitude, progressing into clonic paroxysmal discharges of lower frequency afterwards. (b) Time-frequency analysis for the same EEG signal above. Analysis was performed using a short-time Fourier transform. Peak power was normalized to 1. The dominant ictal signal frequency was 1–3 Hz. Higher frequency components up to 6 Hz occurred earlier in seizure and diminished in power gradually.

6.6 PAT image reconstruction

Representative 3D images for the HbO2 and Hbr are displayed in Fig. 7A and B compared with a photo of the rat brain in Fig. 7 C. Although the image quality is not excellent due to the limited transducer numbers, the SSS and the transverse sinuses (TS) are clearly reconstructed. It's also noted that in the 3D image of HbO2 the Ostia end of the straight sinus (SS) which is below the SSS in z direction can also be seen. The SNR of the 3D image for Hbr is not as good as that for HbO2 partly due to relatively low laser intensity, and the other reason lies in the fact that the concentration of Hb is much lower than that of HbO2 in the blood vessels.

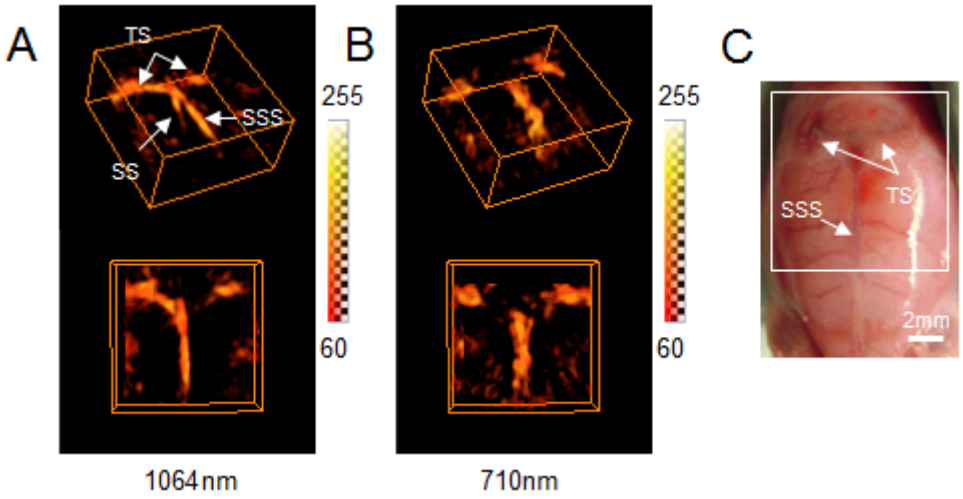

Fig. 7 The reconstruction of 3D PAT images. (A) and (B) show the representative 3D images for HbO2 and Hbr in different views respectively. The image domain is 10×10×5mm containing 201×201×101 pixels. Thresholds and colorbars are presented for the 3D images. (b) Photography of rat head with hair removed. Scale bar represents 2mm. The SSS and TS are well distinguished in both the HbO2 and Hbr images, and the Ostia end of the inferior sagittal sinus can also be seen in the HbO2 image.

6.7 Neurovascular coupling in selective regions

To investigate the hymodynamic changes during the seizure initiation and evolution, regions of interest (ROI) are selected for the SSS, as well as other regions near the hippocampus and the cortex in the brain that are reported to have high gamma-aminobutyric acid (GABA) receptor concentrations (Fig. 8 and 9). ROI was also chosen in the upper posterior region in the reconstruction domain, which contained no tissue of the rat served as reference. With a high frame rate of 3.3f/s, the rapid hemodynamic changes in these regions \can be captured photoacoustically. Taking the SSS and TS as positioning references, it's easy to overlay the maximum amplitude projection (MAP) PAT vascular structural images precisely onto the high resolution anatomical MRI slices of the rat brain obtained from online database .

Fig. 8 shows the averaged HbO2 signals of the ROIs during the seizure, with corresponding EEG signal presented to confirm the onset, duration, and morphology of the seizure. The HbO2 signals are converted into the relative percentage change to the baseline. Because the SSS has the highest SNR in the reconstructed 3D images, the SD for SSS is much higher than the other three signals. The HbO2 signals and the EEG signal are mutually well correlated. All the HbO2 signals of the SSS, hippocampus and cortex remained quite still at first. We can largely divide the change of these three signals after the injection of PTZ into three for stages, which is

indicated in Fig. 8 B. We can see that there was an ‘epileptic dip’ in the SSS at the seizure initiation, and a prominent increase of HbO2 was shown in the hippocampus at the same time which was probably induced by the dilation of the arteries. It’s also seen that the change of hippocampus is largely negatively correlated with the SSS, while the cortex and the SSS are positive correlated. In the third stage, both the HbO2 and Hbr signals in the SSS and cortex dropped, while the increase of HbO2 in the hippocampus sustained through the whole experiment. Comparably, the reference signal remains the same all although the experiment.

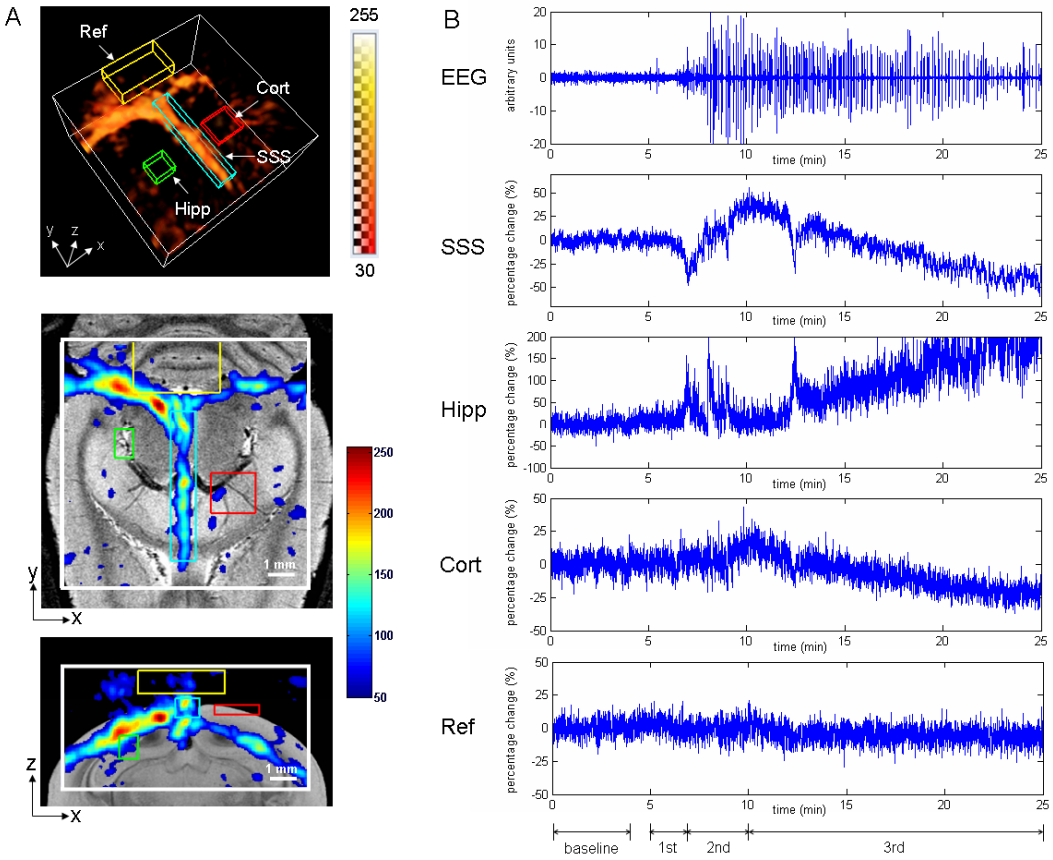

Fig. 8 The HbO2 changes of the SSS, hippocampus and cortex. (A) 3D vascular images of the rat brain (a1) and the MAP vascular structural images (a2 and a3 in the x-y and x-z plane respectively) overlaid on the MRI anatomical images using 1064nm. The ROIs for the SSS, hippocampus, cortex, and the reference are indicated. Thresholds, colorbars, and scale bar are presented. (B) The HbO2 changes of the SSS, hippocampus, cortex and the reference as well as the corresponding EEG signal. The changes of the HbO2 signals are expressed in percentage relative to the baseline, which is defined as the first four minutes of the recording. The changes of these HbO2 signals after the PTZ injection are divided into three stages, as indicated.

Fig. 9 presents result in another rat showing how the changes of Hbr in the SSS, hippocampus, cortex and the EEG signal are mutually correlated. The sizes and the relative positions of the three ROIs are defined to be the same as those in Fig. 8A. The EEG signal here looked almost the same in pattern with that in Fig. 8 B, indicating that our PTZ induced generalized seizure modal was quite stable and the drug administration was well controlled, so that results in Fig. 8 and Fig. 9 were comparable. We also divided the timecourse of the Hbr changes into the three stages with the exact timing as that in Fig. 8 for easy comparison. Although with a relatively low SNR, we clearly see that the decrease of Hbr in the SSS lagged the notable 'epileptic dip' in the SSS shown in Fig. 8 B. In addition, there was a slightly decrease of Hbr in the hippocampus followed by an increase in the first and second stages, but these changes were not as notable as the increase of HbO2 in the hippocampus at the same time in Fig. 8 B. In general, the Hbr signals for the hippocampus and cortex were generally the same in shape, which were negatively correlated with the Hbr of SSS.

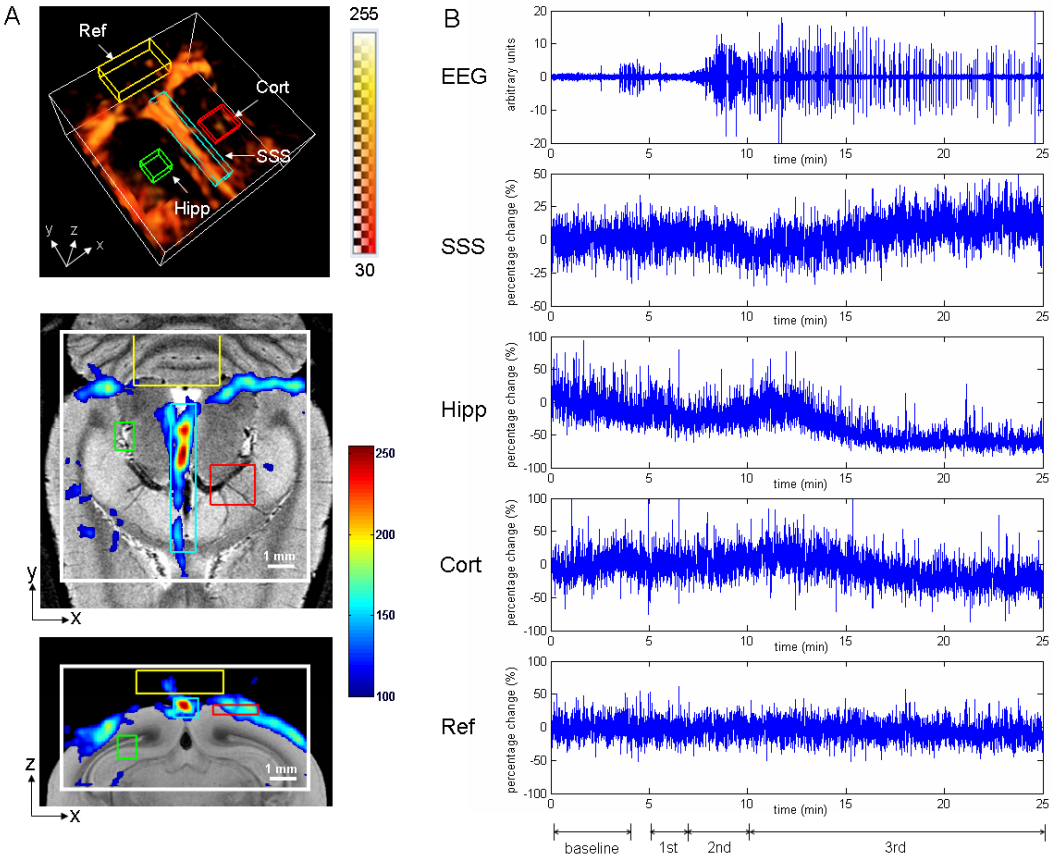

Fig. 9 The Hbr changes of the SSS, hippocampus and cortex. (A) 3D vascular images of the rat brain (a1) and the MAP vascular structural images (a2 and a3 in the x-y and x-z plane respectively) overlaid on the MRI anatomical images using 710nm. The ROIs for the SSS, hippocampus, cortex, and the reference are indicated. Thresholds,

colorbars, and scale bar are presented. (B) The HbO2 changes of the SSS, hippocampus, cortex and the reference as well as the corresponding EEG signal. The changes of the Hbr signals are expressed in percentage relative to the baseline, which is defined as the first four minutes of the recording. The changes of these HbO2 signals after the PTZ injection are also divided into three stages with the same timing as that in Fig. 4B, as indicated.

Fig. 10 shows the statistical results of the HbO2 and Hbr changes across all the rat experiments, which are similar to those in Fig. 8 and 9. The average signal in each rat is calculated every 30 seconds, and then further averaged between different rats, and the corresponding SD is calculated and shown.

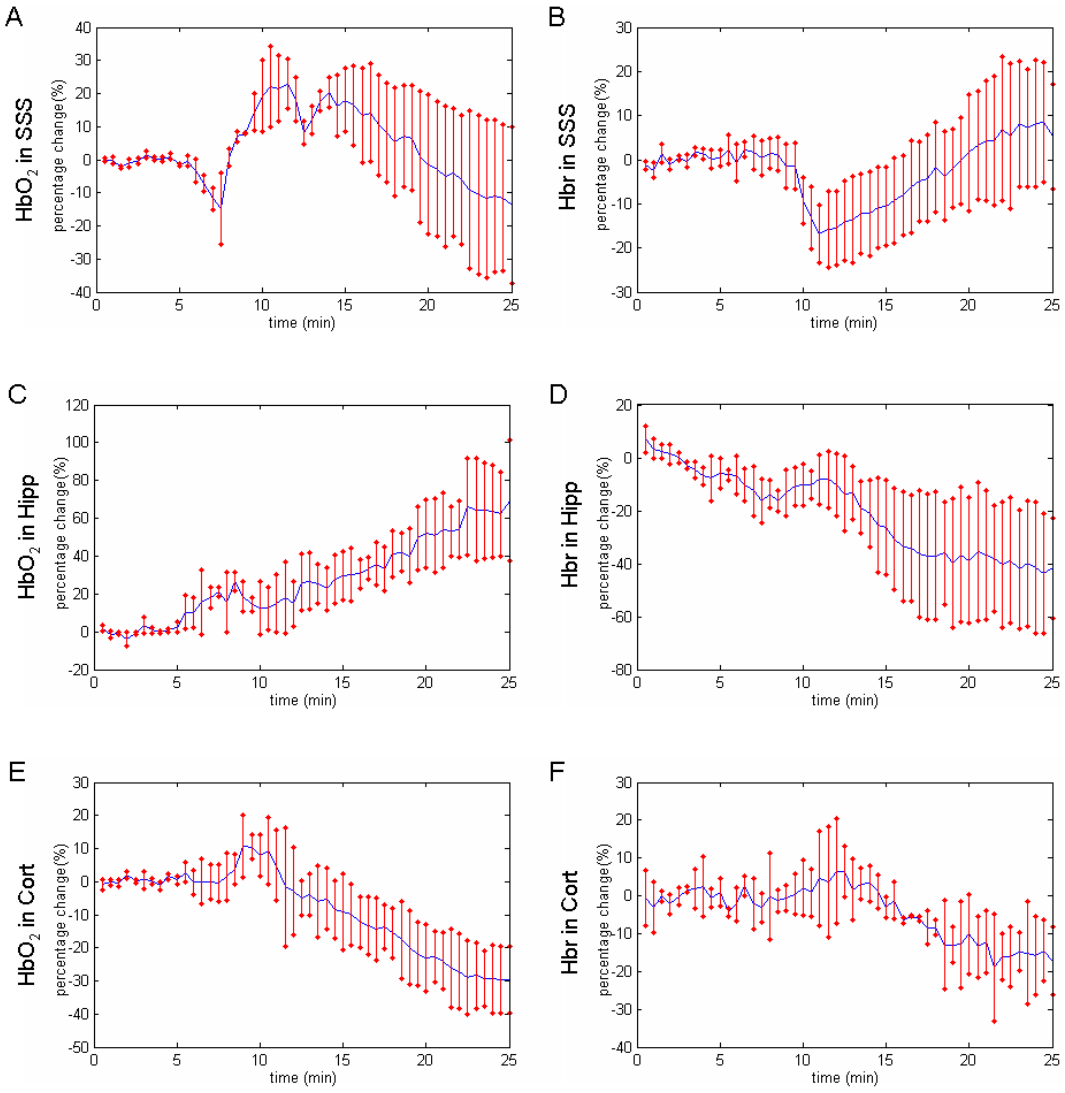

Fig. 10 The average HbO2 and Hbr changes of the SSS, hippocampus and cortex across all the rats. The signals are averaged every 30 seconds, and corresponding SD between different rats are also calculated and shown (in red). (A)

and (B), HbO2 and Hbr changes of the SSS; (C) and (D) HbO2 and Hbr changes of the hippocampus; (E) and (F) HbO2 and Hbr changes of the cortex.

6.8 Correlation analysis and hyper-oxygenation localization

Based on the above results, the hippocampus showed strong hyperfusion and hyperoxgenation during the seizure, and the HbO2 change of it was inversely related with that of the SSS. Fig. 11 A shows the time change of the correlation coefficient between the HbO2 signals of these two regions, and it's found that this value was positive before the drug injection (Fig. 11B), but it turned negative for most of the time after the seizure onset (Fig. 11C). All the correlation coefficients in this paper were calculated in a short time window of 1min.

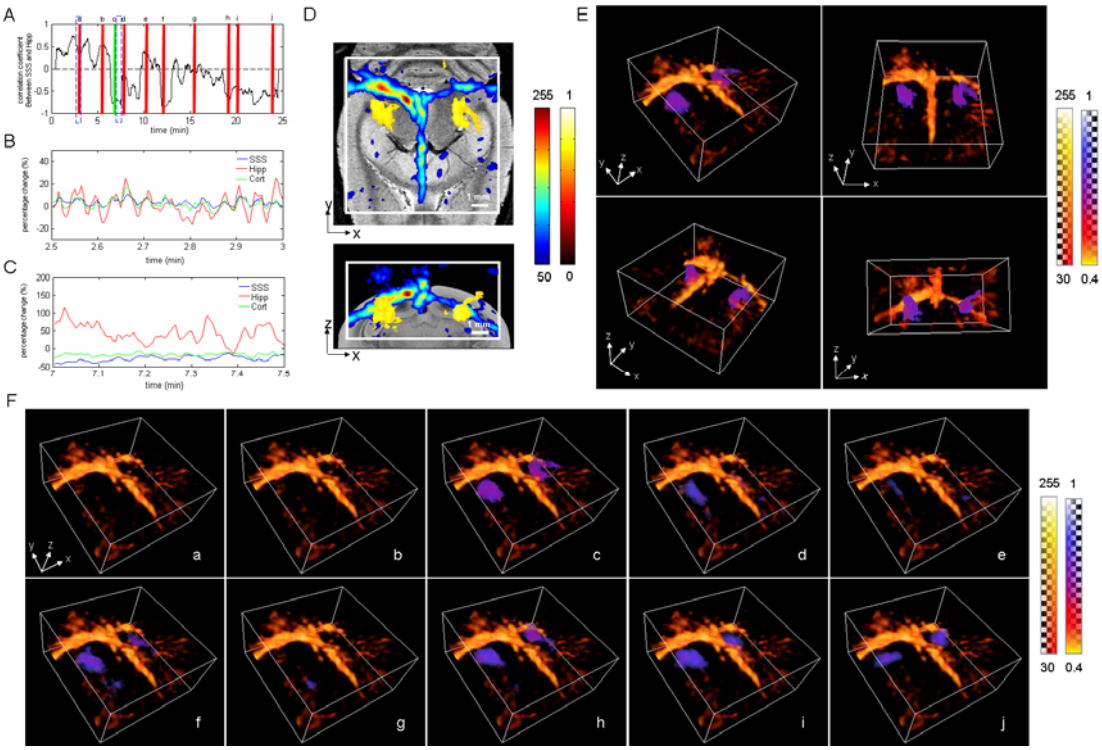

Fig. 11 Correlation study of the HbO2 signals. (A) The time change of the correlation coefficient between the hippocampus and SSS. (B) and (C) the HbO2 signal changes of the SSS, hippocampus and cortex at two different time window as indicated in A with blue rectangles. (D) The 3D negative correlation coefficient map at the time of the green vertical bar in A, shown in different views, and the MAP images of it in the x-y and x-z plane imposed on the corresponding MAP HbO2 vascular images and the MRI anatomical images. (E) The 3D negative correlation coefficient map at different times as indicated in A with vertical bars. The threshold for the negative correlation map is chosen to be 0.6 in D, and 0.4 in E and F. It's seen that the negative correlation voxel with the SSS for HbO2 didn't shown before the drug injection, and were concentrated in the hippocampus and its surroundings after the seizure initiation.

For further investigation, we calculated the 3D HbO2 negative correlation coefficient map between every voxel and the SSS (Fig. 11 D and E). In this step, the 3D HbO2 images were firstly smoothed with a moving window of a 9-voxel wide cube to improve the SNR. Fig. 11 D presents the 3D negative correlation coefficient map at different times, as indicated in Fig. 11 A with vertical red lines. Fig. 11 E shows the same result as Fig. 7 D (e), but from different views, along with the MAP images of it in the x-y and x-z planes coregistered with the corresponding MAP HbO2 vascular structural images, and the MRI anatomical images. We found that voxel with high negative coefficient (with a threshold of 0.7) were hardly found before the drug injection, but they began to show and concentrated in regions around the hippocampus after the seizure onset, although asymmetry is present in these images (Fig. 11E). Especially, when the seizure just began later in the first stage of the seizure (around 6-7min), the HbO2 signal in the hippocampus was correlated with that of the SSS with a large negative correlation coefficient, so that the 3D negative correlation map is preventative at this time (Fig. 11 D). We also calculated the negative correlation maps of HbO2 in other rat experiments, and similar results were obtained (Fig. 12). In summery, voxel with high negative correlation coefficient began to show after the seizure initiation in the hippocampus and its surroundings, which indicates that the hippocampus seemed to be more sensitive in this intraperitoneal PTZ seizure model. This also implies that this method may be of great help for seizure localization especially in generalized seizure cases where fMRI is of less help.

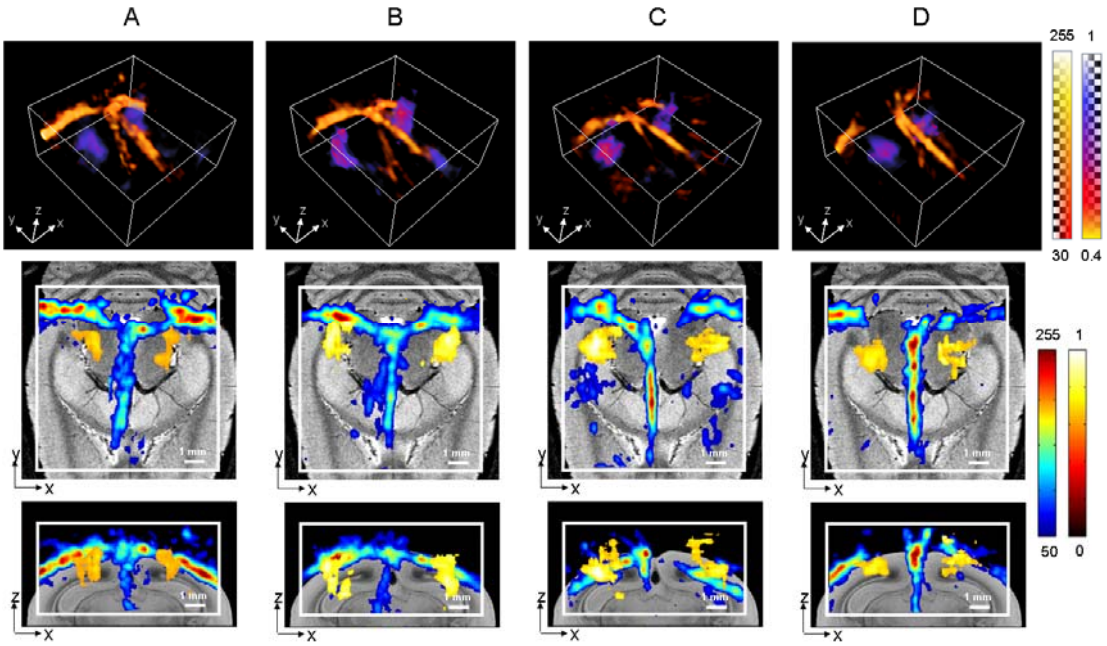

Fig. 12 Negative correlation map of HbO2 in different rats. The time window for generating the correlation map is chosen to be from 6min to 7min. The results are presented in 2D maps, which are imposed on the corresponding

MAP HbO2 vascular images and the MRI anatomical images in x-y and x-z planes, and also presented in 3D images, which are coregistered with the 3D vascular images. The threshold for the negative correlation map is chosen to be 0.6 in the 2D images, and 0.4 in the 3D images. (A)-(D) represent the results for different rats.

6.9 Granger causality analysis

In Fig. 11 B and C, we see that the hemodynamic coupling of the high frequency fluctuations between different brain regions is different with different times. This implies that the high 'noise' component of the PAT signals actually contains rich seizure relevant information that can not be inferred from the overall trend. We applied short time window spectral pairwise granger causality method to identify the functional interaction among the SSS, hippocampus and cortex during the seizure process. Granger causality allowed for assessment of the magnitude and direction of temporal relationships among multiple signals during overlapping time-series windows, holding the promise of revealing paths of information flow within the nervous system. This method has emerged as the leading statistical quantities to furnish directional information from multivariate neural data.

To make use of this formulation, the PAT signals in each short time window is firstly detrend with a 3^{rd} order and then normalized by dividing the standard deviation. In this way, the PAT signals can be approximately regarded as a stationary stochastic process with locally stationary segments, and the collection of the PAT signals from different rat experiments can be treated as an ensemble of realizations. In this paper, the time window is set to be 1min, which is 200 points for the frame rate of 3.33Hz. This is a promise between preserving the time variability and maintaining the smoothness of the estimated spectral quantities. The model order is determined with theAkaike Information Criterion (AIC). Because the AIC generally decreases monotonically with increasing order for all the windows, we set the model order to be 19 selected as a tradeoff between sufficient spectral resolution and overparameterization, and the model order is validated with white noise test. The directional causality was calculated as the average value in the 0-0.3Hz range which makes up about 84% of the total power in the 1.6Hz frequency band. Granger causality spectral analysis of both the HbO2 and Hbr data were performed for all pairs between the SSS, hippocampus, cortex, and the reference signals which is used for significance assessments.

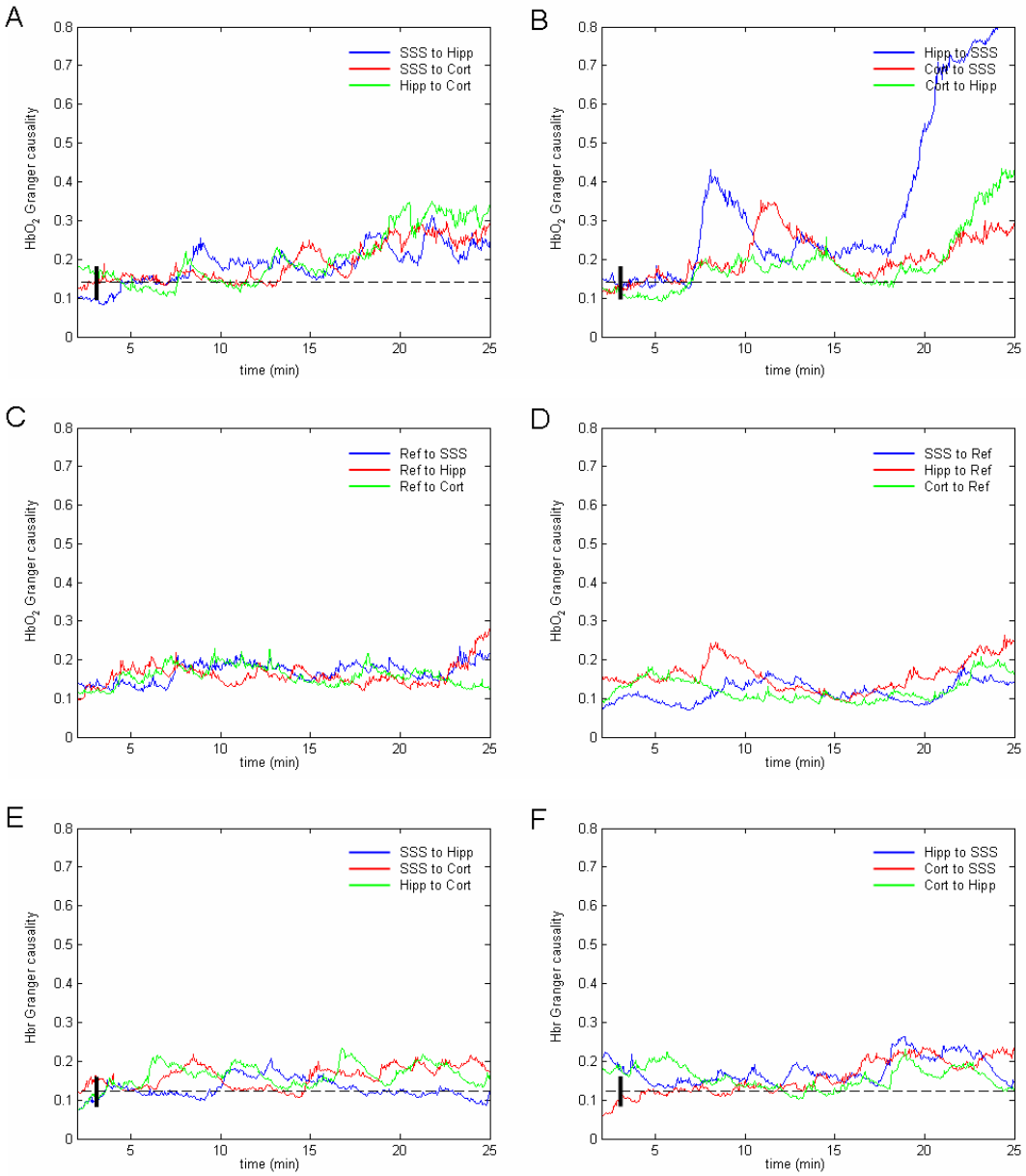

Fig. 13 Granger causality analysis of the HbO2 and Hbr signals between different regions of the brain and the reference signals. (A) and (B) the granger causality of HbO2 between the SSS, hippocampus and cortex; (C) and (D) the granger causality of HbO2 between the above three brain regions and the reference; (E) and (F) the granger causality of Hbr between the SSS, hippocampus and cortex. The horizontal dotted lines in (A) and (B) are the average value of the granger causality of HbO2 between these three brain regions and the reference, or rather the average value of (C) and (D). Similarly, the horizontal dotted lines in (E) and (F) are the average value of the granger causality of Hbr between these three brain regions with the reference. SSS, superior sagittal sinus; Hipp, hippocampus; Cort, cortex.

Fig. 13 A and B show the time varied granger causality of HbO2 between pairs among the SSS, hippocampus and cortex. Fig. 13 C and D are the granger causality of HbO2 between these three brain regions with the reference, which is less varied with time, and the average value of it can be taken as a noise background or baseline, as indicated in Fig. 13 A and B with dotted black horizontal lines. Similarly Fig. 13 E and F show the granger causality of Hbr for these three brain regions. The results of HbO2 shows that strong influence of the hippocampus to the SSS is present in the first and second stages of the seizure; strong influence of the cortex to the SSS is seen in the second and early third stages; and as the seizure evolves, significant causality for all pairs between these three regions can be seen in both directions late in the third stage. Comparatively, the causality of the Hbr for pairs between these three brain regions is overall less significant, which may be due to the poor SNR of the data. However, some time relevant features can still be obtained through the calculated results.

The granger causality in different times can be better presented in graphs, as shown in Fig. 14. In Fig.14, The arrow presents the direction of the influence, and the visibility presents the magnitude of the causality. The granger causality of less significance is not shown, and the thresholds for HbO2 and Hbr are chosen to be the average value of the causality between the reference and the reference, or rather the dotted lines in Fig. 13 A (or B) and E (or F) respectively. The value of the causality can be read from the colorbars. We see that as the seizure evolved, the connectivity between these three brain regions tended to be more and much closer.

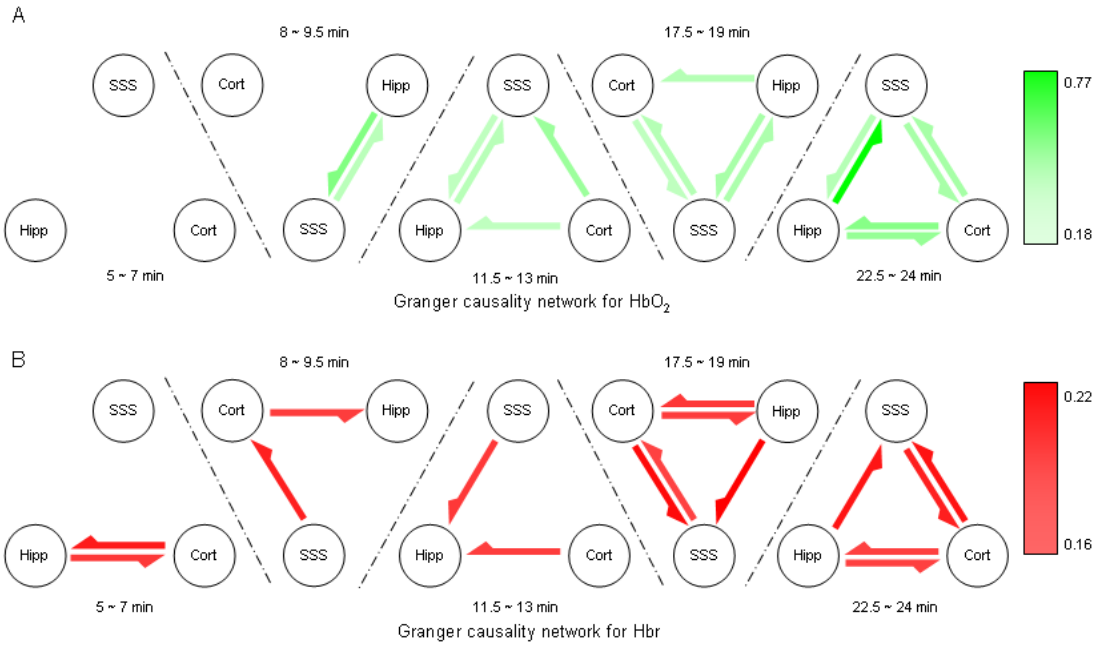

Fig. 14 Granger causality graphs of HbO2 (A) and Hbr (B) between different regions of the brain. The granger causality values are coded by the visibility of the lines between these brain regions (Center), and the arrowheads indicate the direction of granger causal influence. Lines between site pairs not reaching significance in the coherence and Granger causality measures are not shown. SSS, superior sagittal sinus; Hipp, hippocampus; Cort, cortex.

6.10 Significance

Epilepsy affects about 1% of the population world wide, and about 20 to 30% of these patients are refractory to all forms of medical treatment. For those patients the best treatment option is resective brain surgery, which however critically depends on the complete mapping of the local epileptic seizures, and the well understanding of the possible epileptic circuit.

Much of our understanding about seizure comes from electrophysiological recording methods, and intracranial EEG is commonly used for presurgery seizure localization. However, its defects of invasiveness, low spatial sampling and volume conduction may leads to incomplete seizure mapping. As a result, various neuroimaging technologies have been employed to give a high-resolution real time spatial and temporal ‘read out’ of the dynamics of cortical processing.

As the most common neuroimaging method, fMRI is well applied for the diagnosis and presurgery localization of focused seizure, where the hemodynamic changes mainly occurred within the seizure focus and can be well distinguished in fMRI. However, fMRI can not localize generalized seizure because in this case the hemodynamic changes can be found wide-spread in the brain, and it remains unclear whether they arise from a portion of the brain or from more widespread circuits .

This predicament mainly owes to two reasons. One reason is that the spatial and temporal resolution of fMRI is poor, so the initial site of seizure is missed. Most importantly, fMRI is only sensitive to Hbr. It relies on the drop of Hbr in the vein due to the speedy of the blood flow to localize the activation sites of the neurons. However, the change of Hbr and the blood flow is two counter parts during the seizure, so that the changes of Hbr in the tissue may not be as notable as that of HbO2, which mainly results from the dilation of the artery and the blood flow.

In generalized seizure, although current diagnostic methods including intracranial EEG and fMRI all find that regions all over the brain are involved in seizure, this doesn’t surely means that all these regions are the origin of seizure or equally in function. Primary regions or seizure network may be revealed if more information is given. With the realtime PAT operated at two different wavelengths, relative focused regions that were negatively correlated with the SSS were found in the hippocampus and its surroundings following the onset of the seizure using the HbO2 data, and the change of HbO2 in the hippocampus was found to be ahead of the Hbr in the PTZ induced generalized seizure model (Fig. 8, 9, and 10). Since the SSS is decreased in HbO2 when the seizure began, the above regions with high negative correlation coefficient represent regions with hyperoxygenation and hyperfusion, which is usually the marker of the

seizure location. PTZ is a GABA antagonist, and this result is in coincidence with the findings hippocampus is high in GABA receptor concentration. All these imply that PAT may serve better for seizure localization.with appropriate laser wavelength settings and data processing methods.

Besides, generalized seizure occurs in multiple regions all over the brain that form a seizure network. It's important to know the relationship and function of these involved regions. The spatial and temporal resolutions of our realtime PAT system are both about 10 times higher than that of fMRI, thus more subtle hymodynamic changes related to the seizure could be identified. We applied short time window spectral pairwise granger causality method to both the HbO2 and Hbr data, and the time resolved interaction between different regions of the brain was visualized, resulting in a better understanding of epileptic networks at high spatiotemporal resolution.

6.11 Data processing method

PAT has already been employed in the neurovascular coupling study with various animal models, which however are mainly limited in the monitoring of hemodynamic signals in large blood vessels. Actually the changes in capillaries are more related to the metabolic status of the cells. Yet the direct monitoring of the capillary is difficult because the resolution of PAT under the epidermis is usually not enough due to the diffusion of the light. In this work, the signals are averaged in the surrounding region to increase the SNR, and converted into percentage changes regarding to the baseline for comparison. With this method, the small changes in deep tissue that is submerged in the signal of larger blood vessels can be revealed. For example, Fig. 15 shows a 2 minute signal summed within a 9 voxel wide cube around the hippocampus with 1064nm (the black line in the upper right corner), expressed as

$$I_0 = \sum A_{i,j,k} = \sum_{\mathrm{mod}(i+j+k,2)=0} A_{i,j,k} + \sum_{\mathrm{mod}(i+j+k,2)=1} A_{i,j,k} = I_1 + I_2$$

compared with I_1 and I_2 (lines in the lower right corner in red and blue respectively, which are the summed signals with the two halves of the voxel in the cube), where $A_{i,j,k}$ is the value of a voxel in the cube. The difference of I_1 and I_2 can almost be neglected, and calculation shows that the SD of $I_1 - I_2$ is just 0.04 of the SD of I_0. This means the white noise can almost be neglected. Actually, the high frequency fluctuations in the PAT data here are more related to the hemodynamic change in the tissue, which can be inferred from the correlation between the hippocampus and the SSS. The HbO2 signals in the hippocampus and SSS are positively correlated before seizure, but negatively correlated with a high correlation coefficient shortly after the seizure onset. This can be totally explained by the fluctuation of the laser or the influence of the reconstruction algorithm.

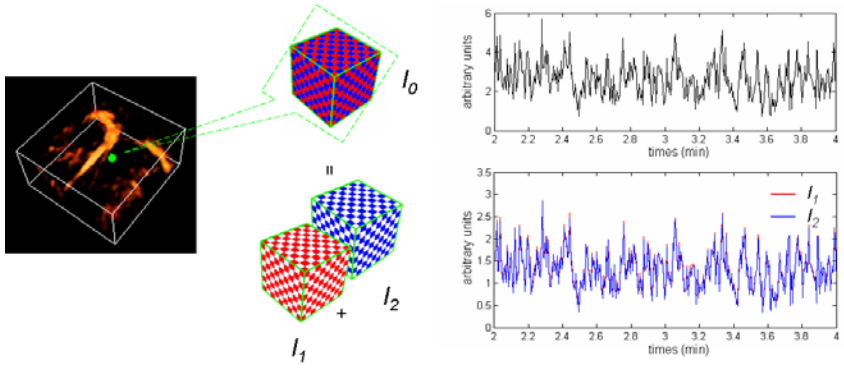

Fig. 15 White noise assessment of the reconstructed images. Upper right corner shows the summed signal of a 9 voxel wide cube, compared with the signals summed with the two halves of the total voxel in the cube (the red and blue lines in lower right corner).

6.12 Other factors in neurovascular coupling

Contradictory data exists for neurovascular coupling. One reason for this lies in the model difference and the individual difference, as well as the systematic influence of the animals , and the other reason may caused by the different principles of various technologies leading to different conclusion in case of incomplete acquisition of the information.

Neurovascular coupling refers to all the aspects regarding the neural metabolic demands and the energy source supply by the vascular system, including the local filed potential, the oxygen-consumption rate, oxygen partial pressure, HbO2 and Hbr volume, blood flow, and so on. More parameters we can measure, the more correct understanding of the neurovascular coupling we can get for the diagnosis of epilepsy.

In this work, through the measuring of HbO2 and Hbr, other factors such as the dilation of the arteries and blood flow, which works as means of power supply to the neurons from the vascular system, can also be indirectly inferred. However, signal analysis can still be complicated sometimes. We only get information of HbO2 and Hbr, making it difficult to infer the status of the neurons. For example, we observed that the HbO2 is decreasing while the Hbr is increasing at the second stage in hippocampus, but since the overall blood supply is increase in the rat brain, we are not sure whether the temporal decreasing of the HbO2 in the hippocampus stands for the decreasing of neural activity there or it's caused by insufficient blood supply, and which factor dominates. Furthermore, the oxygen partial pressure in the tissue which is more related to the neural activity can be uncoupled with the HbO2 change. This also impedes our understanding of neurovascular coupling.

The preceding of the hemodynamic signal to the EEG signal in ictal seizures has also been reported with various kinds of technologies. However, in other cases and in our studies, this

phenomenon is not seen. Because this is of quite importance in aspect of seizure prediction and manual intervention, more ictal neurovascular coupling studies should be done with different seizure models to find out the condition and the mechanism of this phenomenon.

6.13 Limitation in our work

There are limits in our work. First of all, the image contrast and resolution are greatly hindered by the limited transducer numbers with our system. Besides, although the morphology of seizures exhibit quite similarity for all the rats in our experiments, images with the two different wavelengths are not acquired on the same animal. Although this will be not likely to refute the main conclusions we got, valuable information that need simultaneous dual-wavelength recording to be unearthed is missed. Finally and most important of all, generalized seizure involves wide-spread network all over the brain, in which the electrical and hemodynamic signal of different regions are closely related. In our work, we only analyzed the granger causality of the hemodynamic change in SSS, hippocampus, and cortex. Detailed study needs to be done to dig out the interaction of more different regions.

7. Simultaneous real-time 3D photoacoustic tomography and EEG for neurovascular coupling study in an animal model of epilepsy

A. System setup

The real-time 3D photoacoustic system has already been reported, and the main feature of this system is the sparse spherical array which is consisted of 192 discrete transducers, as shown in Fig. 16. The transducers were mounted on a custom fabricated white ABS spherical interface with a distance of 71.6mm from the center of the array, and formed into seven layers. Each transducer had a central frequency of 5MHz and a reception bandwidth of greater than 80%, resulting in an almost isotropic spatial resolution about 0.2mm. The active area of the transducer was 3mm in diameter, and the angular acceptance was about 15 degree. The signal from the 192 transducers was amplified by 16 homemade preamplifier boards and coupled into a 64 channel parallel data acquisition system with 3:1 multiplexing, as indicated with three different colors.

Rats were elevated to the center of the spherical interface through a chamber fixed at the tank bottom, whose top was about 15mm beneath the interface center, and a transparent plastic wrap was used to cover the chamber top. Ultrasound gel was used to couple the sound from the animal to the plastic wrap. The ultrasonic transducer array with the spherical interface, placed in the water bath, was therefore acoustically coupled to the mouse tissues. The laser light was delivered through a concave lens giving a homogenous illumination on the head of the rat. In this study, two wavelengths were used, 1064nm and 710nm. The 1064nm light was from a pulsed Nd:YAG (5~20ns pulse width), and the 710nm light was from a Q-switched Nd:YAG pumped Ti:sapphire laser. The final laser intensity on the rat head was about 50mJ/cm^2 for 1064nm, and 4mJ/cm^2 for 710nm, all below the ANSI exposure limits. Both the two lasers operate at 10Hz, so that the system could record one complete set of 3D PAT data in 0.33s.

Two injection needles, inserted into the front cortex of rat brain about 3mm below the scalp, were served as EEG electrodes as shown in Fig. 16(b). One electrode was picked for reference and ground signal, while the other electrode was to record EEG signal. The EEG signal was amplified (RA16PA, TDtucker-Davis Tech.) and recorded (RZ5 Bioamp Processor, TDtucker-Davis Tech.) with a sampling rate about 50kHz. Both the two electrodes were firmly glued on the rat head and the wires were tightly attached to the animal holder using glue tapes, so as to avoid noise induced by any possible unnecessary movement of the rat or experiment operators. The PAT system gave an output synchronized signal to the EEG system, so that the two systems were well synchronized.

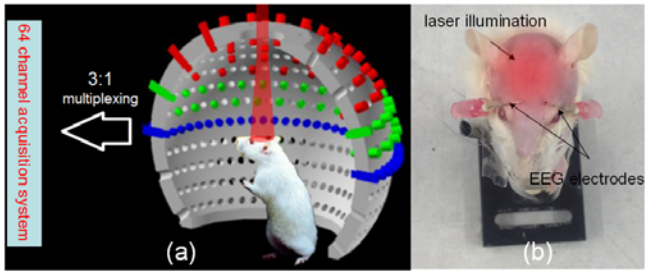

Fig. 16 Experimental setup of the combined system. (a) Schematic of the photoacoustic system; (b) Rat with two electrodes in the brain; and the laser illumination is also indicated

B. Animal preparation

Two groups of rats (n=16 rats, each about 35~45g, with 8 rats for 1064nm and the other 8 rats for 710nm) were used. The rats were anaesthetized with about 0.25ml Urethane (0.25g/mL) and got hair on the head shaven. Before mounting the rats on the homemade plastic holder, a syringe containing 0.04g/ml PTZ with a scalp needle was inserted in the abdomen and fixed with glue. PTZ was used to induce generalized seizure in rat brain, which has already been established. Then the two electrodes were inserted, and the rats were elevated into the transducer array center of the photoacoustic system for scanning. Each experiment lasted 25min, and PTZ was administrated with a dose of 0.5mL at 5min. All rats were kept alive through the experiment. All the animal procedures performed were in accordance with the approved University of Florida IACUC protocols.

C. Data processing

With a frame rate of 3.3f/s, 5000 complete sets of PAT data were recorded. Before doing 3D reconstruction and processing, 2D PAT images were reconstructed with data collected by the 64 transducers in the lowest layer of the array, which were indicated with blue in Fig. 16. The 2D images were carefully checked to avoid the possible motion artifact induced by the movement of the rat head during the experiment. 3D images were calculated using delay&sum algorithm, which was accelerated by GPU parallel technique. Then the negative pixel values in were set to zero. Each set of the reconstructed 3D images had a voxel number of 201×201×101 representing a $10\times10\times5mm^3$ volume, which could be calculated in 0.97s. Amira (from Visage Imaging, Inc.) was used to render the 3D images.

There were two sources of noise in the EEG signal, a strong sharp 10Hz noise from the Q-switch of the laser, and the 60Hz alternating current noise. For de-noising, the deteriorated data

by the Q-switch was replaced with adjacent data, and the 60Hz alternating current noise was removed by filtering out 58-62Hz in frequency domain (Fig. 17). Then the EEG data was applied with a low pass filter of 100Hz, and transformed into a 300000 point signal for the 25min EEG recording, corresponding to sampling rate of 200Hz.

For neurovascular coupling study, we first extracted the averaged PAT signals of the superior sagittal sinus (SSS) of each rat from the reconstructed 3D images and compared it with the corresponding EEG signal. We choose the PAT signals of the SSS because it has the highest SNR and is highly distinguishable in the reconstructed 3D image. Because 1064nm and 710nm are mainly absorbed by oxy-hemoglobin (HbO_2) and deoxy-hemoglobin (HbR), the acquired results for these two wavelengths can be taken as the changes of HbO_2 and HbR respectively. All the acquired results were examined by experts in the neurology.

A. Data preprocessing

Representative time frames of 2D images through the experiment are displayed in Fig. 17(a) with a time interval of 1min, compared with a rat brain photo taken after the experiment (Fig. 17(b)). Although the image quality is not excellent due to the limited transducer positions (only 64 transducers are averaged once), the SSS and two transverse sinuses (TS) are clearly reconstructed, and some other small blood vessels are also revealed. In Fig. 17(a) it is observed that there is no palpable shift of the rat brain which is a prerequisite for the following data processing. In our experiments, 3 out of 8 rats with 1064nm moved, but all the rats in the second group remained still. We also notice that it's hard to tell when the seizure begins just by eyes from these 2D images, so quantitative analyze is needed.

EEG signals were recorded to confirm the onset, duration, and morphology of the seizure, which is shown in Fig. 18(a). The EEG signal is stable before the drug injection at 5min, when isolated high amplitude spikes can be easily seen in the EEG signal. After this spontaneous fast discharges begin to show and increase in amplitude in the following 2 to 3 minutes. The seizure onset comes about 142 ± 45s after the drug injection, which is defined to be the first signal that exceeds 6 times the standard deviation (SD) of the baseline (the average signal in the first 4min). As the seizure evolves, the firing frequency generally gets lower, but the EEG signal begins to decrease in and keeps firing through the experiment. Fig. 18(b) shows the EEG signal in a short time window (blue), compared with the original data before preprocessing (red). We can see that both the noises from the Q-switch and the alternating power supply are removed.

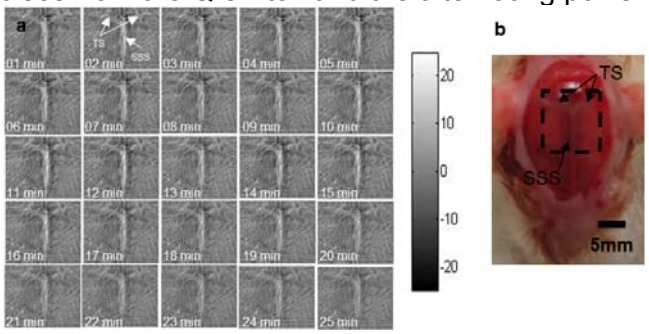

Fig. 17 Representative time frames of 2D PAT images of the rat brain, compared with an anatomical image. (a) Representative time frames of 2D PAT images of the rat brain with 1064nm. The time interval is 1min, and each image covers $10 \times 10 mm^2$ with 201×201 pixels. (b) Photo of rat brain with hair and scalp being removed. The SSS, TS, and the reconstruction area is indicated. Scale bar is 5mm through the figure.

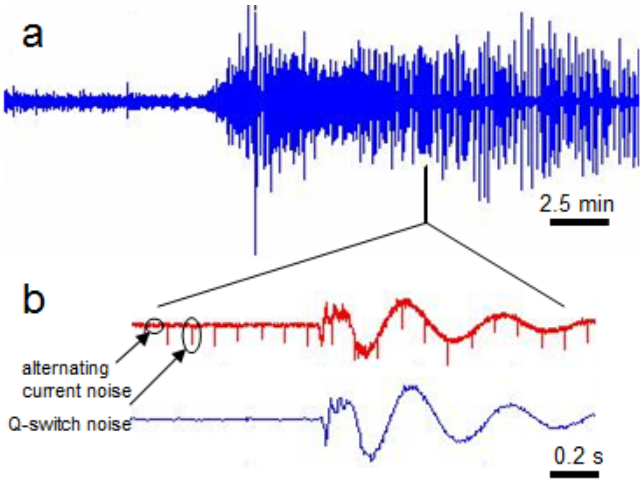

Fig. 18 EEG signal for PTZ-induced seizure. (a) Typical EEG signal after processing. (b) The original (blue) and processed (red) EEG signal in a short time wiondow..

B. 3D image reconstruction

Fig. 19 shows the reconstructed 3D images from different views. The reconstructed volume is 10 x 10 x 5mm^3 with a 0.05mm voxel size. Similar to the 2D images, the SSS and TS can be clearly revealed both in the 3D images of HbO_2 and HbR, although the SNR of HbR is not as good as that of HbO_2 due to relatively low laser intensity of 710nm, as well as the low concentration of HbR in the blood vessels compared to that of HbO_2. It is also noticed that in the 3D images of HbO_2, we can see the Ostia end of the straight sinus (SS) below the SSS which can not be seen in the 2D images. All these demonstrate the excellent positioning ability of our 3D PAT system.

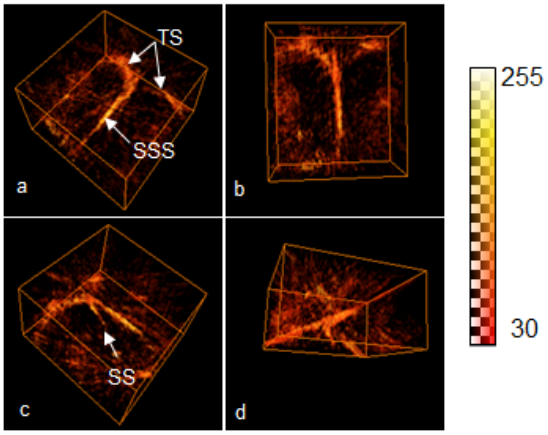

Fig. 19 Reconstructed 3D PAT images of the rat brain with 1064nm from different views. SSS, TS, and SS can be seen in the image. The image domain is 10×10×5mm^3 with 201×201×101 pixels. Colarbar is indicated.

C. Neurovascular coupling study

For each set of PAT data, the average signal in a ROI that could enclose the SSS was extracted and taken as the change of the SSS (Fig. 20(a) and Fig. 20(b)), which was further converted into percentage changes to the baseline. For all the rat datas analyzed (n=14), the EEG signals looked the same in shape and timing (Fig. 20(c) and Fig. 20(d)). This means our PTZ induced generalized seizure modal is quite stable and the drug administration is well controlled, so that all the rat results are comparable. The two PAT curves in Fig. 20(c) and Fig. 20(d) are also representatives. The PAT signals for HbR is smoothed using a moving window of 3 seconds to improve the SNR. The neurovascular coupling of our rat model can be obtained by comparing these two groups of PAT curves and the corresponding EEG signals.

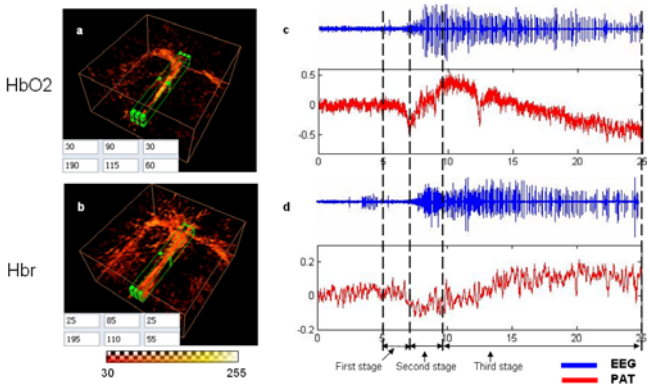

Fig. 20 Typical results for HbO_2 (a and c) and HbR (b and d) respectively, with the ROI for the SSS indicated in the 3D PAT images. The reconstruction domain for the 3D images (a and c) are $10\times10\times5mm^3$ with 201×201×101 pixels. c and d are the EEG and PAT signals of SSS for a and b respectively. The EEG signals (blue line) are in arbitrary units, and the PAT curves (red line) are represented as the change with respect to the baseline. The whole seizure process after the injection of PTZ can be divided into three stages. The PAT signal for HbR has been smoothed using a moving window of 3 seconds. The time units in c and d is minutes.

Both the EEG and PAT signals in these two datas remain quite stable before the drug injection. After that the time course of the experiment can be generally divided into three stages, as indicated. In the first stage, the EEG signal increases in amplitude as seizure initiates. At the same time, there's a prominent sudden decrease in the HbO_2 signal while the HbR signal just slightly increases. This indicates that for this period of time, the increase of blood supply was inadequate for the metabolism of neurons. In the second step, we can see that the EEG signals continue to increase as the seizure evolves. However, the HbO_2 signal begins to increase and the HbR begins to decrease at the same time. Thus we conclude that the blood supply is greatly increased due to dilation of arteries and increasing of blood flow. In the third step, although the EEG signal gradually decreases in firing frequency, the HbO_2 signal is still decreased, while the HbR signal increases. This means the blood flow is decreased.

Through the whole seizure process, we see the coincidence that the two PAT signals are well negatively correlated. When the HbO_2 reaches its peak the HbR just drops to its minimum, or otherwise. To make it more convincing, we calculate the average changes of HbO_2 and HbR across all the rat experiments, as shown in Fig. 21. The two curves there are achieved by first normalizing the data in a single experiment to the baseline, and then averaging the data of all rats in the same group. The final data are further averaged every 30secs, with the

corresponding SD indicated. The correlation coefficient of these two signals is calculated to be -0.705.

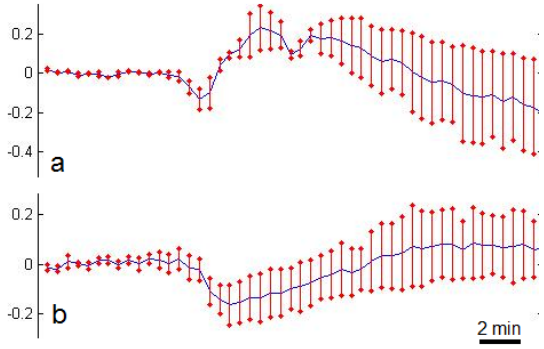

Fig. 21 Full timecourses of mean percent changes of the HbO_2 (a) and HbR (b) signals, which are negatively correlated with each other. The SD for each signal is indicated every 30s. Vertical bar represents the amplitude of the PAT signal changes to the baseline.

Neurovascular coupling study of epilepsy requires simultaneous recording of neuronal activity and macroscopic hemodynamic signals in the brain, bringing significant challenges in terms of experimental paradigm and instrument performance. We successfully integrated the EEG system into our real-time 3D PAT system that is based on a 64-channel parallel data acquisition system and a spherical transducer array, and realized the simultaneous recording of neuron activity and hemodynamic signal in the whole rat brain over the entire epileptic seizure process.
The neurovascular coupling of the intraperitoneal PTZ rat model here is studied with the HbO_2 and HbR signals of the SSS. PTZ has been used experimentally to induce generalized seizure, where hemodynamic changes can be found all over the brain. As one of the main blood vessels in the brain, SSS is highly involved in the PTZ-induced seizures. When the seizure begins, we observed a sudden decrease in HbO_2 for 1 to 2 minutes, followed by a dramatic increase. The 'dip' observed here is much similar to the reported 'epileptic dip' with ORIS, but found on the cerebral cortex. It's different from the 'initial dip' which only lasts several seconds. In the second stage of the seizure, the HbO_2 signal keeps on increasing and finally succeeds the baseline, which supports the idea that the increase of cerebral blood flow oversupplies the increased metabolic demands of the neurons in epileptic seizures. And the negative correlation we observed between the HbO_2 and HbR signals in SSS here can be explained by the fact that the veins don't usually dilate as much as the arteries.
There are limitations in our work. We only studied the PAT signals of SSS, but in-depth information of the vascular coupling is more embedded in the local hemodynamic changes. Thus the signals of different regions in the brain tissue need to be extracted, based on which, the neural network analysis can be carried out.

8. Miniature wearable PAT array system

We developed a miniature wearable PAT system that employs a homemade 64-element transducer array.

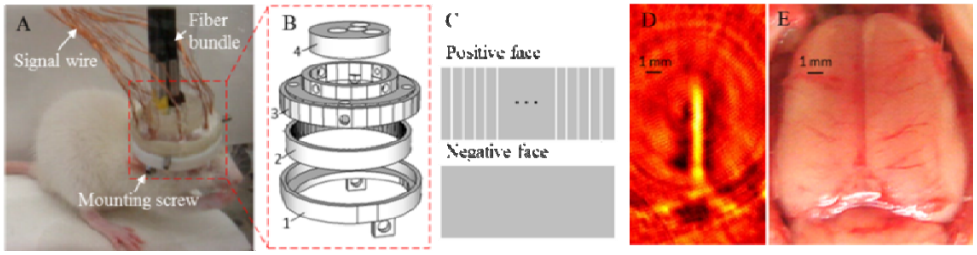

Fig. 22 Miniature wearable PAT imaging system and validation. (A) Experimental photograph of PAT imaging system mounted on a rat head. (B) Corresponding diagram showing the device components. (C) Schematic diagram of the fabrication of PVDF transducer array. (D) Noninvasive PAT image of a freely moving rat brain with skin and skull intact. (D) Open-skull photograph of the rat cortex surface after the PAT experiments

The PAT detecting module, shown in Fig.22A, is composed with a cap-like housing, 64-element transducer array, 64 signal wires and 4 fiber bundles. Fig.22B shows the schematic diagram of the cap-like housing which is designed and fabricated with 3D printing technique. There are four parts in the housing structure, component 1 serves as the bottom holder used to support the whole detecting module and also as mounting part with the help of two screws placed oppositely on both side; component 2 is used to hold the transducer array; component 3 is the cover to protect the PAT imaging space; component 4 is used to connect the fiber bundles to the imaging area. As shown in Fig. 22C, we utilize PVDF film to fabricate the transducer array using its unique feature of flexibility. In order to make a 64-element array based on a 94.2mm×5mm size PVDF film (1.47mm width and 5mm height for each element), we leave one face of the PVDF as a sharing ground and divided the other face into 64 rectangles and each one is working as an independent acoustic detector. The benefit of this design is that the array is more electronic stable and it's easy to be assembled into the transducer holder in the housing. Fig.22D shows a typical non-invasive PAT image obtained with the miniature PAT imaging system of a freely moving rat brain with skin and skull intact. Fig. 22E is the photograph of the rat cortex surface with skin and skull removed after PAT experiment. We also built a 64-channel amplify and data acquisition system which can acquire 64-channel signals simultaneously at a sampling rate of 50MHz. The imaging rate of the PAT system can achieve 10 frames/s without averaging.

8.1 Experiment and animal preparation

The bottom holder (component 1) was mounted on the rat head for one hour before performing experiment in order to let the rat used to the device. The detecting space was filled with phantom for acoustic signal transports to the transducer array. Anti-load methods were employed to reduce the weight on the rat and it ensures the least restriction on experimental animal goal of this work. Besides, EEG recordings were utilized in the experiment as a standard reference to the PAT results. We conduct experiments on awake, freely moving rats (80-100g) in both resting and seizure (drug induced generalized model, Pentylenetetrazol, PTZ, 0.1g/Kg)

state using 1064 nm wavelength pulsed laser light. All procedures were approved by the University of Florida Animal Care and Use Committee and conducted in accordance with the National Institutes of Health Guide for the Care and Use of Experimental Animals.

8.2 Results

Fig. 23 shows the PAT and EEG results of a behaving rat in resting state. The imaging time is 4 min and the imaging rate is 3.33 frames/s (3 times averaging). Fig. 23A is the recorded EEG results and Fig. 23B shows reconstructed PAT signal change of MCV (middle cerebral vessel) marked with white arrows in Fig. 23C. Bottom row of Fig. 23C is the close up view of the top row PAT images at different time. From Fig. 23A and 23B we can see that there is a corresponding significant change at the time around 50s in both the EEG and PAT results. It indicates an intense neural activity which has been verified by a moving of the rat according to the recorded video.

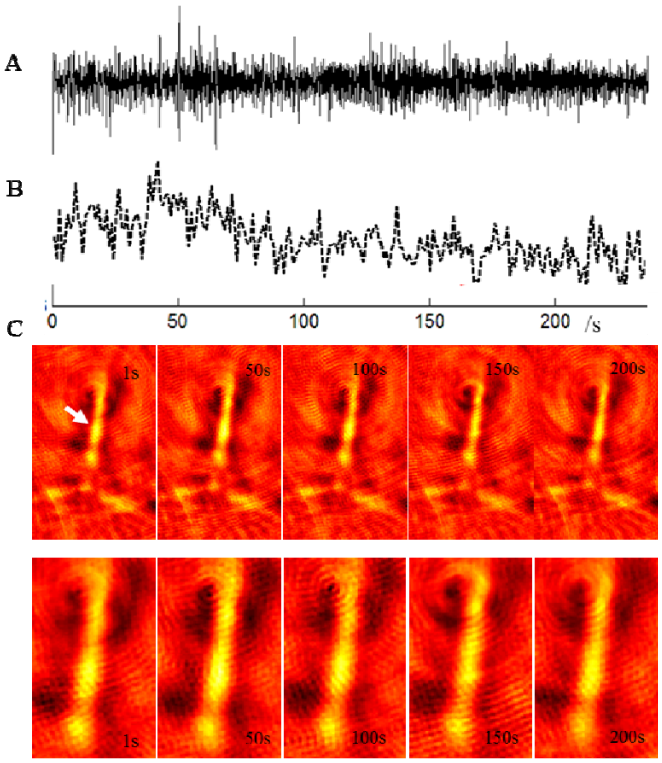

Fig. 23 Noninvasive PAT imaging of a freely moving rat in resting state. (A). EEG recording; (B). Reconstructed PAT signal changes of MCV marked with white arrows in (C); (C). PAT images of the rat brain at different time.

Fig. 24 shows the PAT and EEG results of an awake, freely moving rat in seizure state with PTZ drug injected at the time of 90 s. The imaging time is 20 min and the imaging rate is 3.33 frames/s (3 times averaging). Fig. 24A is the recorded EEG results and Fig. 24B shows

reconstructed PAT signal changes of three locations marked with white arrows in Fig. 24C. Fig. 24C shows PAT images at different time.

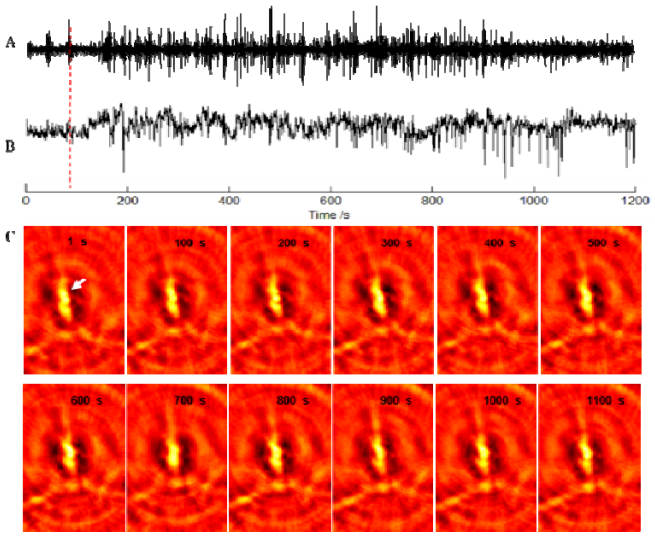

Fig. 24 Noninvasive PAT imaging of a freely moving rat with drug induced seizure. (A). EEG recording; (B). Reconstructed PAT signal changes MCV marked with white arrows in (C); (C). PAT images of the rat brain at different time.

Fig. 25 shows the PAT and EEG results of an anesthetized rat in seizure state with PTZ drug injected at the time of 180 s. The imaging time is 20 min and the imaging rate is 3.33 frames/s (3 times averaging). Fig. 25A is the recorded EEG results and Fig. 25B shows reconstructed PAT signal change of MCV marked with white arrow in Fig. 24C. Fig. 24C shows PAT images at different time.

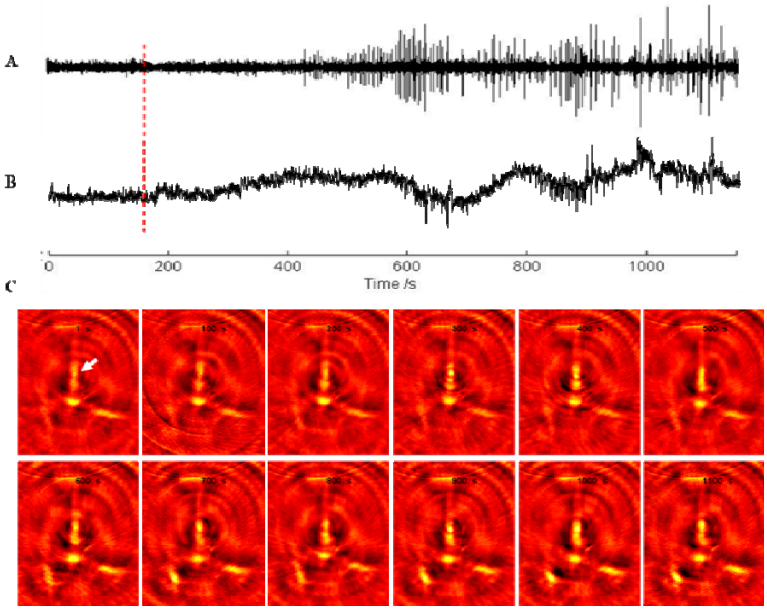

Fig. 25 Noninvasive PAT imaging of a freely moving rat with drug induced seizure. (A). EEG recording; (B). Reconstructed PAT signal changes of MCV marked with white arrows in (C); (C). PAT images of the rat brain at different time.

8.3 Discussion

For the first time, we have presented a miniature wearable photoacoustic tomography system for non-invasive real-time imaging in freely moving rats. The system is based on a ring-shaped PVDF transducer array containing 64 elements. With the 64-channel amplify and data acquisition system, it can achieve imaging rate of 10 f/s which is the frequency of the pulsed laser we utilized in the experiments. Both the rest and drug-induced seizure results demonstrate the imaging ability of our miniature PAT system on freely-moving rats, as well as the neurovascular effect.

However, there are still some limitations of our current miniature PAT system. The first is its relatively low spatial resolution due to the limited sensitivity of PVDF and the limit number of transducer element. The signals we can acquire are mainly from the middle cerebral blood vessel. The second is the light illumination. We currently use four fiber bundles placed according to the shape of the main blood vessels in the brain which results in non-uniform light distribution on the detecting area. The third but not the last one, happened during experiments, is the fixation of the whole probe. We applied two screws held against the skull of the rat to mount the probe on the head, but it's always not enough to bear the rat's intensive motion, especially at the seizure onset state.

Key Research Accomplishments

1. We have completed the design for an array based PAT system, which is the most important part of Task 1.
2. We have developed three novel schemes that can enhance our current reconstruction software.
3. We have completed the construction of the proposed an array based real-time PAT system, and calibrated and tested the system using extensive phantom experiments.
4. We have built the animal interface and successfully tested it for *in vivo* imaging of rat brain.
5. We have developed three novel schemes that can enhance our current reconstruction software.
6. We have conducted phantom experiments that confirmed our software enhancement.

7. We have conducted phantom experiments that confirmed our software enhancement.
8. We have developed the advanced boundary conditions scheme, and implemented the 3D reconstruction codes and their parallelization which allowed efficient high performance PAT image reconstruction.
9. We have conducted simulation and phantom experiments that confirmed our software enhancement.
10. We have performed extensive *in vivo* experiments using the rat epilepsy model to evaluate the PAT system we developed in this project. The results show that we were able to image the functional anatomy of epileptic foci noninvasively and in real time at a spatial resolution of ~150μm.
11. We have developed and validated a rat model of temporal lobe epilepsy.
12. We have performed extensive *in vivo* experiments to achieve concurrent EEG and PAT recordings. Interesting results are obtained that may be significant for seizure prediction and for neurovascular coupling studies.
13. We have designed and constructed a light-weighted animal/transducer interface that can be used for chronic monitoring of freely moving animals.
14. We analyzed the images from the in vivo experiments.
15. We built a simultaneous real-time 3D photoacoustic tomography and EEG system for neurovascular coupling study in an animal model of epilepsy

16. We developed a miniature wearable PAT system that employs a homemade 64-element transducer array

Reportable outcomes (see the Appendix to this Summary Report)

Conclusions

We have fulfilled the statement of work proposed. The real-time PAT system completed in Years 1 and 2 provides us a platform for performing the extensive phantom and animal

experiments proposed for the coming years. In year 3, we implemented reconstruction codes and we performed simulation and phantom experiments to evaluate the software developments. In year 4, the real-time PAT system constructed in this project coupled with the light-weighted cap interface has provided us a platform for performing extensive animal experiments in freely moving rats. In Year 5 we completed the proposed Tasks 6 and 7 for continuous recording of EEG and PAT over a long period of time to monitor seizure activity continuously to characterize changes during interictal, ictal and post-ictal periods when a spontaneous seizure occurs. We analyzed the images from the in vivo experiments and write final reports. We completed any unfinished experimentation during these months such that we have a sufficient number or rats monitored with EEG and PAT to reach statistical significance.

References

The progress report for the year 1 of the project.

The progress report for the year 2 of the project.

The progress report for the year 3 of the project.

The progress report for the year 4 of the project.

Appendix

L. Yao, H. Jiang, “Enhanced photoacoustic tomography using total variation minimization”, *Applied Optics* 50, 5031–5041 (2011).

L. Yao and H. Jiang, "Photoacoustic image reconstruction from few-detector and limited-angle data," *Biomed. Opt. Express* **2**, 2649-2654 (2011).

Bo Wang, Liangzhong Xiang, Max S. Jiang, Jianjun Yang, Qizhi Zhang, Paul R. Carney, and Huabei Jiang, Photoacoustic tomography system for noninvasive real-time three-dimensional imaging of epilepsy, Biomed. Opt. Express 3, 1427-1432 (2012).

Zhen Yuan, Huabei Jiang, A calibration-free, one-step method for quantitative photoacoustic tomography, *Med. Phys.* **39**, 6895-6899(2012).

L. Xiang, L. Ji, T. Zhang, B. Wang, J. Yang, Q. Zhang, M. S. Jiang, J. Zhou, P. R. Carney, H. Jiang, “Non-Invasive Real-Time Tomographic Imaging of Epileptic Foci and Networks,” NeuroImage 66, 240-248 (2013).

Bo Wang, Junli Zhou, Paul Carney, Huabei Jiang, Simultaneous EEG and photoacoustic monitoring of epilepsy in freely moving rats, J Neuroscience Methods (in review).

Bo Wang, Junli Zhou, Paul Carney, Huabei Jiang, Simultaneous real-time 3D photoacoustic tomography and EEG for neurovascular coupling study in an animal model of epilepsy, J Neural Engineering (in review).

Enhancing finite element-based photoacoustic tomography using total variation minimization

Lei Yao and Huabei Jiang*

Department of Biomedical Engineering, University of Florida, Gainesville, Florida, 32611USA

*Corresponding author: hjiang@bme.ufl.edu

Received 27 May 2011; accepted 25 July 2011;
posted 25 July 2011 (Doc. ID 148169); published 30 August 2011

A total variation minimization (TVM)-based finite element reconstruction algorithm for photoacoustic (PA) tomography is described in this paper. This algorithm is used to enhance the quality of reconstructed PA images with time-domain data. Simulations are conducted where different contrast levels between the target and the background, different noise levels, and different sizes and shapes of the target are studied in a 30 mm diameter circular heterogeneous background. These simulated results show that the quality of the reconstructed images can be improved significantly due to the decreased sensitivity to noise effect when the TVM is included in the reconstruction algorithm. The enhancement is further confirmed using experimental data obtained from several phantom experiments and an *in vivo* animal experiment. © 2011 Optical Society of America

OCIS codes: 100.2980, 170.3010, 170.5120, 170.6960.

1. Introduction

Photoacoustic tomography (PAT) is an emerging noninvasive imaging technique that combines the merits of high optical contrast and high ultrasound resolution in a single modality [1–3]. In PAT, the Helmholtz-like photoacoustic (PA) wave equation has been commonly used as an accurate model for describing laser-induced acoustic wave propagation in tissue. While analytical reconstruction methods have been used for PA image reconstructions, the finite element method (FEM)-based approach appears to be particularly powerful in this regard [4,5]. The advantages of the FEM-based PAT method include (1) quantitative imaging capability by recovering optical absorption coefficient, (2) elimination of the assumption of homogeneous acoustic medium needed in analytical methods, (3) accommodation of object boundary irregularity, and (4) appropriate boundary conditions implementations.

Our finite element PAT approaches are based on a regularized iterative Newton method, which have been tested and evaluated using extensive simulations and phantom experiments in both the frequency and time domain [4–7]. Compared with the frequency domain method, the time domain method can reconstruct images with less background artifacts, especially when the target size is very small, and can provide a more accurately recovered target size [7]. While these results are encouraging and promising, we realize that measurement noises are still the major factor affecting the quantitative accuracy of the reconstructed images. For example, errors for quantitatively recovering optical absorption coefficient can be as large as 10% for simulated data with 5% noise added and 20% for experimental data [6,7].

In an effort to reduce the noise effect and further enhance the quantitative accuracy of PA image reconstruction, in this paper, we consider a total variation minimization (TVM) scheme within our FEM-based reconstruction framework. Our existing reconstruction algorithms are based on the least-squares criteria (i.e., the regularized Newton method) [8,9] that stand on the statistical argument that the least-squares estimation is the best estimator over an entire ensemble of all possible pictures. Total variation, on the other hand, measures the oscillations of a given function and does not unduly punish

0003-6935/11/255031-11$15.00/0

discontinuities [10,11]. Hence, one can hypothesize that a hybrid of these two minimization schemes should be able to provide higher-quality image reconstructions. In fact, the strategy of finding minimal total variation has proved to be successful in applications including electrical-impedance tomography [11], microwave imaging [12], image processing [10,13,14], optimal design [15], and diffuse optical tomography [16]. The TVM has also been implemented and tested in a non-FEM-based PA reconstruction framework [17–19].

In Section 2, we describe in detail the implementation of TVM within our existing PAT reconstruction framework in the time domain. In Section 3, we demonstrate the enhanced reconstruction algorithm using simulated, phantom, and *in vivo* data. The conclusions are made in Section 4

2. TVM Scheme

To describe our TVM method, we first briefly introduce the FEM-based regularized Newton method in the time domain. The time domain PA wave equation in tissue can be described as follows [20]:

$$\nabla^2 p(\mathbf{r},t) - \frac{1}{v_0^2}\frac{\partial^2 p(\mathbf{r},t)}{\partial t^2} = -\frac{\Phi(\mathbf{r})\beta}{C_p}\frac{\partial J(t)}{\partial t}, \qquad (1)$$

where p is the pressure wave, v_0 is the speed of acoustic wave in the medium, β is the thermal expansion coefficient, C_p is the specific heat, Φ is the absorbed

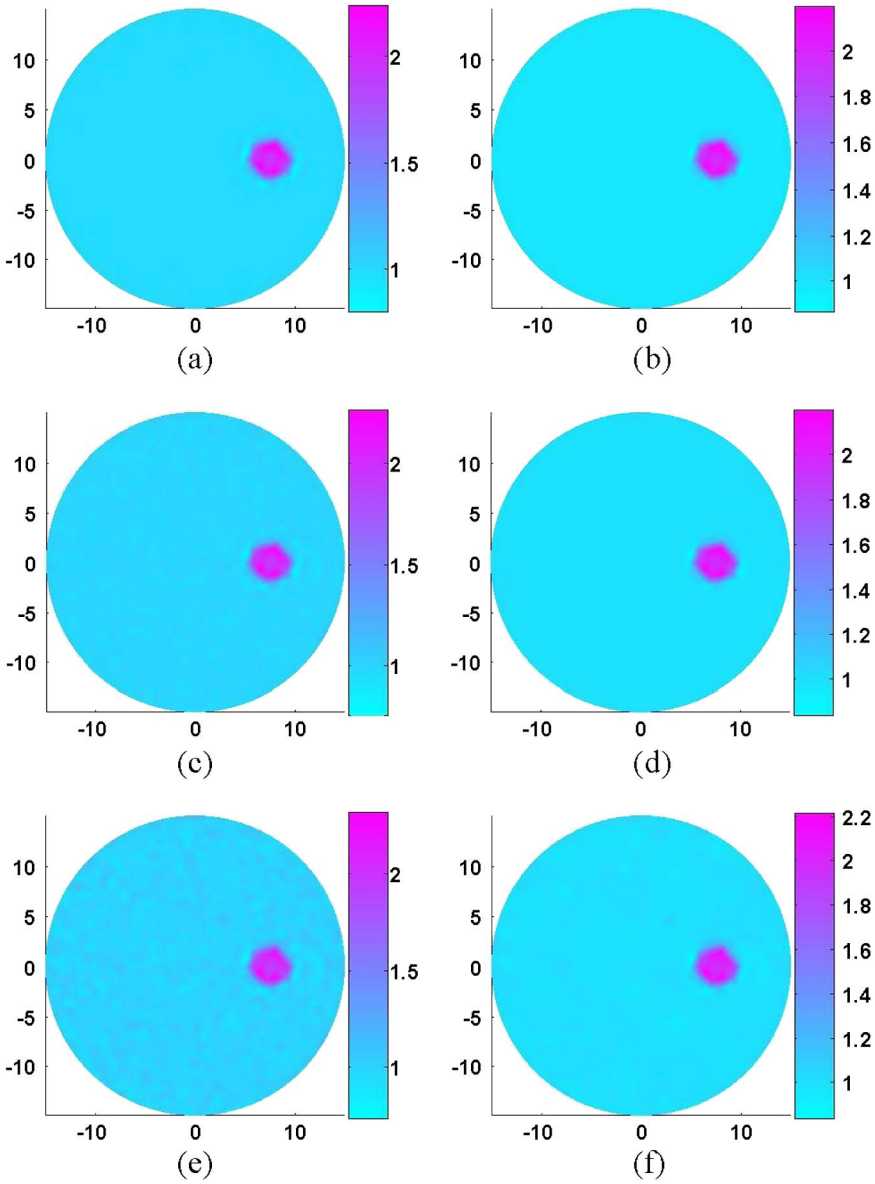

Fig. 1. (Color online) Reconstructed absorbed energy density images from simulated data with and without the TVM enhancement under different noise levels (case 1). (a) Without the TVM, 0% noise, (b) with the TVM, 0% noise, (c) without the TVM, 10% noise, (d) with the TVM, 10% noise, (e) without the TVM, 25% noise, (f) with the TVM, 25% noise. The axes (left and bottom) illustrate the spatial scale in millimeters, whereas the color scale (right) records the absorbed energy density in millijoules per cubed millimeter.

energy density, and $J(t) = \delta(t - t_0)$ is assumed in our study.

Expanding p as the sum of coefficients multiplied by a set of basis function ψ_j, $p = \sum p_j \psi_j$, the finite element discretization of Eq. (1) can then be written as [7]

$$\sum_{j=1}^{N} p_j \left[\int_S \nabla \psi_i \cdot \nabla \psi_j \mathrm{d}S \right] + \sum_{j=1}^{N} \ddot{p}_j \left[\int_S \frac{1}{v_0^2} \psi_i \psi_j \mathrm{d}S \right] - \oint_l \psi_i \nabla p \cdot \hat{n} \mathrm{d}l = \int_S \frac{\beta \Phi}{C_P} \frac{\partial J}{\partial t} \psi_i \mathrm{d}S. \quad (2)$$

The first-order absorbing boundary conditions used are [21]

$$\nabla p \cdot \hat{n} = -\frac{1}{v_0} \frac{\partial p}{\partial t} - \frac{p}{2r}, \quad (3)$$

where $\hat{n}$ is the unit normal vector.

In both the forward and inverse calculations, the unknown coefficient Φ needs to be expanded in a similar fashion to p as a sum of unknown parameters multiplied by a set of locally spatially varying Lagrange polynomial basis functions. Thus, the matrix form of Eq. (2) becomes

$$[K]\{p\} + [C]\{\dot{p}\} + [M]\{\ddot{p}\} = \{B\}, \quad (4)$$

where the elements of matrix $[K]$, $[C]$, and $[M]$ are

$$K_{ij} = \int_S \nabla \psi_i \cdot \nabla \psi_j \mathrm{d}S + \frac{1}{2r} \oint_l \psi_i \psi_j \mathrm{d}l;$$

$$C_{ij} = \frac{1}{v_0} \oint_l \psi_i \psi_j \mathrm{d}l;$$

$$M_{ij} = \frac{1}{v_0^2} \int_S \psi_i \psi_j \mathrm{d}S;$$

and the column vectors $\{p\}$, $\{\dot{p}\}$, $\{\ddot{p}\}$, and $\{B\}$ are

$$B_i = \frac{\beta}{C_p} \int_S \psi_i \left(\sum_k \psi_k \Phi_k \right) \mathrm{d}S \cdot \frac{\partial J}{\partial t}$$

$$\{p\} = \{p_1, p_2, \cdots p_N\}^T;$$

$$\{\dot{p}\} = \{\dot{p}_1, \dot{p}_2, \cdots \dot{p}_N\}^T;$$

$$\{\ddot{p}\} = \{\ddot{p}_1, \ddot{p}_2, \cdots \ddot{p}_N\}^T.$$

Here, the Newmark's time-stepping scheme has been used for the discretization of time dimension [22,23], which is a commonly used implicit method for the second-order propagation equations such as Eq. (4).

To form an image from a presumably uniform initial guess of the absorbed energy density distribution, we need a method of updating Φ from its starting value. This update is accomplished through the least-squares minimization of the following functional:

$$F(p, \Phi) = \sum_{j=1}^{M} (p_j^0 - p_j^c)^2, \quad (5)$$

where p_j^0 and p_j^c are observed and computed acoustic field data for $j = 1, 2, \cdots M$ boundary locations. Using the regularized Newton method, we obtained the following equation for updating Φ:

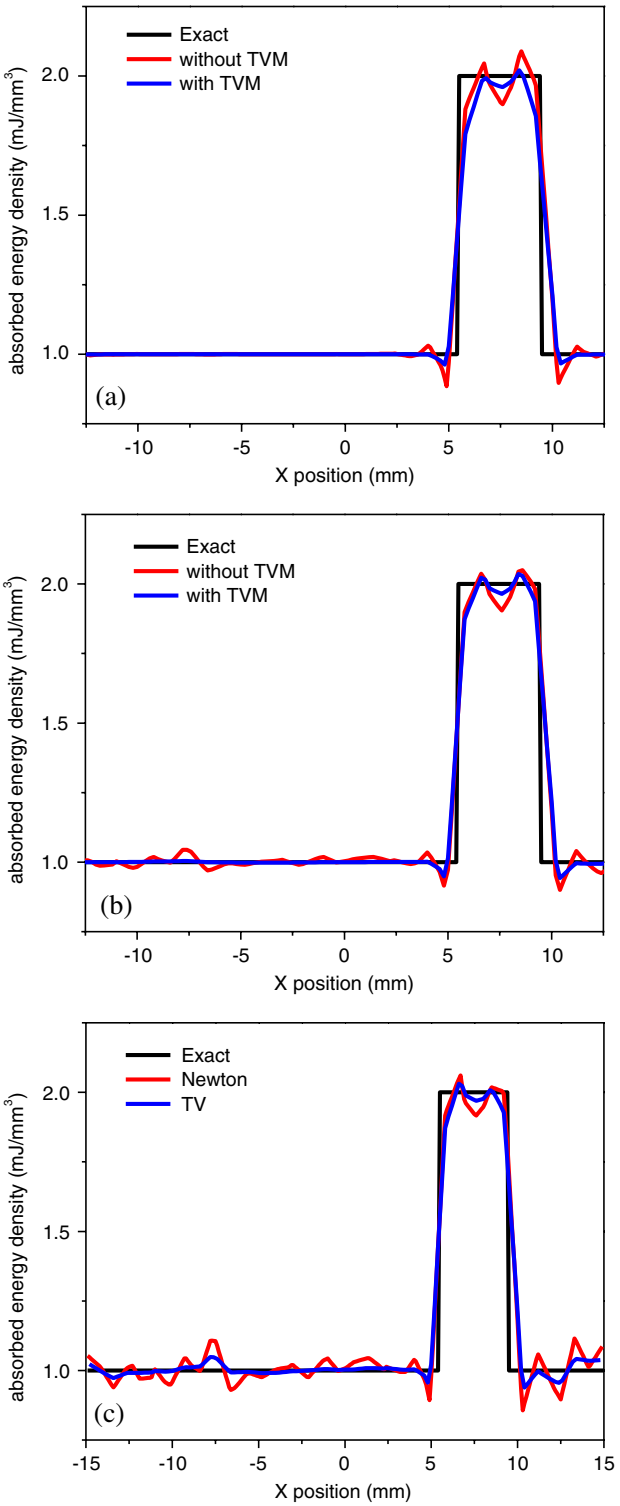

Fig. 2. (Color online) Comparison of the exact and reconstructed absorbed energy density profiles along transect $y = 0$ mm for the images appearing in Fig. 1. (a) 0% noise, (b) 10% noise, (c) 25% noise.

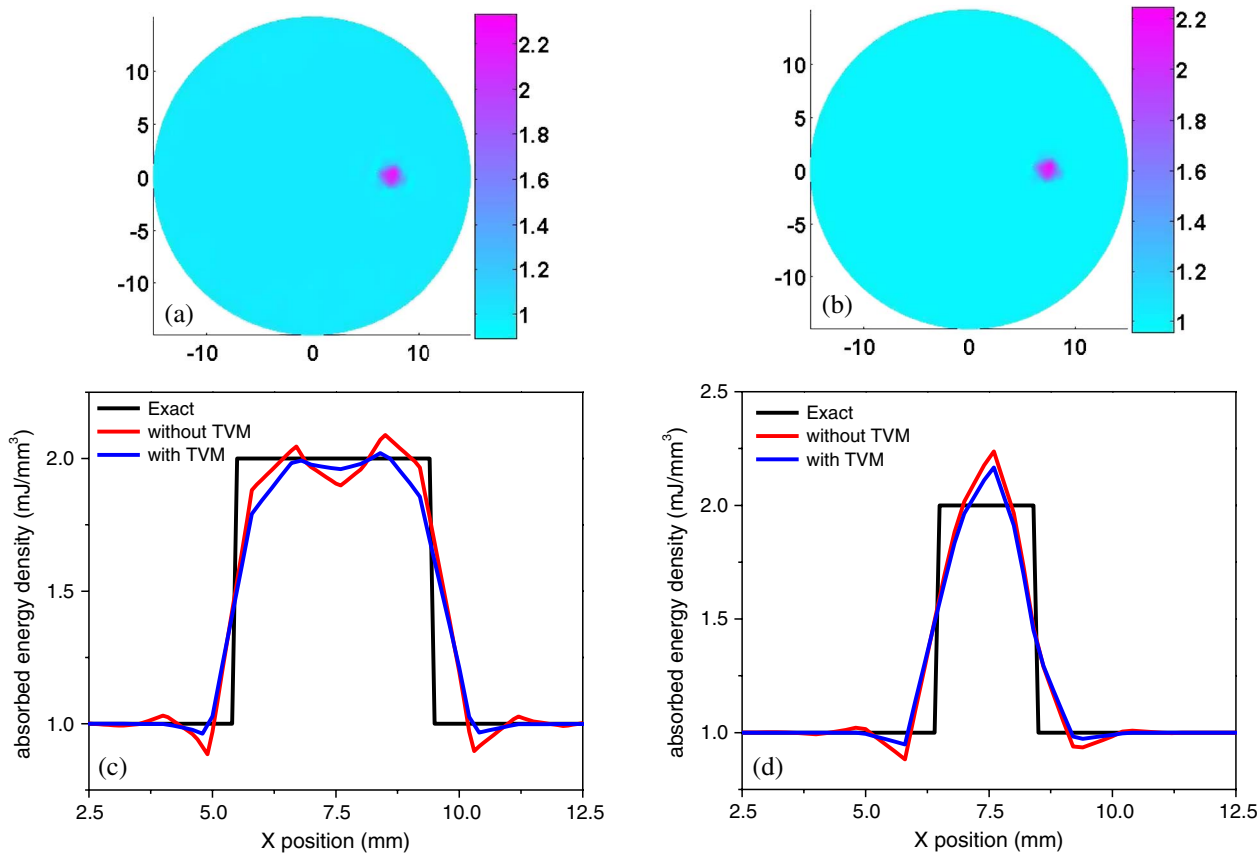

Fig. 3. (Color online) Reconstructed absorbed energy density images from simulated data with and without the TVM enhancement with different target sizes (case 2). (a) Without the TVM, 2 mm diameter target; (b) with the TVM, 2 mm diameter target; (c) absorbed energy density profiles along the transect $y = 0$ mm for the images appearing in Figs. 1(a) and 1(b) (4 mm diameter target); (d) absorbed energy density property profiles along the transect $y = 0$ mm for the images appearing in Figs. 3(a) and 3(b) (2 mm diameter target). In (a) and (b), the axes (left and bottom) illustrate the spatial scale in millimeters, whereas the color scale (right) records the absorbed energy density in millijoules per cubed millimeter.

$$(\Im^T\Im + \lambda\mathbf{I})\Delta\chi = \Im^T(p^0 - p^c), \tag{6}$$

where $p^0 = (p_1^0, p_2^0, \cdots p_M^0)^T$, $p^c = (p_1^c, p_2^c, \cdots p_M^c)^T$, $\Delta\chi$ is the update vector for the absorbed optical energy density, $\Im$ is the Jacobian matrix formed by $\partial p/\partial\Phi$ at the boundary measurement sites, λ is the regularization parameter determined by combined Marquardt and Tikhonov regularization schemes, and $\mathbf{I}$ is the identity matrix.

Two typical approaches exist for minimizing total variation: a constrained minimization through the solution of the nonlinear PA equation [8,24] and an unconstrained minimization by addition of the total variation as a penalty term to the least-squares functional [10,13,14,25]. From a computational standpoint, unconstrained minimizations are much easier to implement and require fewer modifications to the existing algorithm [13]. Thus, in this study, the unconstrained TVM is used.

We now incorporate the total variation of Φ as a penalty term by defining a new functional [9,10,13]:

$$\tilde{F}(p,\Phi) = F(p,\Phi) + L(\Phi). \tag{7}$$

Here,

$$L(\Phi) = \int \sqrt{\omega_\Phi^2|\nabla\Phi|^2 + \delta^2}\,dxdy \tag{8}$$

is the penalty term, and ω_Φ and δ are typically positive parameters that need to be determined numerically. The minimization of Eq. (7) proceeds in standard fashion by the differentiation of $\tilde{F}$ with respect to each nodal parameter that constitutes the Φ distribution; simultaneously, all these relations are set to zero. These steps lead to the following nonlinear system of equations

$$\frac{\partial\tilde{F}}{\partial\Phi_i} = -\sum_{j=1}^{M}(p_j^o - p_j^c)\frac{\partial p_j^c}{\partial\Phi_i} + V_i, \qquad (i = 1,2\cdots N), \tag{9}$$

where

$$V_i = \frac{\partial L}{\partial\Phi_i} = \int \frac{\omega_\Phi^2\left[\left(\sum_{k=1}^N\Phi_k\frac{\partial\psi_k}{\partial x}\right)\frac{\partial\psi_i}{\partial x} + \left(\sum_{k=1}^N\Phi_k\frac{\partial\psi_k}{\partial y}\right)\frac{\partial\psi_i}{\partial y}\right]}{\sqrt{\omega_\Phi^2\left[\left(\sum_{k=1}^N\Phi_k\frac{\partial\psi_k}{\partial x}\right)^2 + \left(\sum_{k=1}^N\Phi_k\frac{\partial\psi_k}{\partial y}\right)^2\right] + \delta^2}} \times dxdy.$$

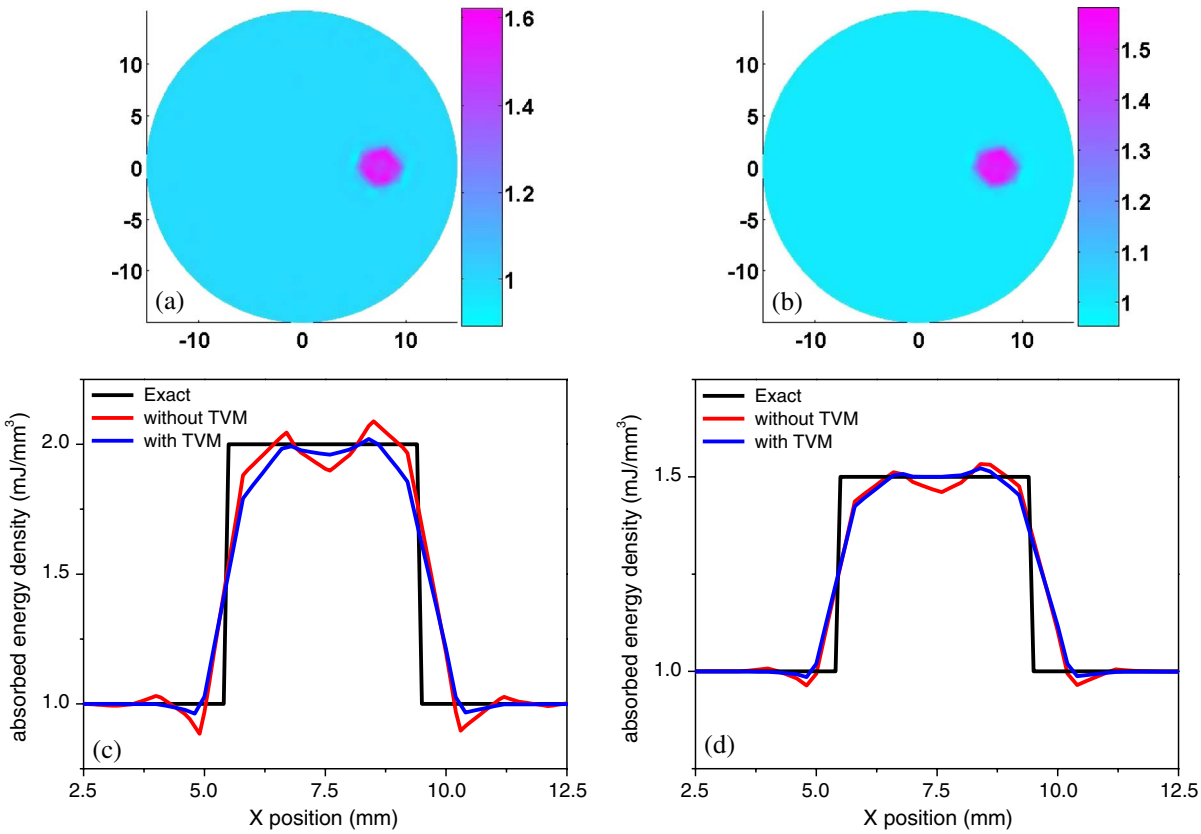

Fig. 4. (Color online) Reconstructed absorbed energy density images from simulated data with and without the TVM enhancement with different contrast levels between the target and the background (case 3). (a) Without the TVM, 1.5:1 contrast; (b) with the TVM, 1.5:1 contrast; (c) absorbed energy density profiles along the transect $y = 0$ mm for the images appearing in Figs. 1(a) and 1(b) (2:1 contrast); (d) absorbed energy density profiles along the transect $y = 0$ mm for the images appearing in Figs. 4(a) and 4(b) (1.5:1 contrast). In Figs. 4(a) and 4(b), the axes (left and bottom) illustrate the spatial scale in millimeters, whereas the color scale (right) records the absorbed energy density in millijoules per cubed millimeter.

Similar to Eq. (6), the following matrix equation for TVM constrained inversion can be obtained:

$$(\Im^T\Im + R + \lambda I)\Delta\chi = \Im^T(p^0 - p^c) - V, \qquad (10)$$

where

$$R = \begin{bmatrix} \frac{\partial V_1}{\partial \Phi_1}\frac{\partial V_1}{\partial \Phi_2}\cdots\frac{\partial V_1}{\partial \Phi_N} \\ \frac{\partial V_2}{\partial \Phi_1}\frac{\partial V_2}{\partial \Phi_2}\cdots\frac{\partial V_2}{\partial \Phi_N} \\ \cdots\ \vdots \\ \vdots\ \cdots\ \vdots \\ \frac{\partial V_N}{\partial \Phi_1}\frac{\partial V_N}{\partial \Phi_2}\cdots\frac{\partial V_N}{\partial \Phi_N} \end{bmatrix}$$

and $V = \{V_1, V_2, \cdots V_N\}^T$.

3. Results and Discussion

In this section, the TVM-enhanced reconstruction algorithm is tested and evaluated using both simulated and experimental data. For comparative purposes, reconstructions without the TVM enhancement are also presented.

A. Simulations

In these simulations, a dual-meshing method, as detailed elsewhere [6], is used for fast yet accurate inverse computation. The fine mesh used for the forward calculation consisted of 3627 nodes and 7072 elements, while the coarse mesh used for the inverse calculation had 930 nodes and 1768 elements. All the images obtained from the method without the TVM are the results of three iterations, while those obtained from the TVM-enhanced method are the results of 15 or more iterations. Parallel code was used to perform these calculations on Beowulf clusters with 8 central processing units (CPUs). The computational time can be further reduced if clusters with more than 8 CPUs are used. As mentioned earlier, the parameters ω_Φ and δ were determined through numerical experimentation. A constant value of $\delta = 0.001$ was sufficient for the current simulation and experimental studies, while the value of ω_Φ is related to the signal-to-noise ratio of the measurements [14]. For the simulations presented, $\omega_\Phi = 0.5$ for cases 1, 2, and 3, and $\omega_\Phi = 1.0$ for case 4 was used.

For the first simulation, the test geometry is a 30 mm diameter circular background containing an

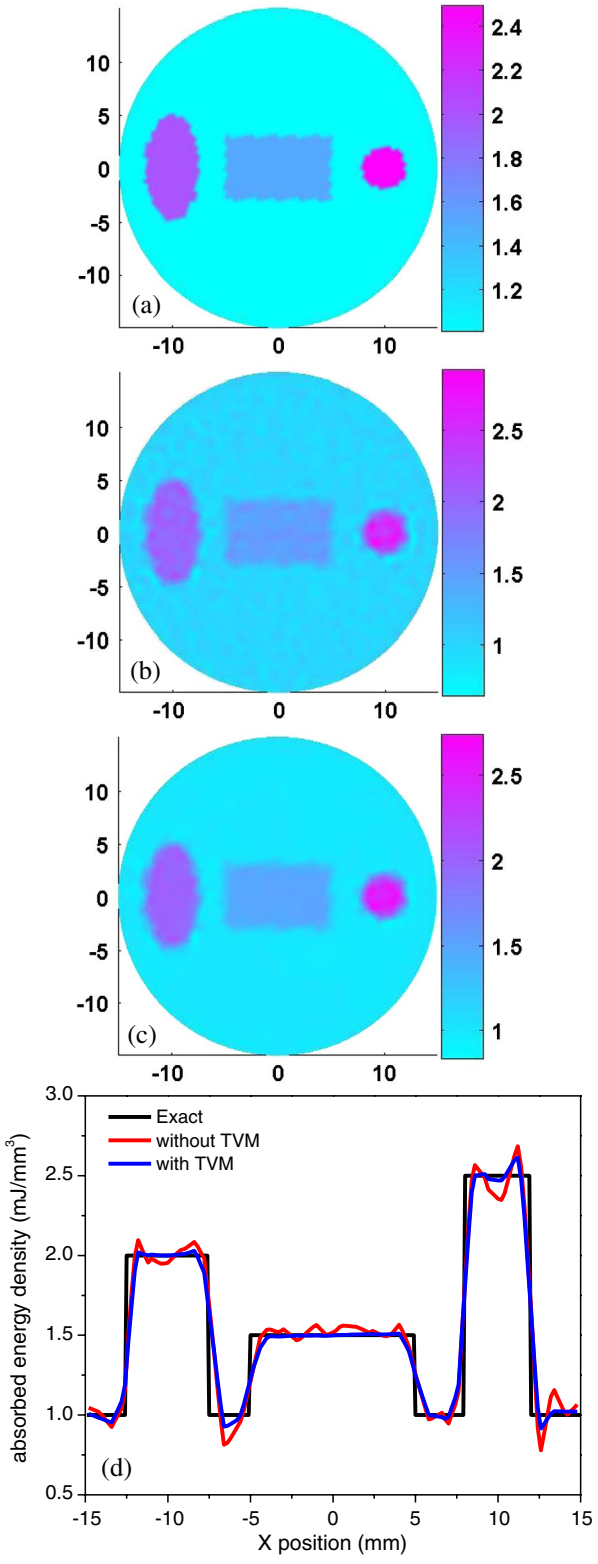

Fig. 5. (Color online) Reconstructed absorbed energy density images from simulated data with and without the TVM enhancement for three targets having different shapes (case 4). (a) Exact image, (b) without the TVM, (c) with the TVM, (d) absorbed energy density profiles along the transect $y = 0$ mm. In (a)–(c), the axes (left and bottom) illustrate the spatial scale in millimeters, whereas the color scale (right) records the absorbed energy density in millijoules per cubed millimeter.

off-center 4 mm diameter target region. The target had $\Phi = 2.0\,\mathrm{mJ/mm^3}$, while the background had $\Phi = 1.0\,\mathrm{mJ/mm^3}$. In this case, the image reconstruction was performed with 0%, 10%, and 25% noise added to the "measured" data. Figure 1 gives two sets of absorbed energy density images recovered using the reconstruction method without [Figs. 1(a), 1(c), and 1(e)] and with the TVM enhancement [Figs. 1(b), 1(d), and 1(f)] under the conditions of different noise levels. As can be seen, enhancement of the reconstruction by the incorporation of the TVM is obvious over the method without the TVM. To provide a more quantitative assessment of these images, Fig. 2 is included, in which the reconstructed absorbed energy density profiles are displayed along transects through the target for the images shown in Fig. 1. We find that the TVM-enhanced method not only can improve the quality of the recovered images, but also can decrease the sensitivity of the method to noise effect.

The second simulation is intended to investigate how the target size affects the TVM enhancement. In this case, no noise was added to the "measured" data, and the diameter of the off-center target was 2 mm. Figures 3(a) and 3(b) give two sets of absorbed energy density images recovered using the method without the TVM [Fig. 3(a)] and with the enhancement [Fig. 3(b)], while Figs. 3(c) and 3(d) present the quantitative profiles of the absorbed energy density along transects through the target for the images shown in Figs. 1(a), 1(b), 3(a), and 3(b). Again, considerable improvement can be observed from the reconstructed results when the TVM is invoked compared with the method without the TVM. It is also interesting to note that the enhancement for this case is more striking than that for the first one where the background contained a larger target.

The third simulation aims to see how the contrast level of the absorbed energy density between the target and the background impacts the TVM enhancement. In this case, no noise was added to the "measured" data, and the off-center target had a diameter of 4 mm and $\Phi = 1.5\,\mathrm{mJ/mm^3}$. Figures 4(a) and 4(b) present two sets of absorbed energy density images recovered using the method without the TVM [Fig. 4(a)] and with the TVM enhancement [Fig. 4(b)], while Figs. 4(c) and 4(d) show the quantitative profiles of the absorbed energy density along transects through the target for the images shown in Figs. 1(a), 1(b), 4(a), and 4(b). We can see that the images formed by incorporation of the TVM are clearly enhanced qualitatively in visual content relative to that obtained using the method without the TVM. We also note that lower the contrast level is, the larger the enhancement.

In the fourth simulation, three targets having different shapes (circular, elliptical, and rectangular) were embedded in the background, and the absorbed energy density of these targets was 2.5, 1.5, and $2.0\,\mathrm{mJ/mm^3}$, respectively. A noise level of 25% was added to the "measured" data in this case. Figure 5 shows the exact and the recovered absorbed energy density images as well as the quantitative absorbed

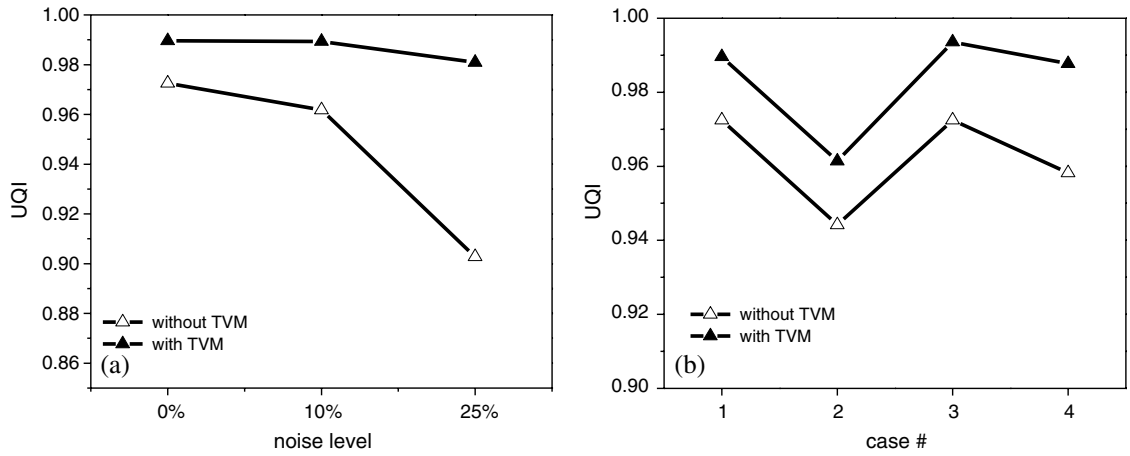

Fig. 6. UQI calculated from the recovered images with and without TVM enhancement from simulated data. (a) Case 1 when different noise levels are considered, (b) cases 2–4.

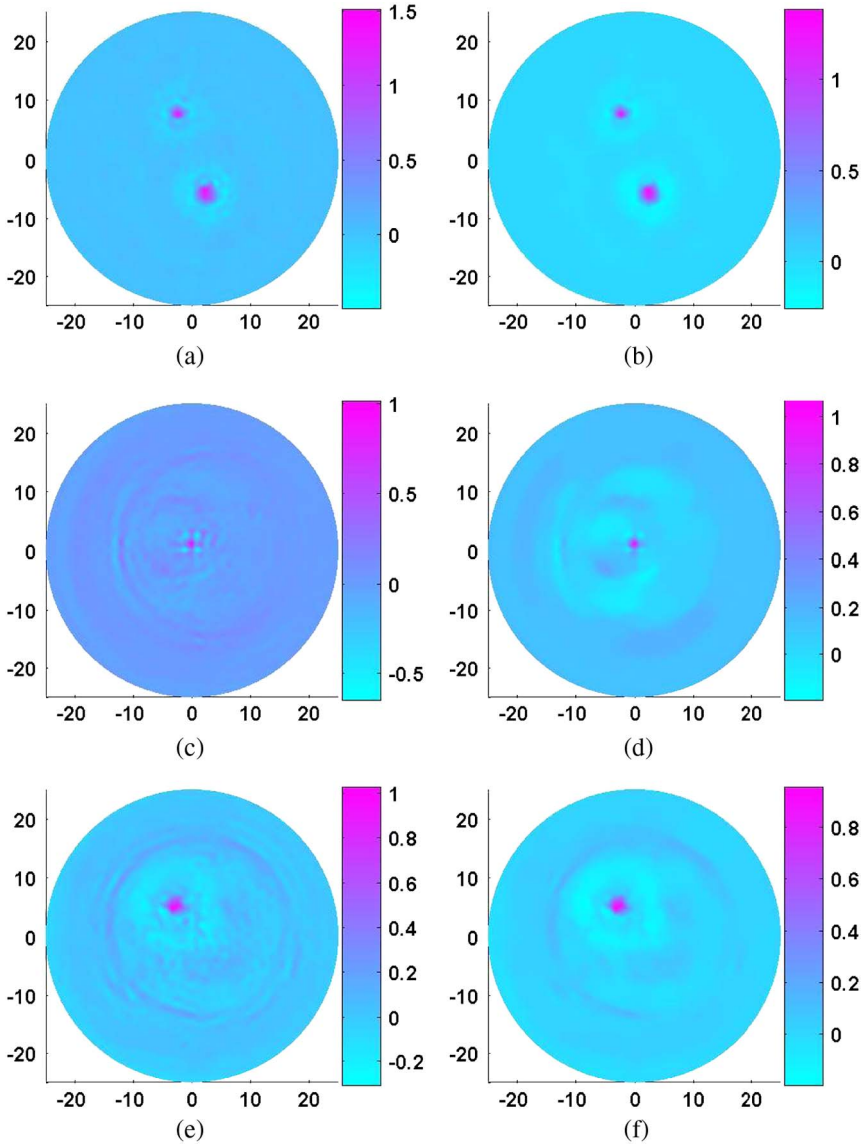

Fig. 7. (Color online) Reconstructed absorbed energy density images from the three phantom experiments. (a) Case 1 without the TVM, (b) case 1 with the TVM, (c) case 2 without the TVM, (d) case 2 with the TVM, (e) case 3 without the TVM, (f) case 3 with the TVM. The axes (left and bottom) illustrate the spatial scale in millimeters, whereas the color scale (right) records the absorbed energy density in millijoules per cubed millimeter.

energy density property profiles along the transect that across these targets. Again, the improvement in image quality is apparent.

In order to quantitatively evaluate the reconstruction quality using the reconstruction method with and without TVM enhancement, we used the universal quality index (UQI) to measure the degree of similarity between the reconstructed and exact images [26]. We first interpreted an image $\mathbf{f}$ as vectors of size $N : \mathbf{f} = (f_1, f_2, \cdots f_N)^T$, where superscript T denotes the matrix transpose, and N denotes the number of image data acquired from the FEM-based algorithm. We then defined image means, variances and covariances over the whole image domain as

$$\bar{f}^j = \frac{1}{N}\sum_{k=1}^{N} f_k^j, \tag{11}$$

$$\sigma^j = \sqrt{\frac{1}{N}\sum_{k=1}^{N}(f_k^j - \bar{f}^j)^2}, \tag{12}$$

where $j = 0$ and 1, and

$$\mathrm{Cov}\{\mathbf{f}^1, \mathbf{f}^0\} = \frac{1}{N}\sum_{k=1}^{N}(f_k^1 - \bar{f}^1)(f_k^0 - \bar{f}^0). \tag{13}$$

Hence, the UQI is defined as

$$\mathrm{UQI}\{\mathbf{f}^1, \mathbf{f}^0\} = \frac{2\mathrm{Cov}\{\mathbf{f}^1, \mathbf{f}^0\}}{(\sigma^1)^2 + (\sigma^0)^2}\frac{2\bar{f}^1\bar{f}^0}{(\bar{f}^1)^2 + (\bar{f}^0)^2}. \tag{14}$$

UQI measures the image similarity between the reconstructed ($\mathbf{f}^1$) and reference/exact ($\mathbf{f}^0$) images, and its value ranges between 0 and 1. The value of the UQI is closer to 1 when the reconstructed image is more similar to the exact image. We calculated the UQIs for the simulation cases presented earlier, and the results are given in Fig. 6, where Figs. 6(a) and 6(b) show the UQIs for case 1 when different noise level is considered and for all the four cases without added noise. In Fig. 6, the horizon axis indicates the case number (from cases 1 to 4, presented earlier), and

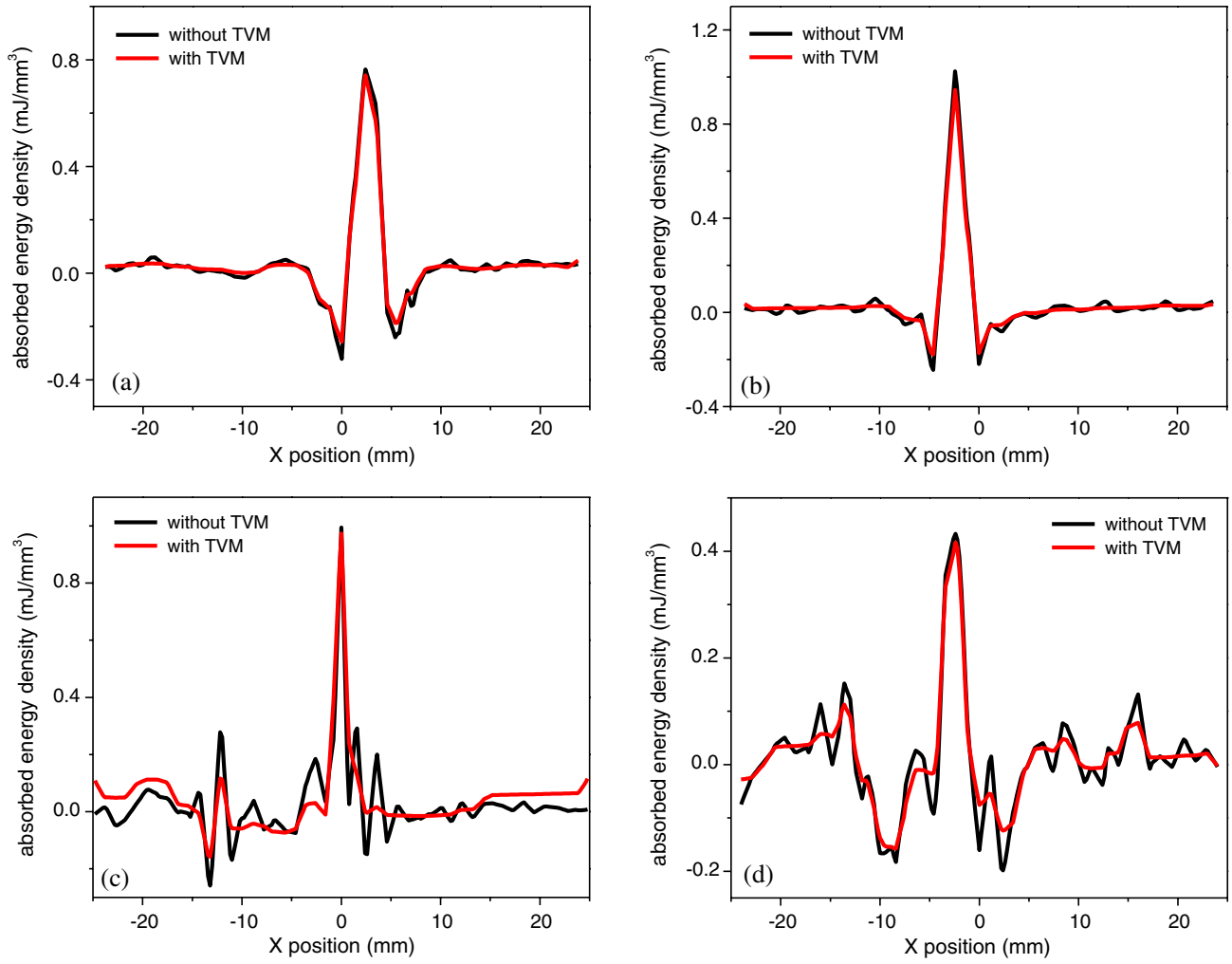

Fig. 8. (Color online) Recovered absorbed energy density profiles along (a) $y = -7.0$ mm crossing the 3 mm diameter target for experimental case 1, (b) $y = 8.0$ mm crossing the 2 mm diameter target for experimental case 1, (c) $y = 1.0$ mm for experimental case 2, and (d) $y = 6.5$ mm for experimental case 3.

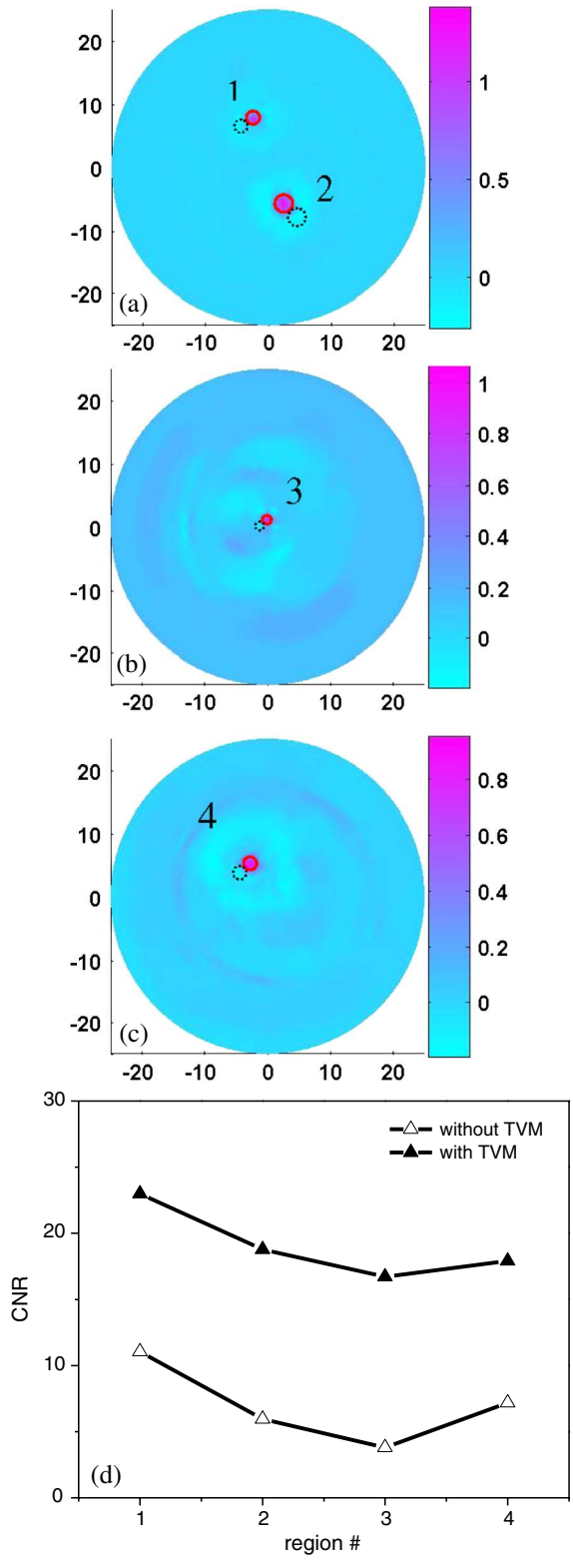

Fig. 9. (Color online) CNR calculated for the recovered images using the method with and without TVM. (a)–(c) Images shown in Figs. 7(b), 7(d), and 7(f) with the ROIs marked (four pairs of ROIs: solid line circle, *t*-ROI; dashed line circle, *b*-ROI). (d) CNR computed for the four pairs of ROIs shown in (a)–(c). In Figs. 9(a)–9(c), the axes (left and bottom) illustrate the spatial scale in millimeters, whereas the color scale (right) records the absorbed energy density in millijoules per cubed millimeter.

the vertical axis shows the value of UQI. We immediately note from Fig. 6 that the TVM-based method provides significantly better UQIs than that without TVM.

B. Phantom and *In Vivo* Experiments

In this section, both phantom and *in vivo* experimental data were used to confirm our findings from the simulations. The experimental setup used for collecting the phantom data was a pulsed Nd:YAG laser-based single transducer (1 MHz) scanning system, which was described in detail elsewhere [5]. Three phantom experiments were conducted. In the first two experiments, we embedded one or two objects with a size ranging from 3 to 0.5 mm in a 50 mm diameter solid cylindrical phantom. The phantom materials used consisted of Intralipid as a scatterer and India ink as an absorber with Agar powder (1%–2%) for solidifying the Intralipid and India ink solution. The absorption coefficient of the background phantom was $0.01\,\mathrm{mm}^{-1}$, while the absorption coefficient of the target(s) was $0.03\,\mathrm{mm}^{-1}$. In the last experiment, we used a single target-containing phantom, aiming to test the capability of detecting targets having low optical contrasts relative to the background phantom. In this case, the target had an absorption coefficient of $0.015\,\mathrm{mm}^{-1}$. The reduced scattering coefficients of the background phantom and targets were 1.0 and $3.0\,\mathrm{mm}^{-1}$ for the first two experiments, and 1.0 and $2.0\,\mathrm{mm}^{-1}$ for the last experiment.

A total of 120 receivers were equally distributed along the surface of the circular background region. In the reconstructions, the fine mesh used for the forward calculation consisted of 5977 nodes and 11,712 elements, while the coarse mesh used for the inverse calculation had 1525 nodes and 2928 elements. The reconstructed images were the results of three and 15 iterations for the method without and with the TVM, respectively. For these experimental cases, $\omega_\Phi = 1.0$ and $\delta = 0.001$ for the cases 1 and 3 and $\omega_\Phi = 2.0$ and $\delta = 0.001$ for case 2 were used.

Here we note that, in the experimental situation, the effect of ultrasonic transducer response should be considered in the PAT image reconstruction because the transducer mechanical–electrical impulse response as well as the transducer aperture effect may introduce significant errors in the forward model. To reduce these effects in our calculations, we applied the normalized acoustic pressure distribution in the reconstruction and used the appropriate parameters (initial values, etc.) obtained from an optimization/searching method [27].

Figure 7 shows the reconstructed absorbed energy density images for all the three experimental cases, while Fig. 8 presents quantitative absorption coefficient profiles along transects through one target for the images shown in Fig. 7. We see that considerably enhanced images are achieved with the TVM, especially when the target is small (case 2), or when the

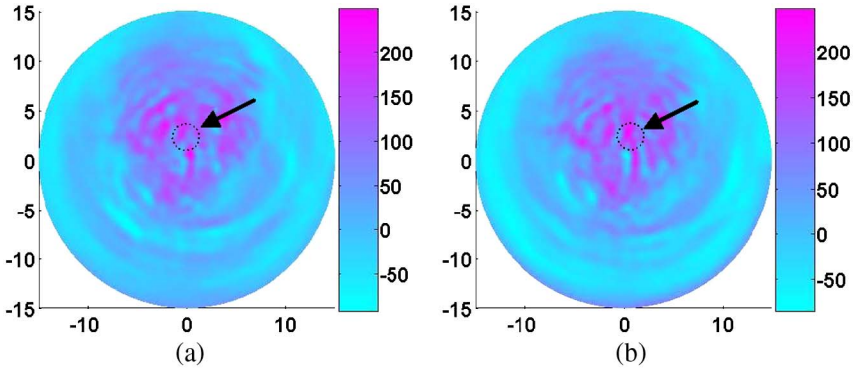

Fig. 10. (Color online) Recovered absorbed energy density images from the rat brain (a) without the TVM, (b) with the TVM. The axes (left and bottom) illustrate the spatial scale in millimeters, whereas the color scale (right) records the absorbed energy density in millijoules per cubed millimeter.

contrast level between the target and the background is low (case 3).

Because there is no true or exact image available for the experimental cases, we used the contrast-to-noise ratio (CNR) to quantitatively evaluate the experimental results. To compute CNR, we selected two regions of interest (ROIs), each having the same size. One region is in the target (referred as t-ROI) and the other is in the background (denoted as b-ROI). The CNR is defined as

$$\mathrm{CNR} = \frac{|\bar{f}^{(t)} - \bar{f}^{(b)}|}{\sigma^{(b)}}, \tag{15}$$

where $\bar{f}^{(t)}$ and $\bar{f}^{(b)}$, respectively, denote the mean over the t-ROI and b-ROI, and $\sigma^{(b)}$ denotes the variances over the b-ROI. We used solid and dashed circles to express the t-ROI and b-ROI for the three experimental cases. We calculated the CNR for each pair of the t- and b-ROIs using Eq. (15) and present the results in Fig. 9(d). We see that the CNR obtained using the method with TVM is clearly larger than that using the method without TVM, indicating that the TVM-based method is less sensitive to the noise effects.

As a final example, our methods were tested using *in vivo* data collected previously from an animal (rat) model of epilepsy [28]. Focal seizures were induced by microinjection of bicuculline methiodide (BMI) into the parietal neocortex. The *in vivo* data were collected using the same pulsed Nd:YAG laser-based scanning PAT system. In the reconstruction, the fine mesh used for the forward calculation consisted of 17,713 nodes and 34,944 elements, while the coarse mesh used for the inverse calculation had 4489 nodes and 8736 elements. The *in vivo* images obtained were the results of two and five iterations for the methods without and with the TVM, respectively. We found that $\omega_\Phi = 0.1$ and $\delta = 0.001$ appeared to provide optimal results.

Figure 10 gives the recovered images for the rat brain scanned 10 min after the injection of BMI without and with the use of the TVM. The *in vivo* results shown here confirm that both of the reconstruction methods can provide quality images (the arrow indicates the detected seizure focus), while notable enhancement in image quality can be observed with the TVM-based method. For example, the actual continuous middle cerebral artery (indicated by the dashed circle) is shown discontinued in Fig. 10(a) (without the TVM), while this feature is clearly depicted in Fig. 10(b) (with the TVM).

4. Conclusions

We have presented a time-domain FEM-based PA image reconstruction method that incorporates the TVM. The results shown in this work indicate that the TVM-based method is able to offer clear enhancement in image reconstruction over the method without the TVM, not only in terms of the location, size, and shape of the target, but also in terms of the absorbed energy density property/optical absorption coefficient values themselves. In addition, the results have shown that the inclusion of the TVM in our reconstruction algorithm is highly effective in the presence of noisy data. Finally, it is important to note that the TVM-based method may be ideal for image reconstruction involving a low contrast level between the target and the background or small targets embedded in the background.

This research was supported in part by the Department of Defense Congressionally Directed Medical Program.

References

1. G. Paltauf, J. Viator, S. Prahl, and S. Jacques, "Iterative reconstruction algorithm for optoacoustic imaging," J. Acoust. Soc. Am. **112**, 1536–1544 (2002).
2. S. J. Norton and T. Vo-Dinh, "Optoacoustic diffraction tomography: analysis of algorithms," J. Opt. Soc. Am. A **20**, 1859–1866 (2003).
3. A. A. Oraevsky, A. A. Karabutov, S. V. Solomatin, E. V. Savateeva, V. A. Andreev, Z. Gatalica, H. Singh, and R. D. Fleming, "Laser optoacoustic imaging of breast cancer in vivo," Proc. SPIE **4256**, 6–15 (2001).
4. Z. Yuan and H. Jiang, "Quantitative photoacoustic tomography: recovery of optical absorption coefficient maps of heterogenous media," Appl. Phys. Lett. **88**, 231101 (2006).

5. L. Yin, Q. Wang, Q. Zhang, and H. Jiang, "Tomographic imaging of absolute optical absorption coefficient in turbid media using combined photoacoustic and diffusing light measurements," Opt. Lett. **32**, 2556–2558 (2007).
6. H. Jiang, Z. Yuan, and X. Gu, "Spatially varying optical and acoustic property reconstruction using finite-element-based photoacoustic tomography," J. Opt. Soc. Am. A **23**, 878–888 (2006).
7. L. Yao and H. Jiang, "Finite-element-based photoacoustic tomography in time-domain," J. Opt. A **11**, 085301 (2009).
8. K. D. Paulsen and H. Jiang, "Spatially-varying optical property reconstruction using finite element diffusion equation approximation," Med. Phys. **22**, 691–702 (1995).
9. S. R. Arridge, "Forward and inverse problems in time-resolved infrared imaging," in *Medical Optical Tomography: Functional Imaging and Monitoring*, G. J. Mueller, B. Chance, R. R. Alfano, S. B. Arridge, J. Beuthen, E. Gratton, M. Kaschke, B. R. Masters, S. Svanberg, and P. van der Zee, eds., SPIE Institute Series (SPIE, 1993), Vol. IS11, pp. 35–64.
10. D. C. Dobson and F. Santosa, "An image-enhancement technique for electrical impedance tomography," Inverse Probl. **10**, 317–334 (1994).
11. P. M. van den Berg and R. E. Kleinmann, "A total variation enhanced modified gradient algorithm for profile reconstruction," Inverse Probl. **11**, L5–L10 (1995).
12. C. R. Vogel and M. E. Oman, "Iterative methods for total variation denoising," SIAM J. Sci. Comput. **17**, 227–238 (1996).
13. D. C. Dobson and F. Santosa, "Recovery of blocky images from noisy and blurred data," SIAM J. Appl. Math. **56**, 1181–1198 (1996).
14. D. C. Dobson, "Exploiting ill-posedness in the design of diffractive optical structures," Proc. SPIE **1919**, 248–257 (1993).
15. R. Acar and C. R. Vogel, "Analysis of bounded variation penalty methods for ill-posed problems," Inverse Probl. **10**, 1217–1229 (1994).
16. K. D. Paulsen and H. Jiang, "Enhanced frequency-domain optical image reconstruction in tissues through total-variation minimization," Appl. Opt. **35**, 3447–3458 (1996).
17. K. Wang, E. Y. Sidky, M. A. Anastasio, A. A. Oraevsky, and X. Pan, "Limited data image reconstruction in optoacoustic tomography by constrained total variation minimization," Proc. SPIE **7899**, 78993U (2011).
18. J. Provost and F. Lesage, "The application of compressed sensing for photo-acoustic tomography," IEEE Trans. Med. Imaging **28**, 585–594 (2009).
19. Z. Guo, C. Li, L. Song, and L. V. Wang, "Compressed sensing in photoacoustic tomography in vivo," J. Biomed. Opt. **15**, 021311 (2010).
20. A. C. Tam, "Applications of photoacoustic sensing techniques," Rev. Mod. Phys. **58** 381–430 (1986)
21. A. Bayliss and E. Turkel, "Radiation boundary conditions for wave-like equations," Commun. Pure Appl. Math. **33**, 707–725 (1980).
22. I. M. Smith and D. V. Griffiths, *Programming the Finite Element Method* (Wiley, 2004).
23. O. C. Zienkiewicz, R. L. Taylor, and J. Z. Zhu, *Finite Element Method: Its Basis and Fundamentals* (Butterworth, 2005).
24. L. I. Rudin, S. Osher, and E. Fatemi, "Nonlinear total variation based noise removal algorithm," Physica D **60**, 259–268 (1992).
25. S. R. Arridge, P. van der Zee, M. Cope, and D. Delpy, "Reconstruction methods for infrared absorption imaging," Proc. SPIE **1431**, 204–215 (1991).
26. Z. Wang and A. Bovik, "A universal image quality index," IEEE Signal Process. Lett. **9**, 81–84 (2002).
27. N. Iftimia and H. Jiang, "Quantitative optical image reconstruction of turbid media by use of direct-current measurements," Appl. Opt. **39**, 5256–5261 (2000).
28. Q. Zhang, Z. Liu, P. R. Carney, Z. Yuan, H. Chen, S. N. Roper, and H. Jiang, "Non-invasive imaging of epileptic seizures *in vivo* using photoacoustic tomography," Phys. Med. Biol. **53**, 1921–1931 (2008).

Photoacoustic image reconstruction from few-detector and limited-angle data

Lei Yao and Huabei Jiang*

Department of Biomedical Engineering, University of Florida, Gainesville, FL 32611, USA
**hjiang@bme.ufl.edu*

Abstract: Photoacoustic tomography (PAT) is an emerging non-invasive imaging technique with great potential for a wide range of biomedical imaging applications. However, the conventional PAT reconstruction algorithms often provide distorted images with strong artifacts in cases when the signals are collected from few measurements or over an aperture that does not enclose the object. In this work, we present a total-variation-minimization (TVM) enhanced iterative reconstruction algorithm that can provide excellent photoacoustic image reconstruction from few-detector and limited-angle data. The enhancement is confirmed and evaluated using several phantom experiments.

OCIS codes: (100.2980) Image enhancement; (170.3010) Image reconstruction techniques; (170.5120) Photoacoustic imaging; (170.6960) Tomography

References and links

1. G. Paltauf, J. A. Viator, S. A. Prahl, and S. L. Jacques, "Iterative reconstruction algorithm for optoacoustic imaging," J. Acoust. Soc. Am. **112**(4), 1536–1544 (2002).
2. S. J. Norton and T. Vo-Dinh, "Optoacoustic diffraction tomography: analysis of algorithms," J. Opt. Soc. Am. A **20**(10), 1859–1866 (2003).
3. A. A. Oraevsky, A. A. Karabutov, S. V. Solomatin, E. V. Savateeva, V. A. Andreev, Z. Gatalica, H. Singh, and R. D. Fleming, "Laser optoacoustic imaging of breast cancer in vivo," Proc. SPIE **4256**, 6–15 (2001).
4. L. A. Kunyansky, "Explicit inversion formulae for the spherical mean radon transform," Inverse Probl. **23**(1), 373–383 (2007).
5. D. Finch, S. Patch, and Rakesh, "Determining a Function from Its Mean Values Over a Family of Spheres," SIAM J. Math. Anal. **35**(5), 1213–1240 (2004).
6. M. Xu and L. V. Wang, "Universal back-projection algorithm for photoacoustic computed tomography," Phys. Rev. E Stat. Nonlin. Soft Matter Phys. **71**(1), 016706 (2005).
7. Z. Yuan and H. Jiang, "Quantitative photoacoustic tomography: Recovery of optical absorption coefficient maps of heterogenous media," Appl. Phys. Lett. **88**(23), 231101 (2006).
8. L. Yin, Q. Wang, Q. Zhang, and H. Jiang, "Tomographic imaging of absolute optical absorption coefficient in turbid media using combined photoacoustic and diffusing light measurements," Opt. Lett. **32**(17), 2556–2558 (2007).
9. K. D. Paulsen and H. Jiang, "Spatially varying optical property reconstruction using a finite element diffusion equation approximation," Med. Phys. **22**(6), 691–701 (1995).
10. S. R. Arridge, "Forward and inverse problems in time-resolved infrared imaging," in *Medical Optical Tomography: Functional Imaging and Monitoring*, G. J. Mueller, B. Chance, R. R. Alfano, S. B. Arridge, J. Beuthen, E. Gratton, M. Kaschke, B. R. Masters, S. Svanberg, and P. van der Zee, eds. (SPIE Press, 1993), pp. 35–64.
11. S. J. LaRoque, E. Y. Sidky, and X. Pan, "Accurate image reconstruction from few-views and limited-angle data in diffraction tomography," J. Opt. Soc. Am. A **25**(7), 1772–1782 (2008).
12. J. Bian, J. H. Siewerdsen, X. Han, E. Y. Sidky, J. L. Prince, C. A. Pelizzari, and X. Pan, "Evaluation of sparse-view reconstruction from flat-panel-detector cone-beam CT," Phys. Med. Biol. **55**(22), 6575–6599 (2010).
13. H. Ammari, E. Bretin, V. Jugnon, and A. Wahab, "Photo-acoustic imaging for attenuating acoustic media," in *Mathematical Modeling in Biomedical Imaging II*, H. Ammari, ed., Vol. 2035 of Lecture Notes in Mathematics (Springer, 2011), pp. 53–80.
14. H. Ammari, E. Bossy, V. Jugnon, and H. Kang, "Mathematical models in photoacoustic imaging of small absorbers," SIAM Rev. **52**(4), 677–695 (2010).
15. H. Ammari, E. Bossy, V. Jugnon, and H. Kang, "Reconstruction of the optical absorption coefficient of a small absorber from the absorbed energy density," SIAM J. Appl. Math. **71**, 676–693 (2011).

#151589 - $15.00 USD Received 22 Jul 2011; revised 19 Aug 2011; accepted 19 Aug 2011; published 19 Aug 2011

16. K. Wang, E. Y. Sidky, M. A. Anastasio, A. A. Oraevsky, and X. Pan, "Limited data image reconstruction in optoacoustic tomography by constrained total variation minimization," Proc. SPIE **7899**, 78993U, 78993U-6 (2011).
17. L. Yao and H. Jiang, "Finite-element-based photoacoustic tomography in time-domain," J. Opt. A, Pure Appl. Opt. **11**(8), 085301 (2009).
18. K. D. Paulsen and H. Jiang, "Enhanced frequency-domain optical image reconstruction in tissues through total-variation minimization," Appl. Opt. **35**(19), 3447–3458 (1996).
19. H. Jiang, Z. Yuan, and X. Gu, "Spatially varying optical and acoustic property reconstruction using finite-element-based photoacoustic tomography," J. Opt. Soc. Am. A **23**(4), 878–888 (2006).
20. Z. Wang and A. C. Bovik, "A universal image quality index," IEEE Signal Process. Lett. **9**(3), 81–84 (2002).

1. Introduction

Photoacoustic tomography (PAT) is an emerging non-invasive imaging technique that combines the merits of high optical contrast and high ultrasound resolution in a single modality [1–3]. In PAT, the Helmholtz-like photoacoustic wave equation has been commonly used as an accurate model for describing laser-induced acoustic wave propagation in tissue. While a variety of analytic PAT reconstruction algorithms have been developed [4–6], the finite element method (FEM) based approach appears to be particularly powerful in this regard, because it can provide quantitative imaging capability by recovering optical absorption coefficient [7,8], eliminate the assumption of homogeneous acoustic medium needed in analytical methods, accommodate object boundary irregularity and allow appropriate boundary conditions implementations.

A practical need exists for reconstruction of photoacoustic images from few measurements, as this can greatly reduce the required scanning time and the number of ultrasound sensors placed near or on the boundary of an object to receive the laser-induced acoustic signals. In addition, in many practical implementations of PAT the photoacoustic signals are recorded over an aperture that does not enclose the object, which results in a limited-angle tomographic reconstruction problem. In such cases, the existing reconstruction algorithms, which are based on the least-squares criteria (i.e., the regularized Newton method) [9,10], often generate distorted images with severe artifacts. Total-variation-minimization (TVM), on the other hand, has proved to be a powerful tool for limited-data image reconstruction in diffraction tomography and computed tomography (CT) [11,12]. TVM based PAT algorithms have also been implemented and tested using numerically simulated limited-view data [13–16]. Here we describe an unconstrained TVM FEM-based iterative reconstruction algorithm, and for the first time present experimental evidence that the TVM-based algorithm offers excellent photoacoustic image reconstruction from few-detector and limited-angle data.

This paper is organized as follows. In Section 2, the FEM based PAT reconstruction algorithm and the unconstrained TVM scheme are reviewed briefly. The experimental validation of our TVM FEM-based algorithm is presented in Section 3. The conclusions are made in Section 4.

2. Method

We first briefly describe the existing FEM-based photoacoustic reconstruction algorithm detailed elsewhere [17]. The time-domain photoacoustic wave equation in tissue can be described as follows:

$$\nabla^2 p(\mathbf{r},t) - \frac{1}{v_0^2}\frac{\partial^2 p(\mathbf{r},t)}{\partial t^2} = -\frac{\Phi(\mathbf{r})\beta}{C_p}\frac{\partial J(t)}{\partial t}, \tag{1}$$

where p is the pressure wave; v_0 is the speed of acoustic wave in the medium; β is the thermal expansion coefficient; C_p is the specific heat; Φ is the absorbed energy density; $J(t) = \delta(t - t_0)$ is assumed in our study.

#151589 - $15.00 USD Received 22 Jul 2011; revised 19 Aug 2011; accepted 19 Aug 2011; published 19 Aug 2011

To form an image from a presumably uniform initial guess of the absorbed energy density distribution, we need a method of updating Φ, the desired quantity from its starting value. This update is accomplished through the least-squares minimization of the following functional:

$$F\left(p,\Phi\right)=\sum_{j=1}^{M}\left(p_j^0-p_j^c\right)^2, \tag{2}$$

where p_j^o and p_j^c are the measured and computed acoustic field data for $i=1,2,\cdots M$ boundary locations. Using the regularized Newton method, we obtained the following matrix equation for updating Φ:

$$\left(\Im^T\Im+\lambda\mathbf{I}\right)\Delta\chi=\Im^T\left(p^o-p^c\right), \tag{3}$$

where $p^0=\left(p_1^0,p_2^0,\cdots p_M^0\right)^T$ and $p^c=\left(p_1^c,p_2^c,\cdots p_M^c\right)^T$; $\Delta\chi$ is the update vector for the absorbed optical energy density; $\Im$ is the Jacobian matrix formed by $\partial p/\partial\Phi$ at the boundary measurement sites; λ is the regularization parameter determined by combined Marquardt and Tikhonov regularization schemes; and **I** is the identity matrix.

We now incorporate the total variation of Φ as a penalty term by defining a new functional [18]:

$$\tilde{F}\left(p,\Phi\right)=F\left(p,\Phi\right)+L\left(\Phi\right). \tag{4}$$

Here $L\left(\Phi\right)=\int\sqrt{\omega_\Phi^2\left|\nabla\Phi\right|^2+\delta^2}\,dxdy$ is the penalty term, and ω_Φ and δ are typically positive parameters that need to be determined numerically. The minimization of Eq. (4) can be realized by the differentiation of $\tilde{F}$ with respect to each nodal parameter that constitutes the Φ distribution and by setting each of the resulting expression to zero, leading to the following system of equations:

$$\frac{\partial\tilde{F}}{\partial\Phi_i}=-\sum_{j=1}^{M}\left(p_j^o-p_j^c\right)\frac{\partial p_j^c}{\partial\Phi_i}+V_i=0\quad\left(i=1,2\cdots N\right), \tag{5}$$

where $V_i=\partial L/\partial\Phi_i$. Again, through the regularized Newton method, the following matrix equation for TVM-based inversion is obtained [18]:

$$\left(\Im^T\Im+R+\lambda I\right)\Delta\chi=\Im^T\left(p^0-p^c\right)-V, \tag{6}$$

where V is formed by $\partial L/\partial\Phi$ and R is formed by $\partial V/\partial\Phi$. At this point, our solution procedure for solving Eq. (6) and the regularization parameter selection are identical to those described previously. Hence, it becomes clear that the only additions to our new algorithm result from the assembly of matrix R and the construction of column vector V.

3. Results

In this section our TVM enhanced reconstruction algorithm is tested and evaluated using phantom experimental data. For comparative purposes, reconstruction results without the TVM enhancement are also presented.

The experimental setup used for collecting the phantom data was a pulsed ND: YAG laser based single transducer (1MHz) scanning system, which was described in detail elsewhere [8]. Three phantom experiments were conducted. In the first two experiments, we embedded one or two objects with a size ranging from 3 to 0.5 mm in a 50 mm-diameter solid cylindrical phantom. The absorption coefficient of the background phantom was 0.01 mm^{-1}, while the

#151589 - $15.00 USD Received 22 Jul 2011; revised 19 Aug 2011; accepted 19 Aug 2011; published 19 Aug 2011

absorption coefficient of the target(s) was 0.03 mm^{-1}. In the last experiment, we used a single-target-containing phantom, aiming to test the capability of detecting target having low optical contrasts relative to the background phantom. In this case, the target had an absorption coefficient of 0.015 mm^{-1}. The reduced scattering coefficients of the background phantom and targets were 1.0 and 3.0 mm^{-1} for the first two experiments, and 1.0 and 2.0 mm^{-1} for the last experiment. In the reconstructions, we used a dual-meshing scheme [19] where the fine mesh used for the forward calculation consisted of 5977 nodes and 11712 elements, while the coarse mesh used for the inverse calculation had 1525 nodes and 2928 elements. All the images obtained from the method without the TVM are the results of three iterations, while those obtained from the TVM-enhanced method are the results of twenty or more iterations. Parallel code was used to speed up these calculations on Beowulf clusters with 8 CPUs. The computational speed can be further increased if clusters with more than 8 CPUs are used. As mentioned above, the parameters ω_Φ and δ were determined through numerical experimentation. From our experience, a constant value of $\delta = 0.001$ was sufficient for the current experimental studies, while the value of ω_Φ is related to the signal-to-noise ratio of the measurements. For our experimental cases, $\omega_\Phi = 1.0$ and $\delta = 0.001$ for the first case, and $\omega_\Phi = 0.5$ and $\delta = 0.001$ for the second and third cases were used.

The reconstruction results based on few-detector data from the three experimental cases are shown in Figs. 1, 2 and 3, respectively. In each figure, the images in the top and bottom rows, respectively, present the recovered absorbed energy density images using the algorithm without and with the TVM where 120, 60, 30, and 15 detectors were equally distributed along the surface of the circular background region. As expected, the conventional algorithm without the TVM provides high quality images only when the number of detectors was relatively sufficient (Figs. 1a,b, Figs. 2a,b, and Figs. 3a,b). The images reconstructed from few-detector data by the conventional algorithm without the TVM contained severe artifacts and distortions (Figs. 1c,d, Figs. 2c,d, and Figs. 3c,d). Considerably enhanced images are achieved using the method with the TVM, especially when the number of the detectors is reduced to 30 or 15 (Figs. 1g,h, Figs. 2g,h, and Figs. 3g,h). We also note that the computational efficiency of our TVM based algorithm for recovering a small absorber (Fig. 2) and a larger absorber (Fig. 3) is similar when the number of the detectors is insufficient.

Images reconstructed from the limited-angle data for the first case using the two methods are displayed in Fig. 4 where the top and bottom rows, respectively, show the recovered absorbed energy density images using the algorithm without and with the TVM when 120 detectors over 360°, 60 detectors over 180°, and 30 detectors over 90°, were equally

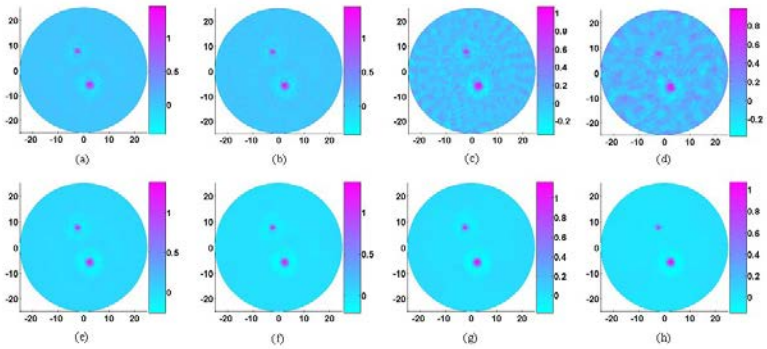

Fig. 1. Reconstructed photoacoustic images based on few-detector data for case 1. (a), 120 detectors, without TVM. (b), 60 detectors, without TVM. (c), 30 detectors, without TVM. (d), 15 detectors, without TVM. (e), 120 detectors, with TVM. (f), 60 detectors, with TVM. (g), 30 detectors, with TVM. (h), 15 detectors, with TVM.

#151589 - $15.00 USD Received 22 Jul 2011; revised 19 Aug 2011; accepted 19 Aug 2011; published 19 Aug 2011

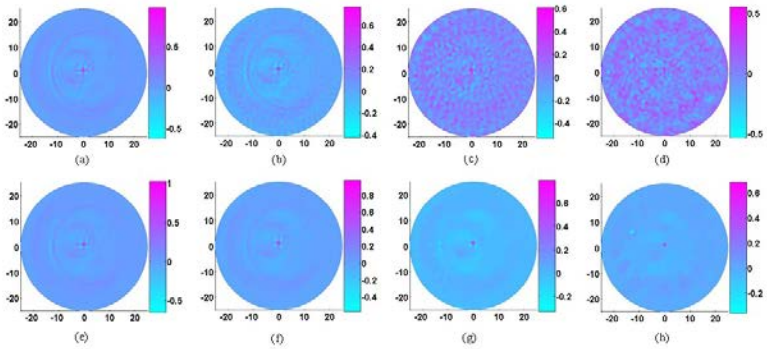

Fig. 2. Reconstructed photoacoustic images based on few-detector data for case 2. (a), 120 detectors, without TVM. (b), 60 detectors, without TVM. (c), 30 detectors, without TVM. (d), 15 detectors, without TVM. (e), 120 detectors, with TVM. (f), 60 detectors, with TVM. (g), 30 detectors, with TVM. (h), 15 detectors, with TVM.

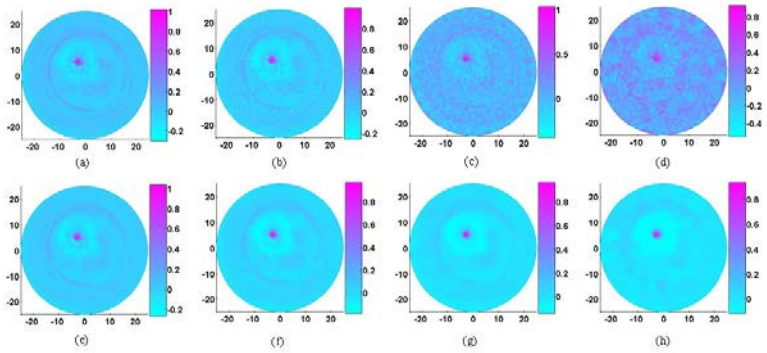

Fig. 3. Reconstructed photoacoustic images based on few-detector data for case 3. (a), 120 detectors, without TVM. (b), 60 detectors, without TVM. (c), 30 detectors, without TVM. (d), 15 detectors, without TVM. (e), 120 detectors, with TVM. (f), 60 detectors, with TVM. (g), 30 detectors, with TVM. (h), 15 detectors, with TVM.

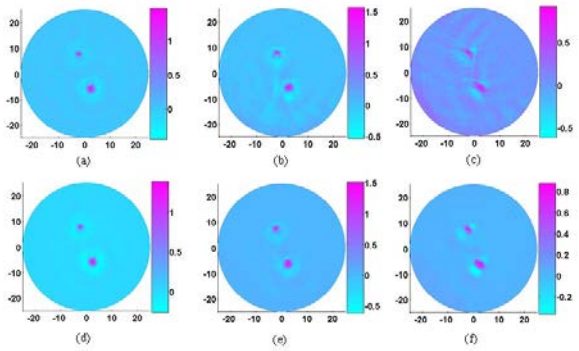

Fig. 4. Reconstructed photoacoustic images based on limited-angle data for case 1. (a), 120 detectors over 360°, without TVM. (b), 60 detectors over 180°, without TVM. (c), 30 detectors over 90°, without TVM. (d), 120 detectors over 360°, with TVM. (e), 60 detectors over 180°, with TVM. (f), 30 detectors over 90°, with TVM.

distributed along the surface of the circular background region. Again, strong artifacts and distortions exist in the images recovered with the method without the TVM when the data collected is angle-limited (Figs. 4b,c), while considerably improved images are reconstructed using the TVM enhanced algorithm (Figs. 4e,f).

#151589 - $15.00 USD Received 22 Jul 2011; revised 19 Aug 2011; accepted 19 Aug 2011; published 19 Aug 2011

In order to evaluate quantitatively the reconstruction quality using the method with and without TVM enhancement, we use the following universal quality index (UQI) [20]:

$$UQI\left\{\mathbf{f}^1,\mathbf{f}^0\right\}=\frac{2Cov\left\{\mathbf{f}^1,\mathbf{f}^0\right\}}{\left(\sigma^1\right)^2+\left(\sigma^0\right)^2}\frac{2\overline{f}^1\overline{f}^0}{\left(\overline{f}^1\right)^2+\left(\overline{f}^0\right)^2}. \tag{7}$$

Here the image f can be interpreted as vectors of size N: $\mathbf{f}=\left(f_1, f_2,\cdots f_N\right)^T$, where N denotes the number of image data acquired from the FEM based algorithm. $\overline{f}^j$ is the image means, σ^j is the variances, and $Cov\left\{\mathbf{f}^1,\mathbf{f}^0\right\}$ is the covariances over the whole image domain, where j = 0 and 1. UQI measures the image similarity between the reconstructed ($\mathbf{f}^1$) and reference ($\mathbf{f}^0$) images, and its value ranges between 0 and 1. The value of the UQI is closer to 1 when the reconstructed image is more similar to the reference image.

We calculated the UQIs for the three cases presented above, and the results are given in Fig. 5 where Figs. 5a and 5b show the results from the few-detector data based on the method without and with the TVM, respectively, while Fig. 5c presents the results from the limited-angle data for the first case based on the two methods. Here the image data recovered by 120 detectors was regarded as the reference one. The computed UQIs shown in Fig. 5 confirm the observation that the TVM enhanced PAT algorithm provides significantly better image quality compared to the conventional method without the TVM.

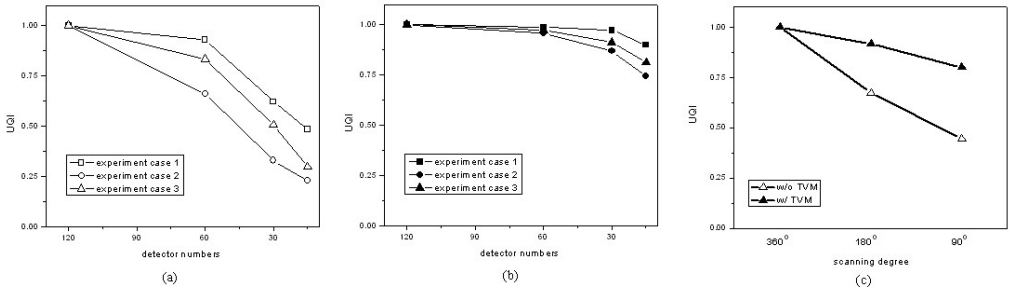

Fig. 5. UQIs calculated from the recovered images for the three cases based on few-detector data without TVM (a) and with TVM (b), and for case 1 based on limited angle data with and without TVM.

4. Conclusions

In this work, we have implemented and evaluated an unconstrained, total-variation-minimization method for time-domain FEM based PAT. This study has confirmed that in the situation that the data is collected from few measurements or over an aperture that does not enclose the object, the developed TVM based PAT algorithm provides considerably improved image reconstruction compared to the conventional methods. The application of this TVM enhanced reconstruction algorithm will significantly reduce the number of ultrasound transducers and scanning time needed for high quality photoacoustic image reconstruction.

Acknowledgment

This research was supported in part by a grant from the Department of Defense Congressionally Directed Medical Program.

#151589 - $15.00 USD Received 22 Jul 2011; revised 19 Aug 2011; accepted 19 Aug 2011; published 19 Aug 2011

Biomedical Optics EXPRESS

Photoacoustic tomography system for noninvasive real-time three-dimensional imaging of epilepsy

Bo Wang,[1] Liangzhong Xiang,[1] Max S. Jiang,[1] Jianjun Yang,[1] Qizhi Zhang,[1] Paul R. Carney,[1,2,3,4,5] and Huabei Jiang[1,*]

[1]*J. Crayton Pruitt Family Department of Biomedical Engineering, University of Florida, Gainesville, FL 32611, USA*
[2]*Department of Pediatrics, University of Florida, Gainesville, FL 32611, USA*
[3]*Neurology and Neuroscience, University of Florida, Gainesville, FL 32611, USA*
[4]*Wilder Center of Excellence for Epilepsy Research, University of Florida, Gainesville, FL 32611, USA*
[5]*McKnight Brain Institute, University of Florida, Gainesville, FL 32611, USA*
**hjiang@bme.ufl.edu*

Abstract: A real-time three-dimensional (3D) photoacoustic imaging system was developed for epilepsy imaging in small animals. The system is based on a spherical array containing 192 transducers with a 5 MHz central frequency. The signals from the 192 transducers are amplified by 16 homemade preamplifier boards with 26 dB and multiplexed into a 64 channel data acquisition system. It can record a complete set of 3D data at a frame rate of 3.3 f/s, and the spatial resolution is about 0.2 mm. Phantom experiments were conducted to demonstrate the high imaging quality and real time imaging ability of the system. Finally, we tested the system on an acute epilepsy rat model, and the induced seizure focus was successfully detected using this system.

OCIS codes: (110.5120) Photoacoustic imaging; (170.6920) Time-resolved imaging.

References and links

1. R. A. Kruger, R. B. Lam, D. R. Reinecke, S. P. Del Rio, and R. P. Doyle, "Photoacoustic angiography of the breast," Med. Phys. **37**(11), 6096–6100 (2010).
2. A. A. Karabutov, E. Savateeva, and A. Oraevsky, "Imaging of layered structures in biological tissues with opto-acoustic front surface transducer," Proc. SPIE **3601**, 284–295 (1999).
3. J. Xiao, L. Yao, Y. Sun, E. S. Sobel, J. He, and H. Jiang, "Quantitative two-dimensional photoacoustic tomography of osteoarthritis in the finger joints," Opt. Express **18**(14), 14359–14365 (2010).
4. X. Wang, Y. Pang, G. Ku, G. Stoica, and L. V. Wang, "Three-dimensional laser-induced photoacoustic tomography of mouse brain with the skin and skull intact," Opt. Lett. **28**(19), 1739–1741 (2003).
5. Q. Zhang, Z. Liu, P. R. Carney, Z. Yuan, H. Chen, S. N. Roper, and H. Jiang, "Non-invasive imaging of epileptic seizures in vivo using photoacoustic tomography," Phys. Med. Biol. **53**(7), 1921–1931 (2008).
6. J. Gamelin, A. Maurudis, A. Aguirre, F. Huang, P. Guo, L. V. Wang, and Q. Zhu, "A real-time photoacoustic tomography system for small animals," Opt. Express **17**(13), 10489–10498 (2009).
7. D. W. Yang, D. Xing, S. H. Yang, and L. Z. Xiang, "Fast full-view photoacoustic imaging by combined scanning with a linear transducer array," Opt. Express **15**(23), 15566–15575 (2007).
8. S. Manohar, A. Kharine, J. C. G. van Hespen, W. Steenbergen, and T. G. van Leeuwen, "Photoacoustic mammography laboratory prototype: imaging of breast tissue phantoms," J. Biomed. Opt. **9**(6), 1172–1181 (2004).
9. T. N. Erpelding, Y. Wang, L. Jankovic, Z. Guo, J. Robert, G. David, C. Kim, and L. V. Wang, "Three-dimensional photoacoustic imaging with a clinical two-dimensional matrix ultrasound transducer," Proc. SPIE **7899**, 78990A, 78990A-6 (2011).
10. M. B. Roumeliotis, I. Kosik, and J. J. L. Carson, "3D photoacoustic imaging using staring, sparse array with 60 transducers," Proc. SPIE **8223**, 82233F, 82233F-6 (2012).
11. C. G. A. Hoelen and F. F. M. de Mul, "Image reconstruction for photoacoustic scanning of tissue structures," Appl. Opt. **39**(31), 5872–5883 (2000).
12. L. Yao and H. Jiang, "Photoacoustic image reconstruction from few-detector and limited-angle data," Biomed. Opt. Express **2**(9), 2649–2654 (2011).
13. L. Yao and H. Jiang, "Enhancing finite element-based photoacoustic tomography using total variation minimization," Appl. Opt. **50**(25), 5031–5041 (2011).

#163569 - $15.00 USD Received 27 Feb 2012; revised 19 Apr 2012; accepted 15 May 2012; published 17 May 2012

1. Introduction

Photoacoustic tomography (PAT) is a hybrid method that is capable of imaging optical absorption of tissue through the detection of ultrasound waves generated by a short laser pulse due to transient thermoelastic expansion. It has an imaging resolution that is superior to pure optical imaging at centimeter scale depths. To date PAT has been applied to the detection of breast cancer, skin cancer and osteoarthritis in humans [1–3], and functional brain imaging in small animals [4,5].

For small animal brain imaging, most prior PAT studies were mostly based on a single-transducer scanning system or a circular or linear array of transducers for only 2D imaging [5–7], and the scanning in z direction is needed for 3D imaging purpose, which leads to a non-optimal elevational resolution in the z direction. 2D planar array of transducers has recently been employed for 3D PAT imaging [8,9]. However, due to the limited aperture of 2D planar array transducers, features with high aspect ratio or with orientations oblique to the transducer surface suffer from distortion, and the azimuthal resolution is reduced. Thus, 2D planar array of transducers is not suitable for small animal brain imaging.

Compared to a 2D planar array, a spherical array can offer more complete angular views of the object, providing both high resolution and accurate feature definition regardless of shape or location of the object. The use of sparse spherical arrays for 3D PAT imaging has been recently reported [1,10], but due to the insufficient number of transducers used, these arrays were not designed for small animal brain imaging. The goal of this work is to present a sparse spherical array based PAT system that is specifically designed for real time 3D imaging of small animal brains. The work is a natural extension/improvement of our previous work which reported for the first time 2D PAT imaging of epileptic focus in small animals [5]. The current PAT system is based on a 2D spherical array of 196 transducers coupled with parallel data acquisition, offering a temporal resolution of 0.33 s for data acquisition. We demonstrate this system using static/dynamic phantom and *in vivo* animal experiments. To the best of our knowledge, this is the first work reporting 3D PAT imaging of epileptic focus in small animals.

2. System descriptions

Figure 1 depicts the block diagram of our real-time 3D PAT system. A Ti:sapphire laser optically pumped with a Q-switched Nd:YAG laser sent 8–12 ns pulses at 10 Hz with a wavelength tunable from 690 to 1015 nm. The beam was delivered with an optical fiber

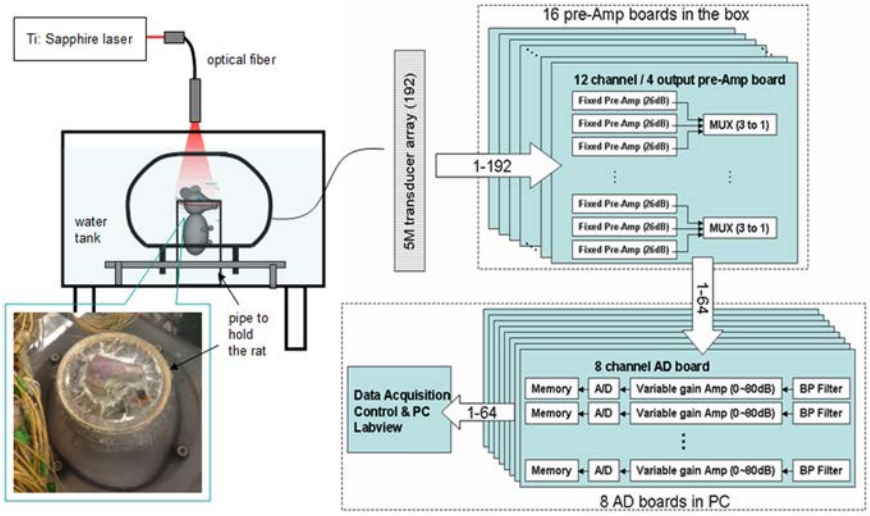

Fig. 1. Block diagram of our real-time 3D PAT system. The inset is a photograph of the close-up view of the chamber holding the rat head.

#163569 - $15.00 USD Received 27 Feb 2012; revised 19 Apr 2012; accepted 15 May 2012; published 17 May 2012

through an opening on the top of the transducer array and produced an approximately uniform illumination in a 2cm-diameter area onto the sample.

The transducer array consisted of 192 transducers placed along a custom fabricated white ABS spherical interface containing 610 through holes with counter bores, as shown in Fig. 2(a). More holes were drilled so that the selection of the transducer positions on the ball can be flexible. The interface has an outer diameter of 160 mm and an inner diameter of 140 mm, and the diameter of the holes in the ball is 5.7 mm, which fitted well with the transducer (5.5 mm outer diameter). Each transducer (Custom designed from Blatek, Inc.) has a central frequency of 5 MHz with a reception bandwidth of greater than 80%. The active area of the transducer is 3 mm in diameter and the angular acceptance is about 15 degree. The transducers were glued onto the interface with epoxy which can be removed to allow the position change of the transducers.

There were 16 preamplifier boards separately sealed in 4 metal boxes, and each board had 12 input channels, 4 output channels, and 2 digital signal control inputs. Within each board, 12 dedicated operational amplifier modules (AD8099) individually amplify the input signals with a fixed gain of 26 dB, and then the amplified signals were multiplexed into the 4 output channels by 4 multiplexer chips (MAX 4051), which were controlled by a USB IO digital module (USB-1024LS, Measurement Computing) through the 2 digital inputs.

The 64-channel parallel data acquisition system consisted of eight 8-channel PCI cards (PCIAD850, US Ultratek) in an industrial computer. For each channel, 3000 sampling points were collected at 50 MHz sampling rate in 10 bits, and stored in a 32k on board memory before they were transferred to the host machine. Amplifiers with a programmable gain of 0 to 80 dB along with a 16 MHz low band pass filter were built into the data acquisition system. A Labview program controlled the data acquisition, and the acquired data was stored on hard disk for further image processing. Images were reconstructed with a delay-and-sum algorithm [11]. For 3D image display, the reconstructed results were normalized to 0~255 after setting the negative values to be zero. Then 3D images were rendered with Amira (from Visage Imaging, Inc.) with different thresholds as indicated in the colorbar shown in each image.

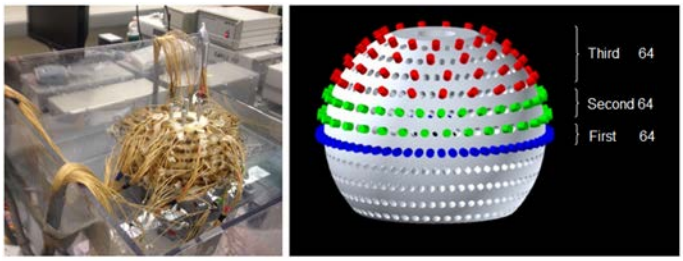

Fig. 2. The spherical transducer array. (a) Photograph of the transducer array. (b) 3D schematic of the transducer distribution on the interface.

The system allows the selection of transducer positions on the spherical interface. The total 610 holes formed 11 evenly spaced layers along the vertical direction of the ball, and the 192 transducer positions were indicated with three different colors in Fig. 2b. Three different colors were used to indicate the 3 to 1 multiplexing from the 192 transducers to the 64-channel data acquisition. This system can also be used as a real-time 2D system operating at 10 f/s using the 64 transducers arranged in the vertical center layer (blue). For *in vivo* experiments, the rat head was elevated to the center of the spherical interface through a chamber fixed at the tank bottom, whose top was about 15 mm beneath the interface center, and a transparent plastic wrap was used to cover the chamber top. For phantom experiments, a homemade silicone holder was used to hold the phantom.

#163569 - $15.00 USD Received 27 Feb 2012; revised 19 Apr 2012; accepted 15 May 2012; published 17 May 2012

3. Phantom experiments

Three different types of phantoms were used: One containing a point object for system calibration, one phantom containing three hairs tilted along different orientations for static imaging, and one phantom with ink flowing through a thin tube embedded in a phantom for real-time 3D imaging.

The point object used for calibration was a small spherical graphite particle (0.1 mm in diameter) located at the center of the spherical array and ensured an isotropic acoustic emission profile for all directions. We measured and compensated the delay of time for all the 192 channels in the radical direction, and reconstructed this point object after calibration. The hairs-containing phantom was used to demonstrate the high imaging quality of our system. Finally, we imaged an embedded tube filled with flowing ink to show the real-time imaging ability of our system. The tube had a 0.3 mm inner diameter and was horizontally placed in a phantom. No averaging of signals was performed for the phantom experiments except for the point object experiment where 10 times averaging was applied.

3.1. System characterization

We calibrated the system by recording the emission profiles from the spherical graphite particle for all the 192 channels, and then measured and compensated the time delay of each channel. We then evaluated the system resolution by reconstructing the image of the point object.

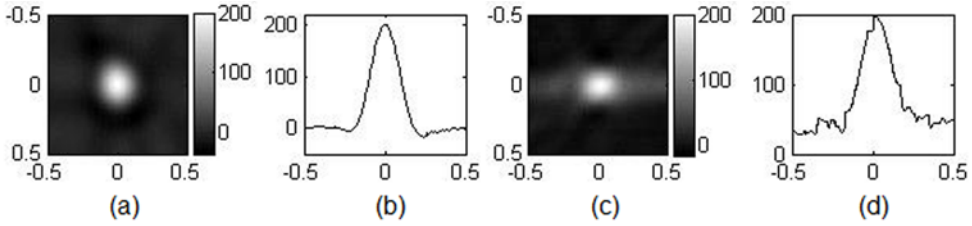

Fig. 3. (a) and (c): x-y and z-x cross section images through the center plan of the point object. (b) and (d): the profile extracted in x and z directions from (a) and (c), respectively. Units are in mm.

Figures 3a and 3c present the reconstructed x-y and z-x cross-section images of the point object located at the array center. The quality of these images is determined by both the distribution and the characteristics of the transducers. The profiles of the two reconstructed images were also extracted in x and z directions, as shown in Figs. 3b and 3d, respectively. The full width at half maximum (FWHM) of the profiles was measured to be 0.19 mm (x direction) for Fig. 3b, and 0.27 mm (z direction) for Fig. 3d, compared to the theoretical value of 0.16 mm for the 5 MHz central frequency transducer with an estimated cut off frequency of 7 MHz. It is noted that the profile in Fig. 3d is noisier than that in Fig. 3b. This along with a larger FWHM from Fig. 3d was due to the asymmetric distribution of the transducers. For targets located away from the center of the array, the radial resolution will stay nearly the same as that for a centrally located target, while the lateral resolution will be linearly reduced with increased distance away from the array center. In our system, the lateral resolution will be reduced by 0.1 mm when the target is located 5 mm off the array center.

3.2. Static phantom experiments

Figure 4a is the photograph of the phantom containing three hairs tilted along different orientations, and Figs. 4b and 4c show the reconstructed 3D images from two different views. The reconstructed volume is 10 x 10 x 10 mm with a 0.1 mm voxel size. The spatial distribution and tails for all the three hairs were clearly revealed. This result indicates that our system is capable of three-dimensionally imaging small objects of different spatial distribution and orientation in high quality.

#163569 - $15.00 USD Received 27 Feb 2012; revised 19 Apr 2012; accepted 15 May 2012; published 17 May 2012

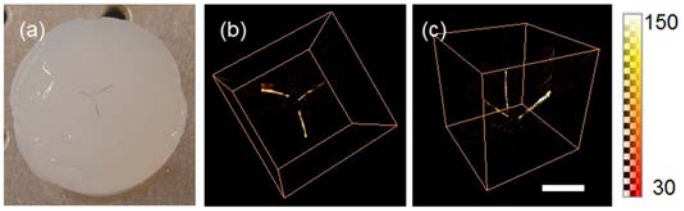

Fig. 4. (a): photograph of the phantom containing three tiled hairs; (b)-(c): reconstructed 3D images of the three hairs in two different views. Scale bar represents 5 mm.

3.3. Dynamic phantom experiments

The reconstructed 3D images of ink flowing through a thin tube are shown in Fig. 5. The image domain is 15 x 5 x 10 mm with a 0.1 mm voxel size. Figure 5a is the photograph of the phantom containing a tube filled with ink, and Figs. 5b–5j are the reconstructed 3D images at different time points. The time interval between two consecutive images was 0.3 s. These 3D images clearly tracked the flow through the tube over the course of 2.4 seconds with high spatial and temporal resolution, and the flowing speed of the ink was measured to be 6 ± 0.9 mm/s from the reconstructed results with a time interval of 0.3 s.

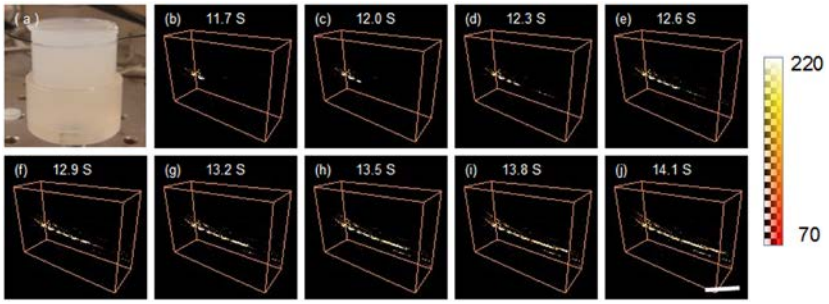

Fig. 5. Reconstructed 3D images of ink flowing through a 0.3 mm-tube embedded in a background phantom. (a): photograph of the phantom containing the tube. (b)-(j): reconstructed 3D images at different time points. The time interval is 0.3 s. Scale bar represents 5 mm.

4. Rat epilepsy experiment

Epilepsy is a serious brain disorder involving intensive hemodynamic changes, which provides high endogenous contrast for PAT imaging due to the strong absorption of blood at visible and NIR wavelengths. Compared with current existing neuron-imaging methods (such as MRI, CT, PET, and SPECT), PAT provides not only high ultrasound resolution and high optical contrast, but also unprecedented advantage of high temporal resolution over these methods, which is critical for capturing seizure dynamics.

2D PAT of seizure focus on an acute seizure rat model was demonstrated for the first time by our lab [5], but the observation of hemodynamic changes during seizure onset was hindered by the long time scanning of a single transducer. Here we test our real-time 3D system using the same animal model to show the hemodynamic changes and reveal the 3D structures in the rat brain.

Two small rats (~40g) were imaged with intact skull and skin but hairs on the head were removed. The rats were anaesthetized and mounted on the homemade plastic chamber/holder. Focal seizure was induced by microinjection of 10 μl of 1.9 mM bicuculline methiodide (BMI) into the neocortex of one rat, while saline solution was injected into the brain of another rat as control. In each experiment, the rat was elevated to the transducer array center and kept alive under the water tank through the whole experiment. The incident energy of the 730 nm light was maintained at 8mJ/cm^2 below the safety standard. Seizure process was recorded for 50 minutes, and the measurement from the control rat was recorded for 3 s. All

#163569 - $15.00 USD Received 27 Feb 2012; revised 19 Apr 2012; accepted 15 May 2012; published 17 May 2012

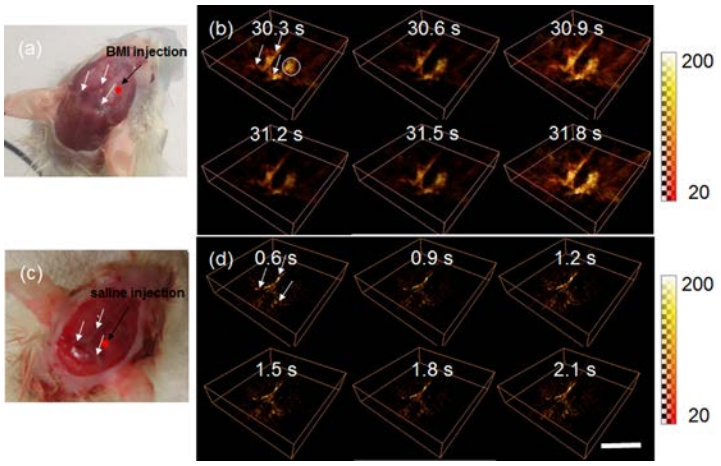

Fig. 6. (a) and (c): photograph of the rat with BMI injection and the control rat after scalp removed. (b) and (d): 3D PAT images at 6 time points for (a) and (c) respectively. The three main blood vessels are indicated by the white arrows, and the seizure focus is indicated by the circle in (b). The time interval between two successive images is 0.3 s. Scale bar represents 10 mm.

animal procedures were performed in accordance with the approved University of Florida IACUC protocols.

Figure 6b presents the 3D images for the rat with BMI injection during the seizure onset at 6 time points, compared with that for the control rat in Fig. 6b. The corresponding photographs of the two rats with scalp removed right after the experiments are shown in Figs. 6a and 6c, respectively. The reconstructed domain for the images shown in both Figs. 6b and 6d is 20 x 20 x 4.5 mm, with a 0.1 mm pixel size. The three main blood vessels on the rat brain are clearly revealed for both cases, as indicated by the white arrows, and for the rat with BMI injection a seizure focus can be clearly seen right at the BMI injection position (the white circle in Fig. 6b), where strong absorption is observed during seizure onset. The rapid changes of the absorption both in the main blood vessel and in the seizure focus were observed from Fig. 6b, while no such changes were noted for the control rat (Fig. 6c). The seizure focus had a diameter of ~3 mm, which is consistent with the results published before [5]. This experiment demonstrates that our system can be used to investigate the hemodynamic changes in small animal brain both spatially and temporally during seizure onset, although the complex microvasculature cannot be resolved due to the limited number of transducers and the simple backprojection reconstruction method used here. The microvasculature can be revealed if sophisticated reconstruction methods such as the finite element based algorithms coupled with the total variation minimization scheme are used [12,13].

5 Conclusions

We have presented a real-time photoacoustic system for three-dimensionally imaging focal cortical seizures in a rat. The system is based on a spherical array containing 192 discrete transducers. With the 64-channel data acquisition system coupled with 3:1 multiplexing, it can achieve a frame rate of 3.3 f/s with a spatial resolution of 0.2 mm. The 3D imaging performance of the system was demonstrated by both static and dynamic phantom experiments. We have also tested our system using an acute epilepsy rat model and obtained 3D images showing the hemodynamic changes during seizure onset.

Acknowledgments

This research was supported in part by a grant from the U.S. Department of Defense Congressionally Directed Medical Program, the B.J. and Eve Wilder endowment fund, and the Children's Miracle Network.

#163569 - $15.00 USD Received 27 Feb 2012; revised 19 Apr 2012; accepted 15 May 2012; published 17 May 2012

A calibration-free, one-step method for quantitative photoacoustic tomography

Zhen Yuan[a] and Huabei Jiang[b]
Department of Biomedical Engineering, University of Florida, Gainesville, Florida 32611

(Received 3 September 2012; revised 25 September 2012; accepted for publication 27 September 2012; published 25 October 2012)

Purpose: Recently reported quantitative photoacoustic tomography (PAT) has significantly expanded the utilities of PAT because it allows for recovery of tissue optical absorption coefficient which directly correlates with tissue physiological information. However, the recovery of optical absorption coefficient by the existing quantitative PAT approaches strongly depends on the accuracy of absorbed energy density distribution, and on the knowledge of accurate strength and distribution of incident light source. The purpose of this study is to develop a new algorithm for the reconstruction of optical absorption coefficient that does not depend on these initial parameters.
Methods: Here the authors propose a novel one-step reconstruction approach that can directly recover optical absorption coefficient from photoacoustic measurements along boundary domain. The authors validate the method using simulation and phantom experiments.
Results: The authors have demonstrated experimental evidence that it is possible to directly recover optical absorption coefficient maps using boundary photoacoustic measurements coupled with the photon diffusion equation in just one step. The authors found that the method described is able to quantitatively reconstruct absorbing objects with different sizes and optical contrast levels.
Conclusions: Compared to the authors' previous two-step methods, the reconstruction results obtained here show that the one-step scheme can significantly improve the accuracy of absorption coefficient recovery. © *2012 American Association of Physicists in Medicine*. [http://dx.doi.org/10.1118/1.4760981]

Key words: photoacoustic tomography, image reconstruction methods, quantitative optical imaging

Biomedical photoacoustic tomography (PAT), as a future imaging modality, can visualize the internal structure and function of soft tissues in multiscale (from millimeters to centimeters) with high spatial resolution and excellent optical contrast.[1–3] While conventional PAT can image tissues with high spatial resolution, it recovers only the distribution of absorbed light energy density that is the product of tissue optical absorption coefficient and local optical fluence. Recently reported quantitative PAT (qPAT) (Refs. 4–14) has significantly expanded the utilities of PAT as it allows for recovery of tissue absorption coefficient which directly correlates with tissue physiological information. All these methods for qPAT require a model-based reconstruction algorithm or model-free method to first capture the map of absorbed energy density or initial pressure. Then under various assumptions, the absorption coefficient is deduced from the obtained absorbed energy density/initial pressure through the photon diffusion equation or a measurement technique that can provide the distribution of exciting fluence.

However, there are several fundamental limitations associated with the existing qPAT techniques. First, one has to know the exact boundary reflection coefficients as well as the exact strength and distribution of a specified incident light source associated with the photon diffusion/transport model. It requires careful experimental calibration procedures in order to obtain these initial parameters. Second, the recovered optical absorption coefficient also strongly depends on the accuracy of the distribution of absorbed energy density. Generally, it is a challenging task to obtain an exact distribution of absorbed energy density due to several reasons: the limited bandwidth of ultrasound transducers for ultrawideband photoacoustic frequency response, dependency on the orientation, size, and shape of the targets with respect to the ultrasound receiving aperture, and effect of the optical scattering. Finally, an optical measurement method for measuring the optical fluence will increase the complexity and cost of hardware systems.[12]

To overcome the limitations mentioned above, here we propose a novel one-step reconstruction approach that can directly recover optical absorption coefficient from photoacoustic measurements along boundary domain. We validate the method using simulations as well as phantom experiments.

The photoacoustic wave equation in frequency domain for an acoustically homogeneous medium is written as (note that the method described here can be easily extended to time domain or acoustically heterogeneous cases),

$$\nabla^2 p(r,\omega) + k_0^2 p(r,\omega) = ik_0 \frac{c_0 \beta \mu_a \Phi}{C_p} \text{ or}$$
$$\nabla^2 p(r,\omega) + k_0^2 p(r,\omega) = ik_0 \frac{c_0 \beta E}{C_p} \quad (1)$$

where p is the pressure wave; $k_0 = \omega/c_0$ is the wave number described by the angular frequency, ω and the speed of acoustic wave in the medium, c_0; β is the thermal expansion coefficient; C_p is the specific heat; E is the absorbed light energy density, which is the product of absorption coefficient μ_a and optical fluence Φ ($E = \mu_a\Phi$). Based on the finite element solution to Eq. (1),[9] we use Marquardt–Tikhonov regularization based Newton method to directly recover/update absorption coefficient from an initial guess of $\mu_{a,0}$ by minimizing an object function composed of a sum of the squared difference between computed and measured acoustic pressure around the boundary areas given by

$$\text{Min: } F = \sum_{j=1}^{L}\sum_{i=1}^{M}\left(p_i^o(j) - p_i^c(j)\right)^2. \tag{2}$$

As a consequence, for each of the L frequencies, the complex matrix equation for the forward problem in Eq. (1) is stated as

$$\boldsymbol{A}_{N\times N}\boldsymbol{P}_N = \boldsymbol{B}_N. \tag{3}$$

And the following matrix equation capable of inverse solution of μ_a, is obtained for the inverse calculation:[9]

$$(\Im^T\Im + \lambda\boldsymbol{I})\Delta\boldsymbol{\chi} = \Im^T(\boldsymbol{p}^o - \boldsymbol{p}^c), \quad \boldsymbol{\mu_a} = \boldsymbol{\mu}_{a,0} + \zeta\Delta\boldsymbol{\chi} \tag{4}$$

where $\boldsymbol{p}^o = \sum_{j=1}^{L}(p_1^o(j), p_2^o(j), \ldots, p_M^o(j))^T$ and $\boldsymbol{p}^c = \sum_{j=1}^{L}(p_1^c(j), p_2^c(j), \ldots, p_M^c(j))^T$ in which complex $p_i^o(j)$ and $p_i^c(j)$ are observed and computed normalized acoustic measurements for $i = 1, 2, \ldots, M$ boundary locations with frequency j,[9] and N is the nodal number of the finite element mesh in the entire problem domain; $\Delta\boldsymbol{\chi}$ (dimension: N) is the update vector for μ_a; $\Im$ (dimension: $(L \times 2M) \times N$) is the Jacobian matrix formed by $\partial p/\partial\mu_a$ at the boundary measurement sites; λ is a scalar; ζ is calculated from common backtracking line search[15] and $\boldsymbol{I}$ is the identity matrix. In consideration of $E = \mu_a\Phi$, the sensitivity of pressure to absorption coefficient ($\partial p/\partial\mu_a$) equals the product of the sensitivity of pressure to energy density ($\partial p/\partial E$) in full field and the sensitivity of energy density to absorption coefficient ($\partial E/\partial\mu_a$) in local field. Specifically, the elements in Jacobian matrix $\Im$ are determined by

$$\frac{\partial p_i}{\partial \mu_{a,j}} = \sum_{k=1}^{N}\left(\frac{\partial p_i}{\partial E_k}\frac{\partial E_k}{\partial \mu_{a,j}}\right) \quad (i = 1, 2, \ldots, M;\ j, k = 1, 2, \ldots, N) \tag{5}$$

in which the sensitivities of $\partial p/\partial E$ in each iteration can be calculated from Eq. (3) based on the adjoint method:[9]

$$[A]\left\{\frac{\partial p}{\partial E}\right\} = \left\{\frac{\partial B}{\partial E}\right\} - \left[\frac{\partial A}{\partial E}\right]\{P\}. \tag{6}$$

Noted here $[\partial A/\partial E] = 0$ and the derivatives $\partial E/\partial\mu_a$ in Eq. (5) are further written as

$$\frac{\partial E_k}{\partial \mu_{a,j}} = \begin{cases} \Phi_k + \mu_{a,k}(\partial\Phi_k/\partial\mu_{a,j}) & \text{if} \quad (k = j) \\ \mu_{a,k}(\partial\Phi_k/\partial\mu_{a,j}) & \text{if} \quad (k \neq j) \end{cases}. \tag{7}$$

And photon fluence Φ in Eq. (7) can be computed by the finite element solution to the following photon diffusion equation:

$$\nabla\cdot D(r)\nabla\Phi(r) - \mu_\alpha(r)\Phi(r) = -S(r) \tag{8}$$

in which $S(r)$ is the normalized light source term, $D(r)$ is the diffusion coefficient and is considered a constant here. The finite element discretized form of Eq. (8) is written as,

$$[K]_{N\times N}\{\Phi\}_N = \{b\}_N. \tag{9}$$

Based on Eq. (9), the sensitivity $\partial\Phi/\partial\mu_a$ in Eq. (7) is obtained from the following equation in the whole problem domain using adjoint method:

$$[K]\left\{\frac{\partial\Phi}{\partial\mu_a}\right\} = -\left[\frac{\partial K}{\partial\mu_a}\right]\{\Phi\}. \tag{10}$$

Thus the absorption coefficient distribution can be reconstructed through a Newton iterative solution procedure described by Eq. (3) (forward solution) and Eq. (4) (inverse solution) to minimize the objective function in Eq. (2). Equations (5)–(10) are employed to calculate the Jacobian matrix in Eq. (4), and Eqs. (2)–(4) are solved separately for each iteration. The regularization parameter is determined by combined Marquardt and Tikhonov regularization schemes.[9] We have found that when $\lambda = (\boldsymbol{p}^o - \boldsymbol{p}^c) \times \text{trace}\boldsymbol{J}^T\boldsymbol{J}$, the reconstruction algorithm generates the best results for PAT image reconstruction.

The image formation process described above is first tested using simulated data. The test geometry is shown in Fig. 1(a) where a two-dimensional circular background region (50.8 mm in diameter) contained four circular targets (5 mm in diameter each). The optical properties for the background were absorption coefficient $\mu_a = 0.01$ mm^{-1} and reduced scattering coefficient $\mu_s' = 1.0$ mm^{-1}, while the optical properties were $\mu_a = 0.2$ mm^{-1} and $\mu_s' = 1.0$ mm^{-1} for the top left and bottom right targets, and $\mu_a = 0.1$ mm^{-1} and $\mu_s' = 1.0$ mm^{-1} for the top right and bottom left targets. In the simulation, a homogeneously distributed area source was utilized to illuminate the whole imaging domain, the same as in our experiments. A total of 120 ultrasound receivers were equally distributed along the boundary of background region.

For the phantom experiments, a pulsed light from a Nd:YAG laser (wavelength: 532 nm, pulse duration: 3–6 ns; Altos, Bozeman, MT) was sent to the top surface of the cylindrical phantom via an optical subsystem and consequently generated acoustic signals.[9] A transducer (1 MHz central frequency; GE Panametrics, Waltham, MA) and the phantom were immersed in a water tank. A rotary stage rotated the transducer relative to the center of the tank. The incident optical fluence was controlled below 10 mJ/cm^2 and the incident laser beam diameter was 5 cm. The complex wavefield signal was first amplified by a preamplifier (gain: 17 dB, 5 kHz to 25 MHz; Onda, Corporation, Sunnyvale, CA), and then amplified further by a Pulser/Receiver (GE Panametrics, Waltham, MA). In the experimental tests, we embedded one or two objects with a size ranging from 0.5 to 3 mm in the 5-cm-diameter solid cylindrical phantom. The phantom materials used consisted of Intralipid as scatterer and India ink as

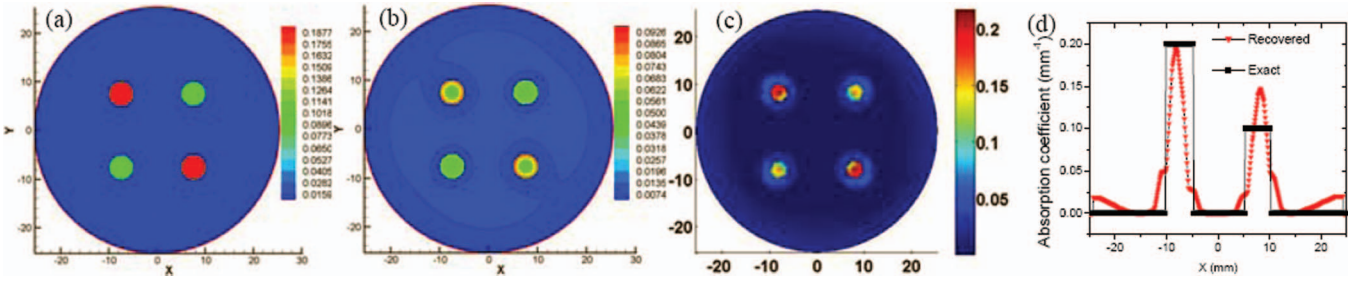

FIG. 1. Exact distribution of optical absorption coefficient μ_a (a) exact distribution of energy density (b), the recovered μ_a image using the new method (c), and recovered optical absorption profile plotted along $y = 7.5$ mm from the image shown in Fig. 1(c) (d). The axes (left and bottom) illustrate the spatial scale, in mm, whereas the gray scale (right) records the normalized absorbed energy density in arbitrary units, or μ_a in mm^{-1}.

absorber with Agar powder (1%–2%) for solidifying the Intralipid and India ink solution. We then immersed the object-bearing solid phantom into the water tank. The absorption of the background phantom was 0.01 mm^{-1}, while the absorption coefficient of the target(s) was 0.03 mm^{-1}. The reduced scattering coefficients of the background medium and target(s) were 1.0 and 3.0 mm^{-1}, respectively. As a final test, we placed human hair-containing phantom (four hairs) into the water tank to show the high resolution imaging capability of the developed scheme. The initial guess for the μ_a is 0.005 mm^{-1} for the experimental tests. It is noted that constant Gruneisen function $\Gamma = c_0^2\beta/C_p$, acoustic velocity (c_0 = 1495 m/s), and reduced scattering coefficient (1.0 mm^{-1}) were employed for all the reconstructions using both simulated and phantom data.

The results from simulated data are shown in Fig. 1, where Figs. 1(a) and 1(b) provide the exact distribution of μ_a and absorbed energy density, respectively, while Fig. 1(c) presents the reconstructed μ_a image using the one-step qPAT algorithm. We can see from Fig. 1(c) that the targets are clearly identified in terms of the target position, size, and absorption coefficient value. The target size was estimated to be 4.6 mm in diameter using the full width at half-maximum (FWHM) of the recovered μ_a profile in Fig. 1(d).

It is also observed from Fig. 1(b) that the influence of the inhomogeneous distribution of optical fluence on the energy density map is apparent, where low values of energy density appear in the center area of the four targets and results in hollow phenomena for the solid targets. However, the absorption coefficient map shown in Fig. 1(c) indicates that the new method has the capability to completely remove effect of the heterogeneous distribution of local fluence.

The results from the first experiment are shown in Fig. 2, where Figs. 2(a) and 2(b) show the recovered μ_a maps using the previous[9] and present qPAT methods, respectively. By estimating the FWHM of the specific profiles for the images shown in Fig. 2(b), we found the recovered object sizes were 1.9 and 3.1 mm, which are in good agreement with the actual object sizes of 2.0 and 3.0 mm. Figure 3 plots the reconstructed absorption coefficient images for experimental test 2 using both the previous[9] and present qPAT schemes. The recovered target size using the present and previous schemes, as shown in Fig. 3(c), was found to be 0.55 and 0.8 mm, respectively, compared to the actual target size of 0.5 mm. Obviously the previous method overestimated the target size in most cases. We also found from Figs. 2 and 3 that the current qPAT method is able to considerably reduce the effect of local optical fluence and boundary noise. Further, it is

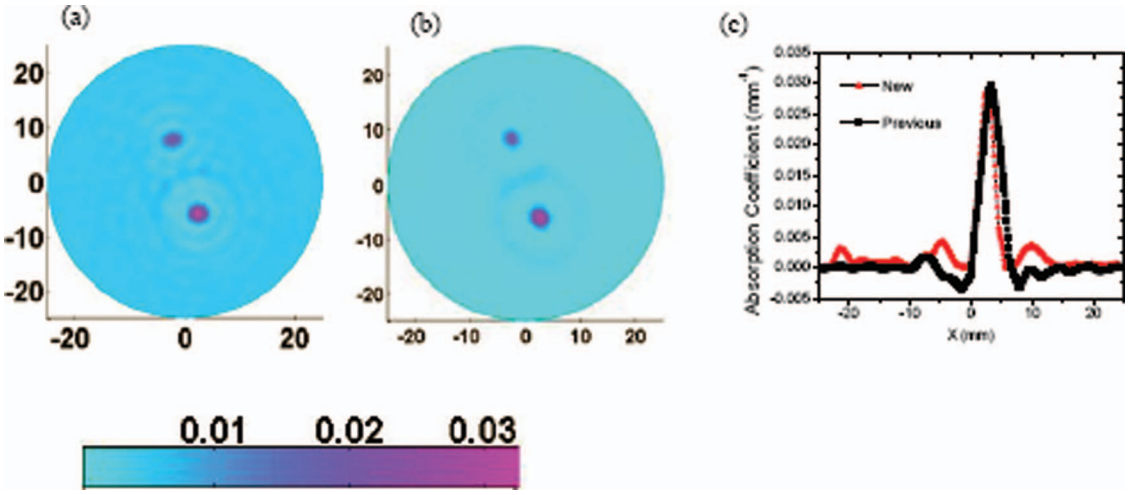

FIG. 2. Reconstructed μ_a image using the previous scheme (a), the new scheme (b), and recovered optical absorption profile plotted along $y = -7.0$ mm from the images shown in Figs. 2(a) and 2(b) (c). The axes (left and bottom) illustrate the spatial scale, in mm, whereas the gray scale (right) records μ_a in mm^{-1}.

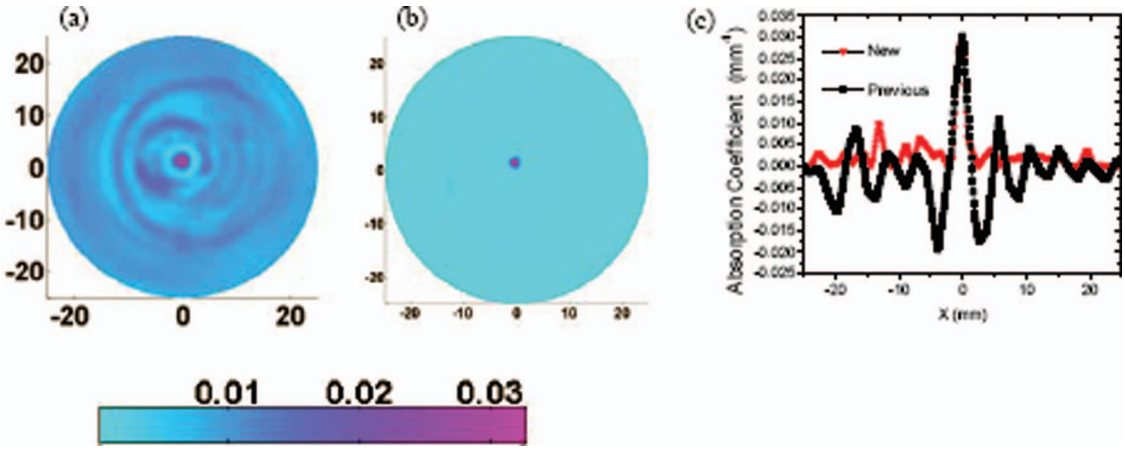

FIG. 3. Reconstructed μ_a images using (a) the previous, (b) new scheme, and (c) recovered optical absorption profile plotted along $y = 1.0$ mm from the images in (a) and (b).

observed from Fig. 4 that based on the developed scheme, the human hairs embedded in phantom are clearly identified with submillimeter resolution and quantitative absorption coefficient.

In summary, we have demonstrated experimental evidence that it is possible to directly recover the absolute μ_a image using boundary photoacoustic measurements coupled with the photon diffusion equation in just one step. The method described is able to quantitatively reconstruct absorbing objects with different sizes and optical contrast levels. In particular, it is noted that this method does not depend on any calibration procedure because it allows for the use of relative incident laser source strength and normalized boundary measurements of acoustic pressure. The source intensity and boundary condition coefficient can be optimized and localized based on the photon diffuse equation by minimizing f with the normalized acoustic measurements $\bar{p}$: $f = \sum_{i=1}^{M} ((\mu_a \Phi)_i - \bar{p}_i)^2$. As such, the reconstruction of absorption coefficient with the new algorithm does not depend on the absolute values of absorbed energy density and optical fluence whereas the previous methods are all dependent on these values. Additionally, we note that different transducer sensitivity may lead to a different scaling factor of the reconstructed absorption coefficient images. Routine calibrations on the transducer response had to be done in our previous study.[9] However, in the new scheme presented here, we use normalized acoustic data in arbitrary units (i.e., the largest value of pressure is 1.0) to recover the absorption coefficient, reducing the impact of transducer sensitivity significantly. It should be pointed out, however, that the choice of the initial guess of μ_a does have some effect on the recovered results. Finally, further investigation is warranted to consider optical scattering, inhomogeneous acoustic properties, inhomogeneous light illumination field, and multispectral photoacoustic measurements within the framework of this new method.

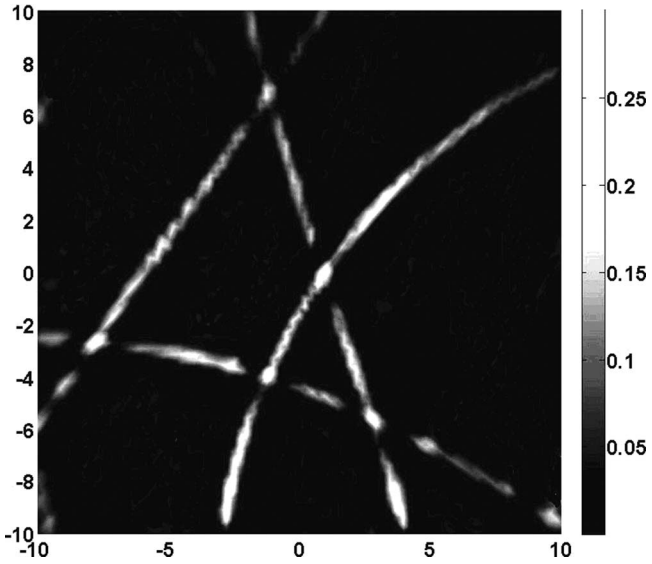

FIG. 4. The recovered μ_a image for the human hair phantom.

ACKNOWLEDGMENT

This research was supported in part by a grant from the Department of Defense Congressionally Directed Medical Program. This research was supported in part from the National Institute of Neurological Disorders and Stroke, NIH Grant No. 1R01NS069848-01.

[a]Electronic mail: zyuan11@asu.edu
[b]Electronic mail: hjiang@bme.ufl.edu

[1]L. V. Wang and H. Wu, *Biomedical Optics: Principles and Imaging* (Wiley, New York, 2007).
[2]G. Paltauf and H. Schmidt-Kloiber, "Pulsed optoacoustic characterization of layered media," J. Appl. Phys. **88**, 1624–1631 (2000).
[3]A. A. Oraevsky, S. L. Jacques, and F. K. Tittel, "Measurement of tissue optical properties by time-resolved detection of laser-induced transient stress,"Appl. Opt. **36**, 402–415 (1997).
[4]R. Zemp, "Quantitative photoacoustic tomography with multiple optical sources," Appl. Opt. **49**, 3566–3572 (2010).
[5]Y. Yuan, S. Yang, and D. Xing, "Optical-resolution photoacoustic microscopy based on two-dimensional scanning galvanometer," Appl. Phys. Lett. **100**, 023702 (2012).
[6]B. Cox, S. Arridge, K. Kostli, and P. Beard, "2D quantitative photoacoustic image reconstruction of absorption distributions in scattering medium using a simple iterative method," Appl. Opt. **45**, 1866–1875 (2006).

[7]C. Xu, P. Kumavor, A. Aguirre, and Q. Zhu, "Quantitative recovery of absorption coefficient using DOT-assisted photoacoustic tomography for breast imaging," in BsuD in OSA Biomedical Optics Topical Meeting, Miami, FL, 2010.
[8]B. Banerjee, S. Bagchi, R. M. Vasu, and D. Roy, "Quantitative photoacoustic tomography from boundary pressure measurements: Non iterative recovery of optical absorption coefficient from the reconstructed absorbed energy map," J. Opt. Soc. Am. A **25**, 2347–2356 (2008).
[9]Z. Yuan and H. Jiang, "Quantitative photoacoustic tomography: Recovery of optical absorption coefficient map of heterogeneous medium," Appl. Phys. Lett. **88**, 231101 (2006).
[10]Z. Yuan, Q, Wang, and H. Jiang, "Reconstruction of optical absorption coefficient map of heterogeneous media by photoacoustic tomography coupled diffusion equation based regularized Newton method," Opt. Express **15**, 18076–18081 (2007).
[11]B. T. Cox, J. G. Laufer, and P. C. Beard, "Quantitative photoacoustic image reconstruction using fluence dependent absorbers," Biomed. Opt. Express **1**, 201–208 (2010).
[12]L. Yin, Q. Wang, Q. Zhang, and H. Jiang, "Tomographic imaging of absolute optical absorption coefficient in turbid medium using combing photoacoustic and diffusing light measurements," Opt. Lett. **32**, 2556–2558 (2007).
[13]G. Bal and G. Uhlmann, "Inverse diffusion theory of photoacoustics," Inverse Probl. **26**, 085010 (2010).
[14]H. Gao, H. Zhao, and S. Osher, "Quantitative photoacoustic tomography," University of California Los Angeles (UCLA) Computational and Applied Mathematics Reports (UCLA, 2011), Vols. 11–28.
[15]Z. Yuan and H. B. Jiang, "An image reconstruction scheme that combines modified Newton method and efficient initial guess estimation for optical tomography of finger joints," Appl. Opt. **46**, 2757–2768 (2007).

NeuroImage 66 (2013) 240–248

Contents lists available at SciVerse ScienceDirect

NeuroImage

journal homepage: www.elsevier.com/locate/ynimg

Noninvasive real time tomographic imaging of epileptic foci and networks

Liangzhong Xiang [a], Lijun Ji [a], Tao Zhang [a], Bo Wang [a], Jianjun Yang [a], Qizhi Zhang [a], Max S. Jiang [a], Junli Zhou [b,c], Paul R. Carney [a,b,c,d], Huabei Jiang [a,*]

[a] J. Crayton Pruitt Family Department of Biomedical Engineering, University of Florida, Gainesville, FL 32611, USA
[b] Departments of Pediatrics, Neurology, and Neuroscience, University of Florida, Gainesville, FL 32611, USA
[c] Wilder Center of Excellence for Epilepsy Research, University of Florida, Gainesville, FL 32611, USA
[d] McKnight Brain Institute, University of Florida, Gainesville, FL 32611, USA

ARTICLE INFO

Article history:
Accepted 25 October 2012
Available online 2 November 2012

Keywords:
Real time photoacoustic tomography (PAT)
Noninvasive seizure dynamic imaging
Epileptic foci and networks
Pre-surgical planning

ABSTRACT

While brain imaging and electrophysiology play a central role in neuroscience research and in the evaluation of neurological disorders, a single noninvasive modality that offers both high spatial and temporal resolution is currently not available. Here we show in an acute epilepsy rat model that photoacoustic tomography (PAT) can noninvasively track seizure brain dynamics with both high spatial and temporal resolution, and at a depth that is clinically relevant. The noninvasive yet whole surface and depth capabilities of the PAT system allowed us to actually see what is happening during ictogenesis in terms of seizure onset and spread. Both seizure onset and propagation were tomographically detected at a spatial resolution of 150 μm and a temporal resolution of 300 ms, respectively. The current study lends support to the theory that seizure onset and spread involves a rich interplay between multiple cortical and subcortical brain areas during the onset and spread of epileptic seizures. Dynamical changes of vasculature during epileptiform events were also detected with high spatiotemporal resolution. Together, these findings suggest that PAT represents a powerful tool for noninvasively mapping seizure onset and propagation patterns, and the 'functional' connectivity within epileptic brain networks.

Introduction

Epilepsy is a common, chronic, neurological disorder characterized by seizures. Three percent of people will be diagnosed with epilepsy at some time in their lives (Hauser et al., 1996). Indeed, approximately 50 million people worldwide have epilepsy, and 20 to 30% of these patients are refractory to all forms of medical treatment (Hauser, 1992). In most cases, seizures are controlled, although not cured, with anticonvulsant medication. Seizure types are classified according to whether the source of the seizure is localized (partial or focal onset seizures) or distributed (generalized seizures) (Greenfield et al., 2011). Localization-related epilepsies arise from an epileptic focus. A partial seizure may spread within the brain, a process known as secondary generalization. Generalized epilepsies, in contrast, arise from many independent foci (multifocal epilepsies) or from epileptic circuits that involve the whole brain. In epilepsies of unknown localization, it remains unclear as to whether they arise from a portion of the brain or from more widespread circuits.

For those patients with medically intractable focal epilepsy, the best treatment option is resective brain surgery (Berg et al., 2007; Birbeck et al., 2002; Duncan et al., 2006). Although several factors can impact the success of epilepsy surgery, the primary reason of failure is the incomplete mapping of the local epilepsy network which results in incomplete resection of epileptogenic foci (Engel, 2004; Jeha et al., 2007). Much of the attention on epilepsy surgery has been directed at identifying single neuronal populations. This approach has, in many cases, led to failed surgical outcomes, because seizures typically involve groups of neurons interacting both locally and across several cortical and subcortical brain regions. A better understanding of the regional interactions occurring at the site of seizure onset and spread may provide important insights about the pathophysiology of seizures and aid with accurate brain mapping and resection of the epileptic focus.

In theory, removing the focus should result in a patient's seizures being cured. However, there is much evidence to suggest that the focus is more of a region of seizure onset with a number of sites that can act independently to initiate seizures (Thom et al., 2010a, b). Seizures in animal models and in people often have a multifocal or broadly synchronized onset. The best evidence for multifocality within the seizure onset zone comes from surgical experience with intracranial monitoring. The challenge of mapping the epileptic focus stems from the observation that the pathology associated with focal epilepsy is often distributed across a number of brain sites

* Corresponding author at: University of Florida College of Engineering, J. Crayton Pruitt Family Department of Biomedical Engineering, JG56 BMS Building, Gainesville, FL 32611, USA.
E-mail address: hjiang@bme.ufl.edu (H. Jiang).

1053-8119/$ – see front matter © 2012 Elsevier Inc. All rights reserved.
http://dx.doi.org/10.1016/j.neuroimage.2012.10.077

(Bertram, 2009) and that current diagnostics methods frequently fall short of identifying such sites. Animal studies indicate that the neurons involved in the epileptic circuitry have enhanced excitability throughout (Bertram et al., 1998; Fountain et al., 1998; Mangan et al., 2000). The implication of these observations is that each of the sites could act independently to initiate a seizure or, potentially, to drive another site into a seizure. Thus, in focal epilepsy, one may view a cortical region as a broad seizure onset zone, with the potential that multiple foci can act as a seizure focus for any given seizure.

Much of our understanding about focal seizure circuitry comes from electrophysiological recording methods. Although electrophysiology is currently the 'gold standard' in mapping the epileptic focus, it is often inadequate to define the boundary of the epilepsy circuitry due to spatial sampling limitations and volume conduction. What we truly desire is a brain mapping modality, which could give a high-resolution real time spatial and temporal 'read out' of the dynamics of cortical processing and seizures. It has been well established that optical contrast is highly sensitive to neuronal activity (Grinvald et al., 1988; Hill and Keynes, 1949). The high optical contrast is largely due to the changes in blood volume and blood oxygenation, both of which substantially increase during seizures, and increase in oxygenation metabolic rate results in increased demands on autoregulatory mechanisms (Folbergrová et al., 1981). Taking the advantage of the oxygenation dependence in the optical absorption spectrum of hemoglobin, optical imaging or intrinsic optical signal (IOS) methodologies have provided excellent surface maps of epileptic focus (Haglund and Hochman, 2004; Haglund et al., 1992). Although near-infrared spectroscopy (NIRS) (Steinhoff et al., 1996, Sokol et al., 2000, Watanabe et al., 2000) and blood-oxygen-level-dependent (BOLD) MRI can assess oxygen saturation with endogenous contrasts, BOLD MRI is sensitive only to HbR with low temporal resolution (Ogawa et al., 1990). In addition, the major limitation of NIRS and IOS is that each provides only surface depth information. Greater depth information can be obtained by using tomographic reconstruction methods such as diffuse optical tomography (Bluestone et al., 2001; Boas et al., 2001; Jiang et al., 1996; Oleary et al., 1995). Whereas diffuse optical tomography has low spatial resolution, laser-induced photoacoustic tomography (PAT) has both superior spatial and temporal resolution. PAT detects absorbed photons ultrasonically by employing the photoacoustic effect. It combines both high contrast and spectroscopic specificity based on the optical absorption of both oxy- and deoxy-hemoglobin with high ultrasonic spatial resolution (Kruger and Liu, 1994; Laufer et al., 2007; Xiang et al., 2007; Yuan et al., 2007). Relative to other optical imaging modalities, PAT has the advantage of mitigating both scalp and skull light scattering by a factor of ~1000. The end result is that PAT allows for high spatial resolution imaging of brain at a depth considerably beyond the soft depth limit of conventional optical imaging techniques such as confocal microscopy (Sipkins et al., 2005), two-photon microscopy (Denk et al., 1990), and optical coherence tomography (Huang et al., 1991). The strong preferential optical absorption of hemoglobin makes PA imaging to have a better imaging contrast than ultrasound (US); as it can be difficult to visualize the microvessels with pulse-echo US owing to the weak echogenicity (Mace et al., 2011).

In this study, PAT was employed to image seizures in an experimental acute bicuculline methiodide model of focal epilepsy. Bicuculline is a light-sensitive competitive antagonist of $GABA_A$ receptors that mimics focal epilepsy when applied to brain tissue. During focal application of bicuculline into the brain cortex, brains were imaged noninvasively with a novel PAT system that has three orders of magnitude higher temporal resolution and four-fold higher spatial resolution relative to our previous PAT prototype (Zhang et al., 2008). Off-line, we employed measures of brain connectivity to further identify the functional anatomy implicated in focal cortical seizures. The high spatial and temporal sampling of the novel PAT system allowed for the first time the complete mapping of an epileptiform event *in vivo*.

Methods

Animals

Male Sprague–Dawley rats (Harlan Labs, Indianapolis, IN) weighing 50–60 g on arrival were allowed one week to acclimate to the 12-h light/dark cycle and given food and water ad libitum. All procedures were approved by the University of Florida Animal Care and Use Committee and conducted in accordance with the National Institutes of Health Guide for the Care and Use of Experimental Animals.

PAT imaging

Light from a Ti: Sapphire laser tunable (690 to 950 nm) was delivered through the skull to the brain through an optical fiber (Fig. 1a). The energy of each laser pulse was detected by a photodiode for calibration. A 192 element full-ring transducer array was used to capture the photoacoustic (PA) signals generated by the laser light. The 192 channel data acquisition system consisted of preamplifiers, secondary stage amplifiers (for optimizing the signal-to-noise ratio), and a 3:1 electronic multiplexer coupled with a 64-channel analog-to-digital converter. Each ultrasonic detector had a 5-MHz central frequency and a 70% nominal bandwidth with a diameter of 6 mm (Blatek, Inc., PA, USA).

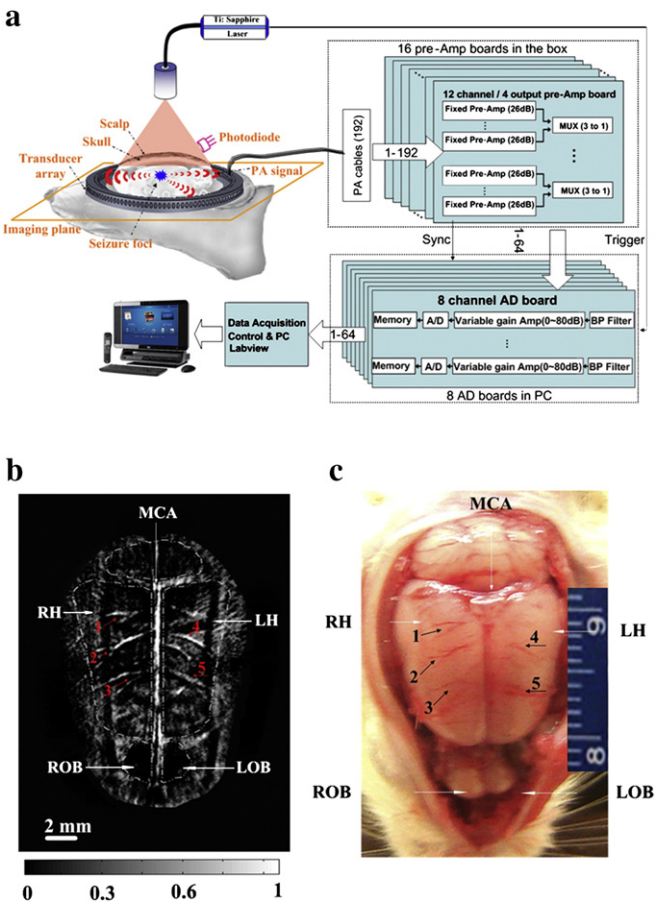

Fig. 1. Real time PAT system for seizure dynamics. (a.) Schematic of the real time PAT system. A 192-element full-ring transducer array was used to capture the PA signal during seizure onset. (b.) Noninvasive PAT imaging of a rat brain *in vivo* with the skin and skull intact. MCA, middle cerebral artery; RH, right hemispheres; LH, left hemispheres; LOB, left olfactory bulbs; ROB, Right olfactory bulbs. (c.) Open-skull photograph of the rat brain surface acquired after the PAT experiment. Numbers 1–5 indicate the corresponding blood vessels in the PAT image and rat brain photograph.

Electrode implantation surgery

Animals were anesthetized intraperitoneally with 1 g/kg of body weight dose of urethane. Two 300 μm diameter stainless steel screw electrodes were implanted within the skull for obtaining subdural multichannel cortical local field potentials data (−0.3 mm posterior, 3 mm lateral (right) of bregma, 1 mm ventral) based on coordinates from a rat brain atlas (Paxinos, 1998). One, 300 μm diameter stainless steel screw electrode (FHC, Bowdoin, ME) was implanted as a reference electrode into the midline occipital bone. Cortical local field potentials were obtained using a Tucker Davis Pentusa (Tucker Davis Technologies, Alachua, FL) neural recording system at 12 kHz, digitized with 16 bits of resolution, and band pass filtered from 0.5 to 6 kHz.

Induction of seizures

Rats (n = 10) received 10 μl of 1.9 mM bicuculline methiodide and 10 μl normal saline into the left and right parietal cortex, respectively. The infusion was performed through the previously implanted electrode sites at a rate of 0.3 μl/min. The infusion system consisted of a 100 μl gas-tight syringe (Hamilton, Reno, NV) driven by a syringe pump (Cole-Parmer, Vernon Hills, IL) connected to polyaryletheretherketone (PEEK) tubing (ID = 0.381 mm, OD = 0.794 mm, length ~ 0.5 m, Upchurch Scientific, Oak Harbor, WA). The PEEK tubing was coupled to a silica cannula (ID = 50 μm, OD = 147 μm, Polymicro Technologies, Phoenix, AZ) via a microfluidic connector. Cortical local field potentials were recorded 5 min before each injection and continued for up to 30 min thereafter.

Image analysis

A custom software utility was written and incorporated into the computer software package MATLAB (MathWorks, Massachusetts, USA) to analyze and display recorded data. This software enabled the reconstruction of the PAT images and the determination of the blood vessel diameter. Amira (version 5.3.3, TGS Template Graphics Software) was used for three-dimensional reconstruction of the seizure foci. We used the frequency domain Granger causality methodology to evaluate the dynamic interactions within the seizure circuitry and the associated brain networks (Brovelli et al., 2004; Granger, 1969; Wang et al., 2007). The time-series data were selected from 200 sets of PAT images sampled at 3 Hz within the seizure onset period, and at each time point, we chose 9 (regions of interest) ROI (R1–R9) and then the PA signal was averaged within each ROI, as shown in Fig. 5b1. Changes in photoacoustic signals were quantified as $-\Delta A/A$ in Fig. 5b3, right. The PA data shown in Figs. 3–5 were not averaged. The image color scale was determined by the photoacoustic signal intensity in arbitrary units (between 0 and 1).

Results

Noninvasive epileptic foci localization

Temporal and spatial resolutions of the PAT system were experimentally determined. PA images depicting frames from a 10-second sequence of dynamic ink flow through a 0.3 mm diameter tube was shown in Movie S1. The movie shows that the temporal resolution of this imaging system was ~0.33 s/frame. Cross-sectional PA image of a two-copper-rods phantom was used to test the spatial resolution of the PAT imaging system. The two copper rods (diameter: 0.05 mm) were embedded in a cylindrical tissue-mimicking phantom at a depth of 10 mm. The center-to-center distance between the two copper rods was approximately 2.2 mm. The spatial resolution of the imaging system calculated with Rayleigh's law was 150 μm. The spatial resolution of the PAT system was inversely related to the bandwidth of the ultrasonic transducer.

The noninvasive PAT image of the rat cortical vasculature (Fig. 1b) matched well with an anatomical atlas (Paxinos, 1998) (Fig. 1c) obtained after the PA imaging. The brain structures including the middle cerebral artery, right hemispheres, left hemispheres, left olfactory bulbs, and right olfactory bulbs are clearly shown in the PAT image. Numbers 1–5 marked in the image indicate that the micro-blood vessels with a diameter of less than 100 μm are also seen, which again correspond well with the rat brain photograph. This allowed for imaging objects of 50 μm in diameter with a spatial resolution of 150 μm (Figs. 2b, c).

Thirty minutes following the microelectrode placement, PAT imaging was performed to generate baseline tissue absorption maps, visualize micro blood vessels, and morphological cortical landmarks (Figs 3b, c). Subsequently, rats (n = 10) received 10 μl of 1.9 mM bicuculline methiodide and 10 μl normal saline into the left [−1.0AP, 2.5ML, 2.4DV] and right [−1.0AP, 2.5 ML, 0.4DV] parietal cortex, respectively, based on coordinates from a rat brain atlas (Paxinos, 1998). Immediately following the focal infusions, PAT imaging was repeated to visualize changes in the injection site tissue absorption. An increase in tissue absorption was observed in the bicuculline methiodide cortical injection site and surrounding region (Fig. 3c, left), but not in the saline injection site or surrounding region (Fig. 3c, right). PAT scanning for subcortical changes was also performed. Slices 5, 7, and 9 (Fig. 3d) are the images obtained 3, 5 and 7 mm below the scalp, respectively. Fig. 3e is the three dimensional rendering of the epileptic foci obtained from different tomographic layers (movie S2). Each image exhibited the variable patterns of seizure onset and propagation both at the cortical and subcortical regions. Seizures were confirmed by concomitant time-locked PAT/video-electroencephalography (Fig. 3a). Experiments were repeated for each animal at 2-hour intervals.

Real time monitoring of epileptic events

Epileptiform events were recorded with PAT from a focal region of interest of ~2 × 3 mm (Fig. 4a). We observed a significant optical absorption change directly associated with de-oxygenation at a wavelength of 755 nm (Fig. 4c). Furthermore, at the seizure onset at 1 min 6.267 s, the seizure focus measured 0.2053 mm^2 and increased to 0.5004 mm^2 as the electrographic seizure time-series increased in frequency and amplitude (Fig. 4b). Corresponding rate changes (0.33 s) spike and wave discharges and PA images were observed in each experimental trial. The seizure onset dynamics captured photoacoustically are best appreciated in movies displaying how the seizure was generated and varied over time (Movie S3). PAT images suggest that in addition to ictal spread from the primary focus, homotopic foci are seen in the contralateral parietal cortex (Fig. 5a1–4). The PA signal in the contralateral foci was smaller in magnitude and delayed in time compared to the signal recorded from the primary seizure foci. We also observed a region of inverted optical signal immediately surrounding the seizure onset zone (Fig. 5b2–3). We performed analysis of the optical signal at a distance of at least 2 mm (±0.01) away from the edge of the focus. Our results demonstrate that the photoacoustic signal was inversely related to the optical signal recorded from the focus (Fig. 5b3).

To evaluate the dynamic interactions within the seizure circuitry and capture the associated networks we used the frequency domain Granger causality (Brovelli et al., 2004; Granger, 1969; Wang et al., 2007). PAT time series data was selected from 200 sets of PAT images sampled at 3 Hz within the seizure onset period. At each time point we chose 9 ROIs (Fig. 5b1) and used the averaged optical absorption within each region for the network analysis. Nine sets of time series analysis were classified into 3 groups including the primary ictal onset area and corresponding 4 surrounding regions of interest including the primary or initiating seizure focus, contralateral homotopic foci, and 2 regions of interest surrounding the primary focus in the

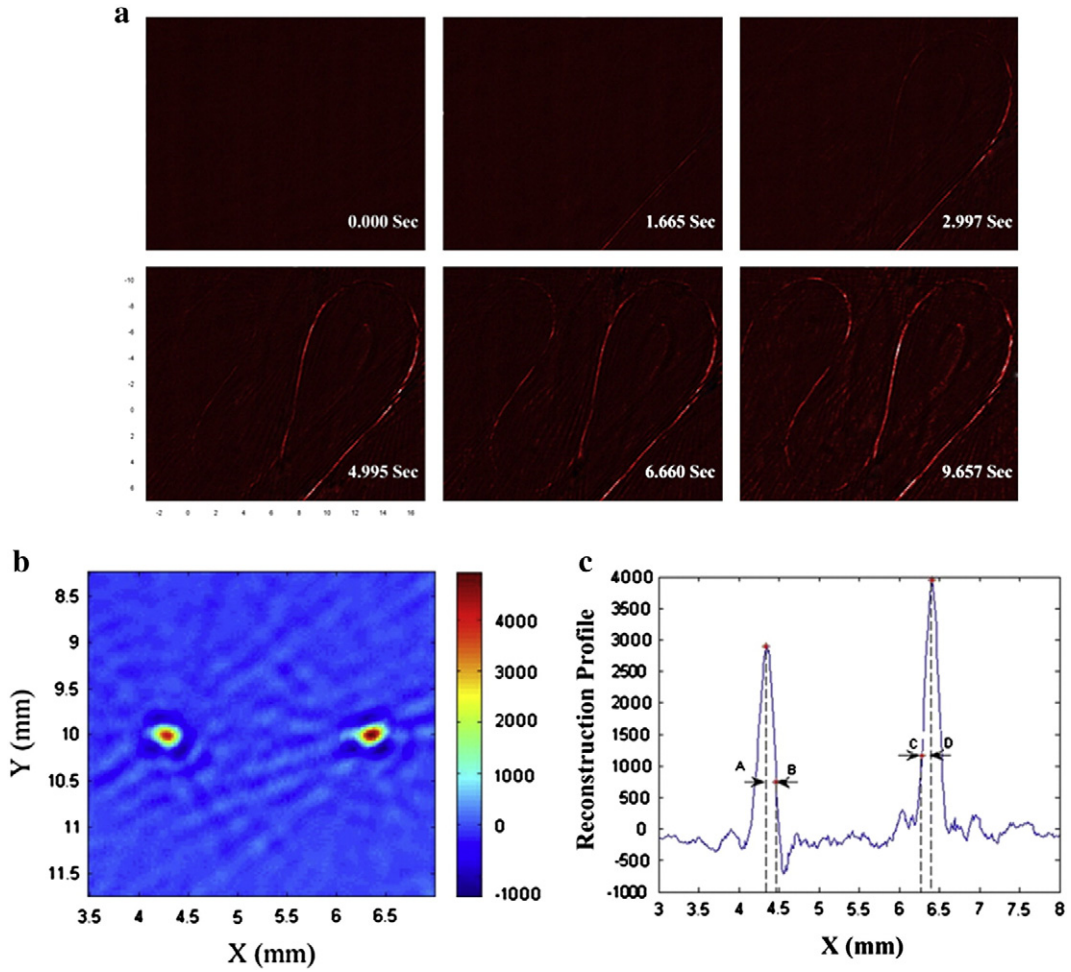

Fig. 2. Temporal and spatial resolution demonstration of the PAT system. (a.) Temporal resolution demonstration of the PAT system. Photoacoustic images depicting frames from a 10-second sequence of dynamic ink flow through a 0.3 mm diameter tube (Movie S1). The movie shows that the temporal resolution of this imaging system was ~0.33 s/frame. (b.) Cross-sectional PA image of a two-copper-rods phantom. The two copper rods (diameter: 0.05 mm) were embedded in a cylindrical tissue-mimicking phantom at a depth of 10 mm. The center-to-center distance between the two copper rods was approximately 2.2 mm. (c.) The normalized profile of the reconstructed PA image shown in (b.) along y = 10 mm. The half- and quarter-amplitude widths were obtained by measuring the distance between points AB and between CD, respectively. The spatial resolution of the imaging system calculated with Rayleigh's law was 150 μm.

contralateral cortex. The middle cerebral artery, primary seizure focus, and secondary homotopic seizure focus were also analyzed. Results from group 1 analysis demonstrate the causal influence from the primary focus to the surrounding regions of interest (Fig. 5b1). The negative zero-lag correlation (−0.68) between both the primary and secondary foci showed that neural activities within these two regions changed in opposite direction over time. Fig. 5b4 shows the Granger causality analysis for group 2 data where we see that the primary and secondary contralateral brain foci influenced each other mutually with a stronger influence of the primary focus relative to the contralateral focus. Moreover, we suggest that the primary seizure focus may influence the contralateral foci as previously suggested using optical intrinsic imaging in epilepsy (Khalilov et al., 2003) and microelectrode recordings of hippocampus local field potentials (Cadotte et al., 2010). Finally, from group 3 analyses (Fig. 5b5) we found that the primary focus strongly influenced the hemodynamic change in the middle cerebral artery, which in turn showed influence on the contralateral homotopic foci.

Dynamical changes of vasculature during interictal discharges

Fig. 6a shows image of the rat cortex vasculature through the intact scalp and skull. The red arrow indicates the microvascularity along the direction marked by the yellow dashed line, representing a cross-sectional scanning using a 50 MHz ultrasound transducer. Positive and negative acoustic peaks induced by a 25 μm blood vessel were sorted out as target signals to track the change of the vessel diameter. Typical PA signals from the targeted vessel at different times show apparent vessel vasomotion by ~40% (mean = 40%, $P < 0.03$, $N = 20$) during the interictal discharges (Fig. 6b). Local field potential recordings (Fig. 6c) showed that interictal spikes had a strong correlation with the discrete change in vessel size observed photoacoustically (Fig. 6d; error bars ± s.d. was calculated from 20 consecutive spikes).

Discussion

The main finding is that PAT imaging is a novel tool for noninvasively mapping seizure dynamics with both high spatial and temporal resolution. This study investigated the hemodynamic changes during focal seizure onset and propagation in an acute model of focal epilepsy. The experimental results suggest that the increase in local and surrounding brain tissue absorption was due to the focal bicuculline methiodide induced seizure rather than other factors such as stab cortex tissue wound injection. Epileptiform events, including interictal spikes, ictal onset and spread were identified in near real time. To the best of our knowledge, this is the first experimental evidence for millisecond temporal resolution, centimeters depth, and micron scale imaging of focal seizure onset and spread by a noninvasive technique.

Quantitative photoacoustic image reconstruction can be used to resolve the light scattering problem with the deeper penetration in

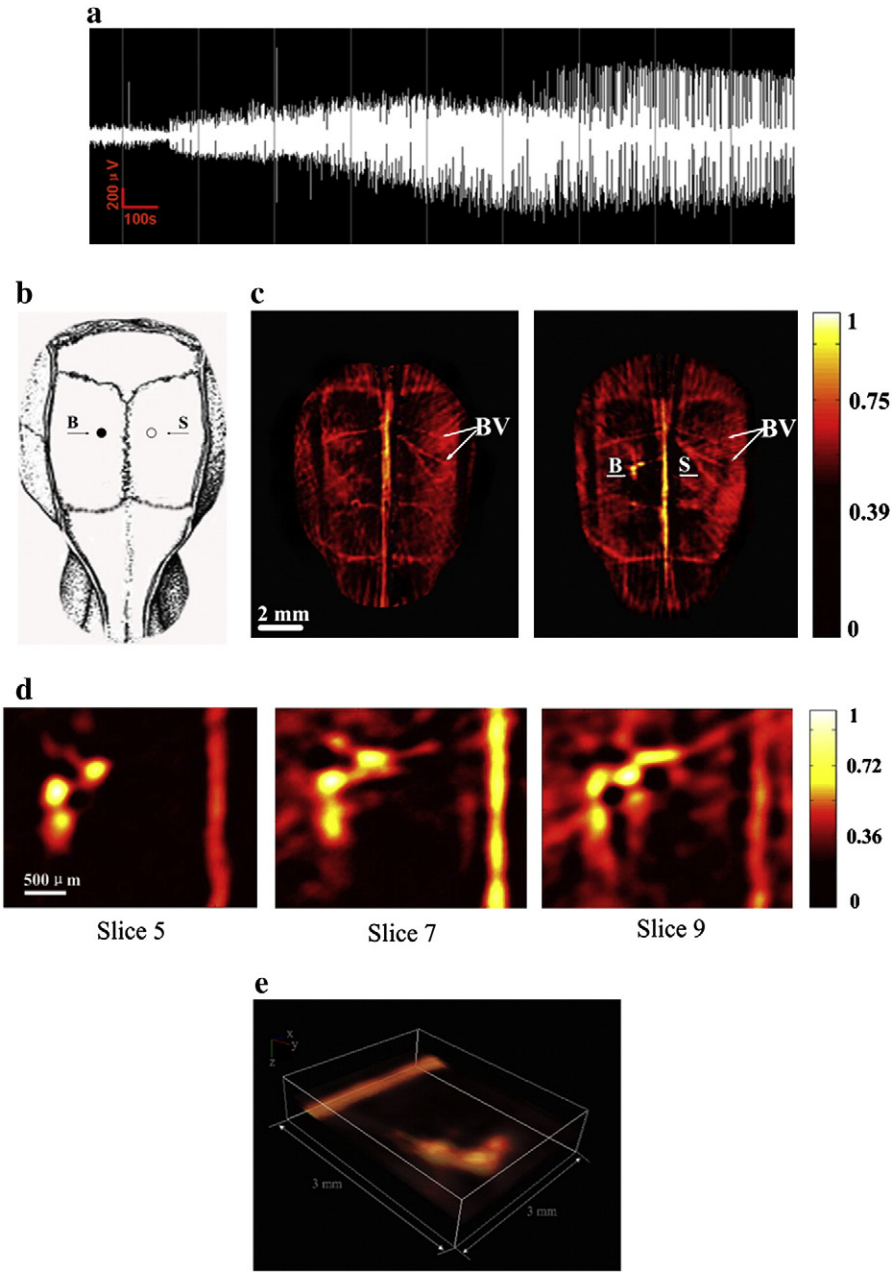

Fig. 3. Noninvasive epileptic foci localization. (a.) EEG recordings of seizure onset after BMI injection. (b.) Schematic showing the location of BMI injection and saline injection (control). B, BMI injection; S, saline injection. (c.) Reconstructed PAT image before (left) and after (right) the BMI injection. The BMI and saline were injected into the left and right parietal neocortex, respectively. A significant increase of optical absorption is seen in the region of the BMI injection, while no absorption contrast is observed in the region of the saline injection relative to its surroundings. (d.) Series of PAT images from three representative transver planes parallel to the skin surface with 755 nm wavelength. Slices 5, 7, and 9 are the images obtained 3, 5 and 7 mm under the skin, respectively. The images show different spatial patterns at the seizure foci at different tomographic layers. (e.) Three dimensional rendering of the epileptic foci from different tomographic layers (Movie S2).

the tissue based on compensating the reconstructed image with a pre-calculated optical fluence distribution (Yao et al., 2009; Yuan et al., 2007). It is possible to achieve higher resolution at cellular and even sub-cellular levels to image the neuronal circuitry *in vivo* by use of photoacoustic microscopy at a depth of more than 3 mm (Shelton and Applegate; Hu et al., 2010). The findings imply that PAT has potential for noninvasive real time brain mapping of cortical processing and seizures.

A key advantage of our noninvasive PAT system for epileptiform event monitoring is the real time imaging ability. Seizures are generated by complex interactions of a large group of neurons in which the population of neurons involved varies largely from moment to moment (Schwartz and Bonhoeffer, 2001). By achieving 1000 times faster data acquisition of the current PAT imaging system relative to our previous PAT system (Zhang et al., 2008), we were able to observe that the spatial aspects of the seizure focus varied over time as suggested by the changes in hemodynamics (Fig. 4c). At present, the imaging speed was limited only by the 10 Hz laser pulse-repetition-rate. Since considerably faster lasers of ~500 Hz pulse-repetition-rates are now commercially available, the temporal resolution of PAT will soon reach a level of a few milliseconds. The light fluence on the skin was less than 5 mJ/cm^2, well within the American National Standards Institute (Institute, 2007) safety limits. This, coupled with the compactness of an optical system makes it possible to bring a PAT system to the bedside for real time chronic noninvasive monitoring of seizures (Yang et al., 2007).

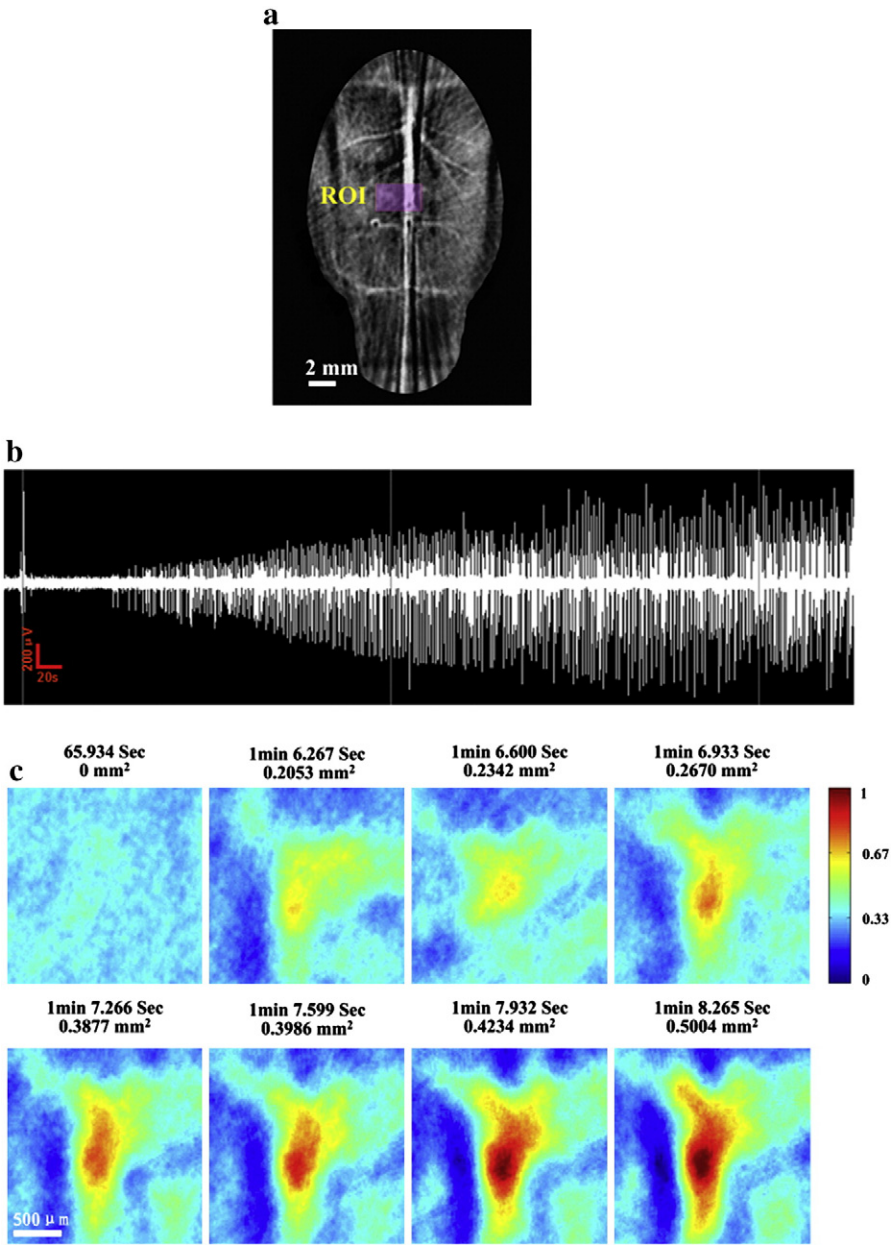

Fig. 4. Real-time monitoring of ictal onset. (a.) A PA image showing the cerebral vasculature and the position of BMI injection. ROI, region of interest; Scale bar: 2 mm. (b.) EEG recordings showing the seizure onset about 1 min after BMI injection. (c.) PAT images recording the ictal onset in real time. At 1 min 6.267 s the area of the focus was 0.2053 mm^2. The area of the focus then increased in size over the next 2 s to 0.5004 mm^2, corresponding to an increase in the amplitude of the EEG spikes. The area of the seizure focus was derived from the PAT images by thresholding to a pixel value one standard deviation above the pixel values from the area of the focus during the control conditions. Scale bar: 500 μm (Movie S3).

One hypothesis is that long-standing epilepsy may lead to the development of secondary epileptogenic regions located at a site distant from the original focus, a factor that may reduce the likelihood of successful epilepsy pre-surgical planning (Cendes et al., 1995). The ability to identify the epileptic focus and associated network may lead to better epilepsy surgery outcomes for many individuals. Various methods such as cross correlation and Granger causality have been explored for assessing the dynamic directional relationships among brain regions using time series data (Bressler et al., 2008; Kaminski et al., 2001). We used Granger causality as a way to quantify the dynamic interactions amongst the primary seizure focus, secondary seizure foci, and middle cerebral artery based on the time-series photoacoustic data. Specifically, Granger causality allowed for assessment of the magnitude and direction of temporal relationships during overlapping PAT time-series windows. Results further exemplified the temporal aspects of seizure onset, seizure secondary spread, and seizure termination. Collectively, PAT image analysis and tools for effective connectivity may result in a better understanding of epileptic networks at high spatiotemporal resolution.

Little data are available regarding a link between vascular changes and seizures (Ndode-Ekane et al., 2010). We found that the vasomotor phenomena of micro blood vessels correlate with interictal spike and wave discharges (Fig. 6d). Interictal spikes generated a strong cerebral metabolic change that induced cerebral vessel dilation and a focal increase in cerebral blood flow provided oxygenated hemoglobin to hypermetabolic neurons, with a corresponding increase in total hemoglobin (Ma et al., 2009). Vasomotion during seizure onset and spread was clearly caused by the oscillation in vessel diameter

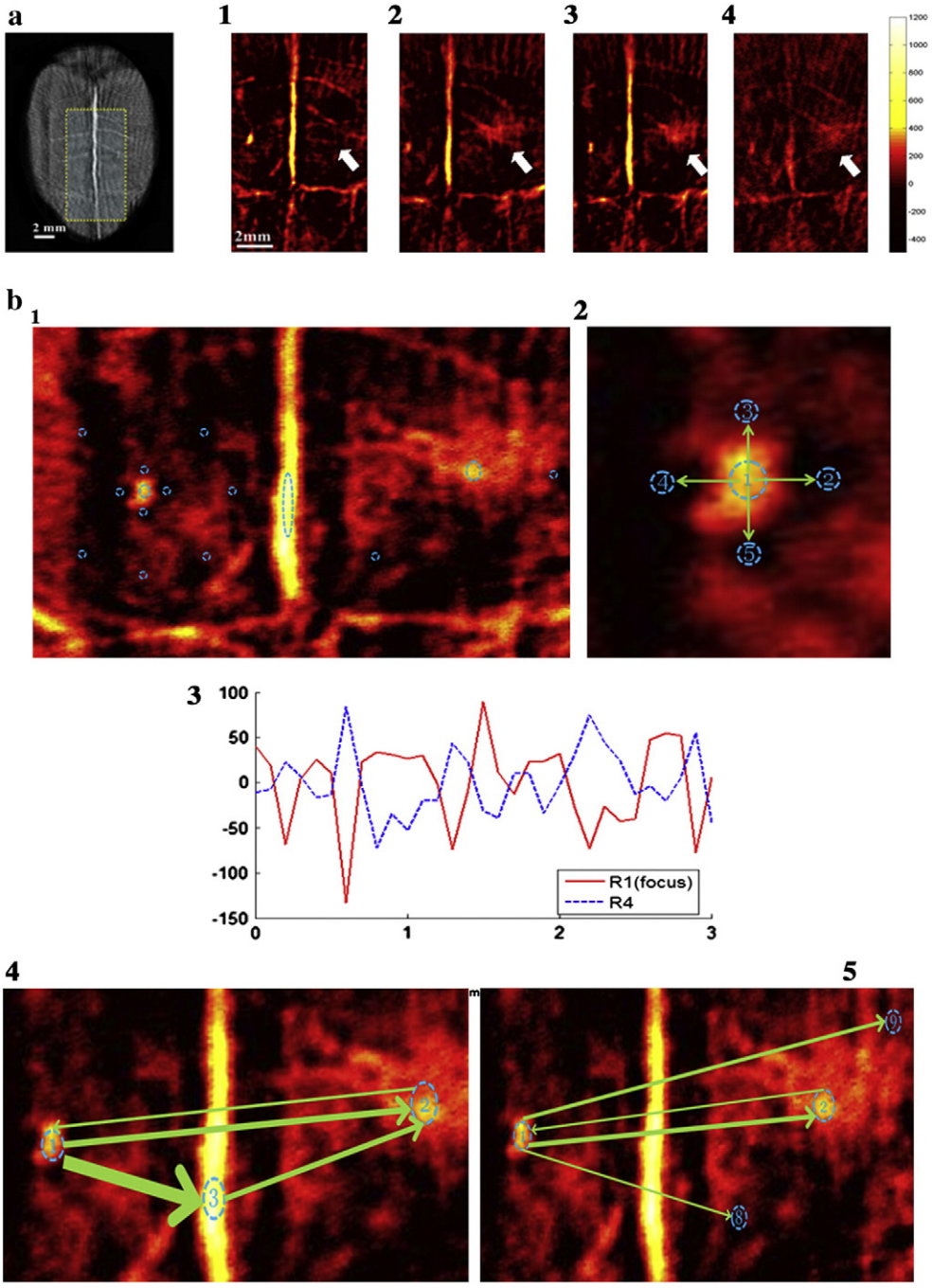

Fig. 5. *In vivo* maps of mirror foci propagation. (a.) Left, the PA image of the rat brain; the yellow dotted rectangular shows the ROI for analysis; Right, noninvasive imaging of the primary and mirror foci in bilateral homotopic cortex. a1–4 shows how mirror foci were generated and diminished. White arrow shows the location of mirror foci. The PA signal in the mirror foci was smaller in magnitude and delayed in time compared to the signal recorded from the primary foci. (b.) Granger analysis of seizure foci, mirror foci and middle cerebral artery; b1, a PAT image showing the nine selected ROIs; b2, Granger analysis of the image around the foci and its 'surround' area; b3, PA signal from the foci (red) and surround (blue) during an ictal event. The PA signal surrounding the foci (blue line) shows inverted signal compared to that from the seizure foci (red line) corresponding to neuronal inhibition. b4, connectivity relation between the primary and mirror focus; b5, connectivity relation between the primary focus, mirror focus and middle cerebral artery. The line width stands for the relative Granger causal influence strength. (For interpretation of the references to color in this figure legend, the reader is referred to the web of this article.)

and the expansion of the vessel cross section. We reasoned that the dilation resulted in an active cerebral microvasculature response to increased metabolic activity accompanying the seizure (Myers and Intaglietta, 1976). The combination of multi-scale imaging ability and endogenous hemoglobin contrast makes PAT a promising tool for imaging microvasculature during seizure onset. Future quantitative PAT studies will allow us to resolve many of the hemodynamic components, including changes in level of hemoglobin oxygenation (i.e., deoxy- and oxy-hemoglobin), cerebral blood flow, and the rate of cerebral oxygen metabolism, for a detailed understanding of the neurovascular coupling phenomenon, both during and in between seizures(Yao et al., 2009; Yuan et al., 2007).

The present work represents a major technological and scientific improvement in epilepsy. Previous attempts to track from moment to moment populations of neurons participating in an epileptiform event had not been possible with any technique or tool because of

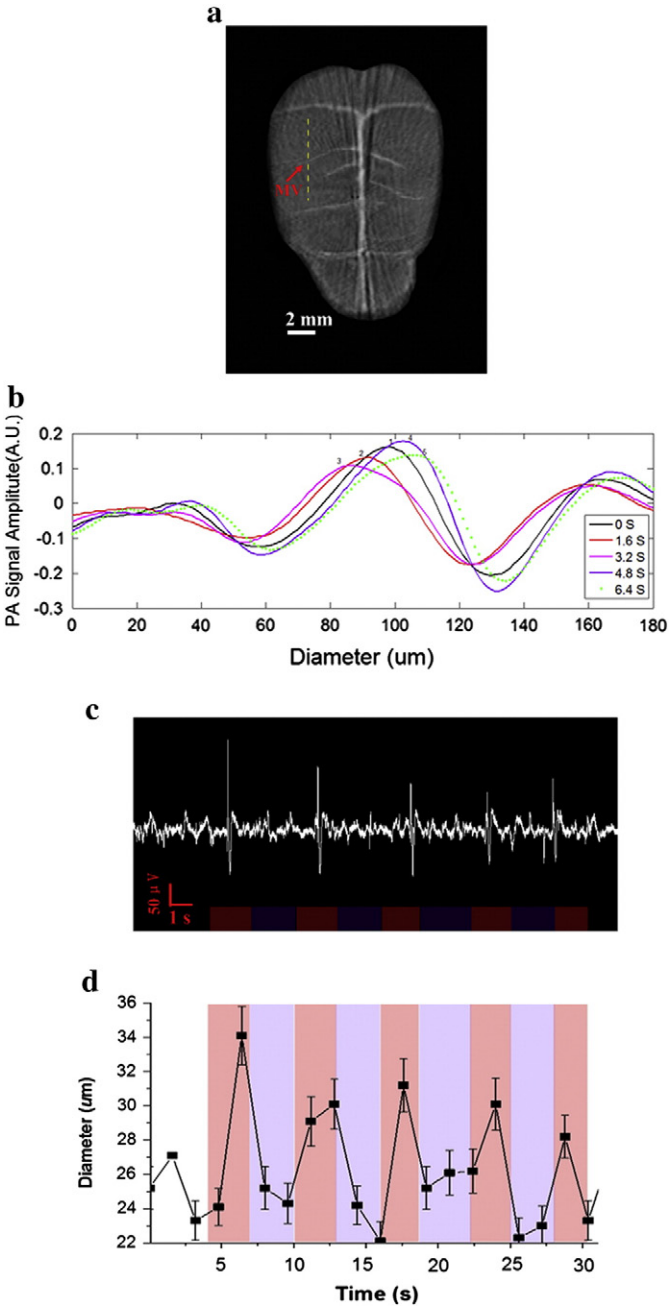

Fig. 6. Changes of blood vessel diameter during interictal onset. (a.) PA image of the rat cortex vasculature with the intact scalp and skull. The red arrow indicates the microvascularity (MV) along the yellow dashed line direction for a cross-sectional scanning using a 50 MHz ultrasound transducer. (b.) Typical photoacoustic signals from the targeted vessel at different times. (c.) EEG recordings show the interictal spikes and (d.) Change of the vessel size captured by PAT. Here was a clear correlation between the interictal spikes and the changes of the vessel size. Error bars (±s.d.) were calculated from 20 consecutive spikes. (For interpretation of the references to color in this figure legend, the reader is referred to the web of this article.)

spatial and/or temporal sampling limitations. The high spatial and temporal sampling of the novel PAT system allowed for the first time the complete mapping of an epileptiform event *in vivo*. Another major improvement is that this is the first report of mapping an epileptiform event at depths well below the cortex. In terms of impact, this is the first demonstration of emerging optical mapping tool in the surgical evaluation of focal cortical epilepsy, since accurate localization of the epileptic focus, propagation paths, and subcortical networks critically depends on the precise localization of epileptogenic neurons and networks. The use of our PAT system, experimental paradigm, results, and analyses advances our understanding of epilepsy and seizure temporal spatial properties relative to previous attempts. The noninvasive yet whole surface and depth capabilities of the PAT system allowed for the first time to actually see what is happening during ictogenesis in terms of seizure onset and spread. The challenge of mapping focal epilepsy stems from the observation that the pathology associated with focal epilepsy is often distributed across a number of brain sites. Seizures in animal models and in people often have a multifocal or broadly synchronized onset. The implication of these observations is that each of the sites could act independently to initiate a seizure or, potentially, to drive another site into a seizure. The current study lends support to the theory that seizure onset and spread involves a rich interplay between multiple cortical and subcortical foci during the onset and spread of focal epilepsy. The findings are timely in the sense that the neuroscience community is questioning the long-held dogma that seizure onset involves some sort of single focus or epicenter in favor of the emerging thought that seizures instead involve multiple cortical and subcortical foci.

Acknowledgments

This research was supported in part by a grant from the US Department of Defense Congressionally Directed Medical Program, the B.J. and Eve Wilder endowment fund, and the Children's Miracle Network.

Appendix A. Supplementary data

Supplementary data to this article can be found online at http://dx.doi.org/10.1016/j.neuroimage.2012.10.077.

Reference

Berg, A.T., Langfitt, J.T., Spencer, S.S., Vickrey, B.G., 2007. Stopping antiepileptic drugs after epilepsy surgery: a survey of U.S. epilepsy center neurologists. Epilepsy Behav. 10, 219–222.
Bertram, E.H., 2009. Temporal lobe epilepsy: where do the seizures really begin? Epilepsy Behav. 14, 32–37.
Bertram, E.H., Zhang, D.X., Mangan, P., Fountain, N., Rempe, D., 1998. Functional anatomy of limbic epilepsy: a proposal for central synchronization of a diffusely hyperexcitable network. Epilepsy Res. 32, 194–205.
Birbeck, G.L., Hays, R.D., Cui, X., Vickrey, B.G., 2002. Seizure reduction and quality of life improvements in people with epilepsy. Epilepsia 43, 535–538.
Bluestone, A.Y., Abdoulaev, G., Schmitz, C.H., Barbour, R.L., Hielscher, A.H., 2001. Three-dimensional optical tomography of hemodynamics in the human head. Opt. Express 9, 272–286.
Boas, D.A., Gaudette, T., Strangman, G., Cheng, X., Marota, J.J., Mandeville, J.B., 2001. The accuracy of near infrared spectroscopy and imaging during focal changes in cerebral hemodynamics. Neuroimage 13, 76–90.
Bressler, S.L., Tang, W., Sylvester, C.M., Shulman, G.L., Corbetta, M., 2008. Top-down control of human visual cortex by frontal and parietal cortex in anticipatory visual spatial attention. J. Neurosci. 28, 10056–10061.
Brovelli, A., Ding, M., Ledberg, A., Chen, Y., Nakamura, R., Bressler, S.L., 2004. Beta oscillations in a large-scale sensorimotor cortical network: directional influences revealed by Granger causality. Proc. Natl. Acad. Sci. U. S. A. 101, 9849–9854.
Cadotte, A.J., DeMarse, T.B., Mareci, T.H., Parekh, M.B., Talathi, S.S., Hwang, D.U., Ditto, W.L., Ding, M.Z., Carney, P.R., 2010. Granger causality relationships between local field potentials in an animal model of temporal lobe epilepsy. J. Neurosci. Methods 189, 121–129.
Cendes, F., Cook, M.J., Watson, C., Andermann, F., Fish, D.R., Shorvon, S.D., Bergin, P., Free, S., Dubeau, F., Arnold, D.L., 1995. Frequency and characteristics of dual pathology in patients with lesional epilepsy. Neurology 45, 2058–2064.
Denk, W., Strickler, J.H., Webb, W.W., 1990. Two-photon laser scanning fluorescence microscopy. Science 248, 73–76.
Duncan, J.S., Sander, J.W., Sisodiya, S.M., Walker, M.C., 2006. Adult epilepsy. Lancet 367, 1087–1100.
Engel, J., 2004. The goal of epilepsy therapy: no seizures, no side effects, as soon as possible. CNS Spectr. 9, 95–97.
Folbergrová, J., Ingvar, M., Siesjö, B.K., 1981. Metabolic changes in cerebral cortex, hippocampus, and cerebellum during sustained bicucullineinduced seizures. J. Neurochem. 37, 1228–1238.
Fountain, N.B., Bear, J., Bertram, E.H., Lothman, E.W., 1998. Responses of deep entorhinal cortex are epileptiform in an electrogenic rat model of chronic temporal lobe epilepsy. J. Neurophysiol. 80, 230–240.
Granger, C.W.J., 1969. Investigating causal relations by econometric models and cross-spectral methods. Econometrica 37 (414-&).

Greenfield, J., Geyer, J., Carney, P.R., 2011. Reading EEGs: a Practical Approach. Lippincott Wilkins Raven, Philadelphia.
Grinvald, A., Frostig, R.D., Lieke, E., Hildesheim, R., 1988. Optical imaging of neuronal-activity. Physiol. Rev. 68, 1285–1366.
Haglund, M.M., Hochman, D.W., 2004. Optical imaging of epileptiform activity in human neocortex. Epilepsia 45, 43–47.
Haglund, M.M., Ojemann, G.A., Hochman, D.W., 1992. Optical imaging of epileptiform and functional activity in human cerebral cortex. Nature 358, 668–671.
Hauser, W.A., 1992. Seizure disorders: the changes with age. Epilepsia 33 (Suppl. 4), S6–14.
Hauser, W.A., Annegers, J.F., Rocca, W.A., 1996. Descriptive epidemiology of epilepsy: contributions of population-based studies from Rochester, Minnesota. Mayo Clin. Proc. 71, 576–586.
Hill, D.K., Keynes, R.D., 1949. Opacity changes in stimulated nerve. J. Physiol. (Lond.) 108, 278–281.
Hu, S., Rao, B., Maslov, K., Wang, L.V., 2010. Label-free photoacoustic ophthalmic angiography. Opt. Lett. 35, 1–3.
Huang, D., Swanson, E.A., Lin, C.P., Schuman, J.S., Stinson, W.G., Chang, W., Hee, M.R., Flotte, T., Gregory, K., Puliafito, C.A., Fujimoto, J.G., 1991. Optical coherence tomography. Science 254, 1178–1181.
Institute, A.N.S., 2007. American national standard for the safe use of lasers. ANSI z136.1. Laser Institute of America, Orlando, Fla.
Jeha, L.E., Najm, I., Bingaman, W., Dinner, D., Widdess-Walsh, P., Luders, H., 2007. Surgical outcome and prognostic factors of frontal lobe epilepsy surgery. Brain 130, 574–584.
Jiang, H.B., Paulsen, K.D., Osterberg, U.L., Pogue, B.W., Patterson, M.S., 1996. Optical image reconstruction using frequency-domain data: simulations and experiments. J. Opt. Soc. Am. A 13, 253–266.
Kaminski, M., Ding, M.Z., Truccolo, W.A., Bressler, S.L., 2001. Evaluating causal relations in neural systems: Granger causality, directed transfer function and statistical assessment of significance. Biol. Cybern. 85, 145–157.
Khalilov, I., Holmes, G.L., Ben-Ari, Y., 2003. In vitro formation of a secondary epileptogenic mirror focus by interhippocampal propagation of seizures. Nat. Neurosci. 6, 1079–1085.
Kruger, R.A., Liu, P.Y., 1994. Photoacoustic ultrasound — pulse production and detection in 0.5-percent liposyn. Med. Phys. 21, 1179–1184.
Laufer, J., Delpy, D., Elwell, C., Beard, P., 2007. Quantitative spatially resolved measurement of tissue chromophore concentrations using photoacoustic spectroscopy: application to the measurement of blood oxygenation and haemoglobin concentration. Phys. Med. Biol. 52, 141–168.
Ma, H., Zhao, M., Suh, M., Schwartz, T.H., 2009. Hemodynamic surrogates for excitatory membrane potential change during interictal epileptiform events in rat neocortex. J. Neurophysiol. 101, 2550–2562.
Mace, E., Montaldo, G., Cohen, I., Baulac, M., Fink, M., Tanter, M., 2011. Functional ultrasound imaging of the brain. Nat. Methods 8, 662–U685.
Mangan, P.S., Scott, C.A., Williamson, J.M., Bertram, E.H., 2000. Aberrant neuronal physiology in the basal nucleus of the amygdala in a model of chronic limbic epilepsy. Neuroscience 101, 377–391.
Myers, R.R., Intaglietta, M., 1976. Brain microvascular hemodynamic responses to induced seizures. Stroke 7, 83–88.
Ndode-Ekane, X.E., Hayward, N., Grohn, O., Pitkanen, A., 2010. Vascular changes in epilepsy: functional consequences and association with network plasticity in pilocarpine-induced experimental epilepsy. Neuroscience 166, 312–332.
Ogawa, S., Lee, T.M., Nayak, A.S., Glynn, P., 1990. Oxygenation-sensitive contrast in magnetic-resonance image of rodent brain at high magnetic-fields. Magn. Reson. Med. 14, 68–78.
Oleary, M.A., Boas, D.A., Chance, B., Yodh, A.G., 1995. Experimental images of heterogeneous turbid media by frequency-domain diffusing-photon tomography. Opt. Lett. 20, 426–428.
Paxinos, G.W.C., 1998. The Rat Brain. Academic Press.
Schwartz, T.H., Bonhoeffer, T., 2001. *In vivo* optical mapping of epileptic foci and surround inhibition in ferret cerebral cortex. Nat. Med. 7, 1063–1067.
Shelton, R.L., Applegate, B.E., 2010. Ultrahigh resolution photoacoustic microscopy via transient absorption. Biomed, Opt Express 1, 676–686.
Sipkins, D.A., Wei, X.B., Wu, J.W., Runnels, J.M., Cote, D., Means, T.K., Luster, A.D., Scadden, D.T., Lin, C.P., 2005. In vivo imaging of specialized bone marrow endothelial microdomains for tumour engraftment. Nature 435, 969–973.
Sokol, D.K., Markand, O.N., Daly, E.C., Luerssen, T.G., Malkoff, M.D., 2000. Near infrared spectroscopy (NIRS) distinguishes seizure types. Seizure 9, 323–327.
Steinhoff, B.J., Herrendorf, G., Kurth, C., 1996. Ictal near infrared spectroscopy in temporal lobe epilepsy: a pilot study. Seizure 5, 97–101.
Thom, M., Mathem, G.W., Cross, J.H., Bertram, E.H., 2010a. Mesial temporal lobe epilepsy: how do we improve surgical outcome? Ann. Neurol. 68, 424–434.
Thom, M., Mathern, G.W., Cross, J.H., Bertram, E.H., 2010b. Mesial temporal lobe epilepsy: how do we improve surgical outcome? Ann. Neurol. 68, 424–434.
Wang, X., Chen, Y.H., Bressler, S.L., Ding, M.Z., 2007. Granger causality between multiple interdependent neurobiological time series: blockwise versus pairwise methods. Int. J. Neural Syst. 17, 71–78.
Watanabe, E., Maki, A., Kawaguchi, F., Yamashita, Y., Koizumi, H., Mayanagi, Y., 2000. Noninvasive cerebral blood volume measurement during seizures using multichannel near infrared spectroscopic topography. J. Biomed. Opt. 5, 287–290.
Xiang, L.Z., Xing, D., Gu, H.M., Yang, D.W., Yang, S.H., Zeng, L.M., Chen, W.R., 2007. Real-time optoacoustic monitoring of vascular damage during photodynamic therapy treatment of tumor. J. Biomed. Opt. 12.
Yang, S.H., Xing, D., Lao, Y.Q., Yang, D.W., Zeng, L.M., Xiang, L.Z., Chen, W.R., 2007. Noninvasive monitoring of traumatic brain injury and post-traumatic rehabilitation with laser-induced photoacoustic imaging. Appl. Phys. Lett. 90.
Yao, L., Sun, Y., Jiang, H.B., 2009. Quantitative photoacoustic tomography based on the radiative transfer equation. Opt. Lett. 34, 1765–1767.
Yuan, Z., Wang, Q., Jiang, H.B., 2007. Reconstruction of optical absorption coefficient maps of heterogeneous media by photoacoustic tomography coupled with diffusion equation based regularized Newton method. Opt. Express 15, 18076–18081.
Zhang, Q.Z., Liu, Z., Carney, P.R., Yuan, Z., Chen, H.X., Roper, S.N., Jiang, H.B., 2008. Noninvasive imaging of epileptic seizures in vivo using photoacoustic tomography. Phys. Med. Biol. 53, 1921–1931.

Simultaneous EEG and photoacoustic monitoring of epilepsy in freely moving rats

Bo Wang, Junli Zhou, Paul Carney, Huabei Jiang*

Department of Biomedical Engineering
University of Florida

*Corresponding author: hjiang@bme.ufl.edu

Abstract

Study of neuro-hemodynamic activities in freely moving small animals (rather than anesthetized) provides more realistic and accurate information about diseases, and hence better understanding. While it has been proved that hemodynamic changes are closely related to epileptic seizures, methods for detection in freely moving (small) animals are limited. In this work, we integrated photoacoustic sensor and EEG system into a small device that can be attached on the head of awaken rats, and for the first time it shows the realization of long time and simultaneous monitoring of photoacoustic and EEG signals in pentylenetetrazol (PTZ) induced seizure on freely moving small animals i.e., rats. Results showed that both the neural and vascular responses to seizure in freely moving rats have characteristics, which are observed to be different and more diverse from that of anesthetized rats, and this calls for more detailed study in future. This technology also promises for other hemodynamic related research study in freely moving small animals.

Introduction

Epilepsy is the most common brain disease that affects 1% of the world population [1]. Epileptic seizures are caused by synchronous, rhythmic firing of a population of neurons in the brain that involves enormous increase in metabolic rate of oxygen and thus hemodynamic parameters such as cerebral blood flow (CBF), cerebral blood volume (CBV) and oxy-saturation are greatly changed [2]. A better understanding of coupling between the neural and vascular systems is crucial to diagnosis, prediction and treatment for this disease.

Currently available neural imaging modalities such as functional magnetic resonance imaging (fMRI), positron emission tomography (PET), single-photon emission computed tomography (SPECT), have already been employed in the study of neurovascular coupling in epilepsy both in human and animal models [2, 3]. However, one remaining problem for these technologies is that they are expensive and bulk in size, so the objects must be anesthetized or keep still during the entire recording process. For recently developed optical mapping methods such as optical recording of intrinsic signals (ORIS), optical coherence tomography (OCT) and voltage sensitive dye, pre-operation surgeries like skull opening are generally required due to their limited imaging depth [4, 5] and thus they permit only anesthetized animals.

Problem associated with anesthetized animals is: the anesthetization suppresses the activities of neurons and cardiovascular system, so the neural and vascular responses to seizure are altered [6].

As a consequence, awakening and freely moving animals with vascular response uninterrupted by extrinsic factors is ideal and preferred model for epilepsy study. Conventional EEG or telemetric EEG system with video monitoring is the gold standard for seizure detection and quantification, and has already been widely used on freely moving animals [7, 8]. Yet the compact devices, which can be firmly fixed on the animals and hence can reliably detect hemodynamic changes, are still missing and no studies have been reported.

Photoacoustic technologies have been widely employed in vascular network visualization of small animal brain, tumor detection, and in early osteoarthritis diagnosis [9-12]. In photoacoustic effect when a short pulse of laser light is absorbed by tissue, wideband ultrasound signal that conveys the position and absorbed energy of the tissue is generated due to transient thermoelastic expansion. In this way, it compromises the merits of high spatial resolution and imaging depth from ultrasound imaging, and high intrinsic optical contrast from optical imaging. It has been used for neurovascular coupling study of epilepsy with anesthetized animals [9, 10]. However, most of the photoacoustic techniques focus on imaging that permits only the anesthetized animals. Besides, the imaging speed of photoacoustic systems is often limited by the laser repetition rate. On other hand, its potential for real-time monitoring as a sensor in simple and compact design that can be used on freely moving animals is not fully explored.

The purpose of this work is to develop an interface that consists of an EEG system and a photoacoustic sensor, and to study the interaction between the EEG signal and the hemodynamic signal of superior sagittal sinus (SSS) in pentylenetetrazol (PTZ) induced seizure on freely moving rats. PTZ has been employed to induce generalized seizure in rats to study seizure phenomenon, where hemodynamic changes have reportedly been found all over the brain. As one of the most distinguishable as well as main blood vessels in brain, SSS allows blood to drain from lateral aspects of anterior cerebral hemisphere to confluence of sinuses and return to venous circulation, covering large region of brain. Thus the hemodynamic signal of SSS is closely related to the status of the PTZ-induced generalized seizure.

Through this dual-modality, monitoring epilepsy in freely moving animals, one can get an in-depth knowledge of responses from vascular and neural systems, and hence better understanding of mechanisms of epilepsy. This technology may have greater utility in applications such as drug development and therapy assessment in epilepsy, and other hemodynamic related studies.

Material and methods

(1) System overview

The entire system can be divided into four main parts as: photoacoustic system, EEG system, video camera, and small interface mounted on rat head, as shown in Fig. 1. Pulse light of wavelength, 1064nm from a Q-switch Nd:YAG laser operating at 10Hz was coupled into a 0.4mm core multimode fiber patch cable using a convex lens and delivered to the rat brain. The transient photoacoustic signal generated by the short laser pulse was detected by a pair of transducers with central frequency 5MHz. The signal was amplified using a 26dB PCB preamplifier and a 17dB commercial preamplifier (AH-1100, ONDA Co.), and finally digitalized by a PCI DAQ card (NI

PCI-5154) with sampling rate 50MHz. The intracranial EEG signal was collected through a pair of small screws drilled in the skull of rat. The depth of the screws through the skull was about 1mm. The EEG signal was amplified (RA16PA, TDtucker-Davis Tech.), and collected (RZ5 Bioamp Processor, TDtucker-Davis Tech.) and stored into a computer for processing later. The entire system was synchronized through triggering with Nd:YAG laser. Continuous video recording was achieved with a video camera (we used iPhone 4S). The transducers, multimode fiber and EEG connecting wires are detachable from the rat head when the experiment is over. All the data including the photoacoustic signal, EEG signal and video are jointly analyzed later for study of epilepsy.

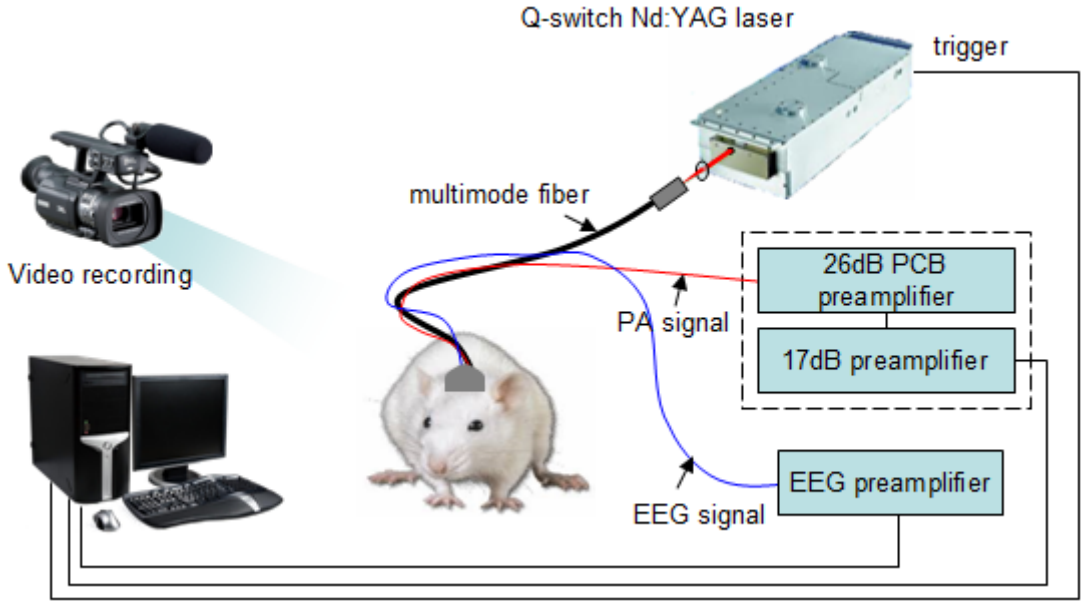

Fig. 1: Schematic of experimental system. The integration of photoacoustic system, EEG system, video camera, and small interface mounted on the rat head is depicted.

(2) Photoacoustic sensor design

Fig. 2(a) depicts the schematic of photoacoustic sensor being mounted on a rat head. Core multimode fiber patch cable (0.4mm) for delivery of light was connected to an optical cannula (CFMC14L02, Thorlabs Inc.) with a ceramic mating sleeve (see Fig. 2(b)). The cannula was implanted right above SSS, with a tip (2mm) reaching into brain through a small hole in skull. In rat experiment, the optical energy coming out of the multimode fiber was about 6mJ/pulse and that from the connula tip into the brain was about 4mJ/pulse. The cannula was fixed with dental cement, and then the skull surface was sealed with a thin layer of super glue. The two transducers were tilted and placed with their axes pointing to SSS. They were supported by a 3D printed VeroWhitePlus interface and fastened with small screws and thermal glue. The space between the skull and the transducers was filled with ultrasound gel for proper acoustic coupling. Fig. 2(c) shows a photograph of the above-mentioned design being mounted on rat head (after the surgery).

(3) Surgery

Four Sprague Dawley rats, whose weights were around 400g, were employed in the experiments. SSS was about 2mm below the skull. Fig. 3 shows the top view of a rat skull during surgery. The positions of the optical cannula and the two EEG electrodes are noted by arrows. The surgery was

carried out as follows. Firstly, rat was anesthetized with isoflurane and hair on the head was removed, and subsequently, the scalp was opened. Next, a hole of diameter 0.5mm was carefully drilled in the skull, and cannula was inserted into the hole and fixed with dental cement. The surface of the skull was cleaned and applied with antibiotic, and then sealed with a thin layer of super glue to prevent from infection. After that, two small screws were drilled at forehead and they served as two EEG electrodes. Finally, 3D Printed VeroWhitePlus interface was fixed onto the rat skull with dental cement, and the two EEG screws were also embedded in dental cement, leaving two wires tied on the screws stretching out for later connecting to recording leads. After four days (for complete recovery), rat was adopted for (epilepsy) experiment. All the procedures were carried out in accordance with an approved University of Florida IACUC protocol.

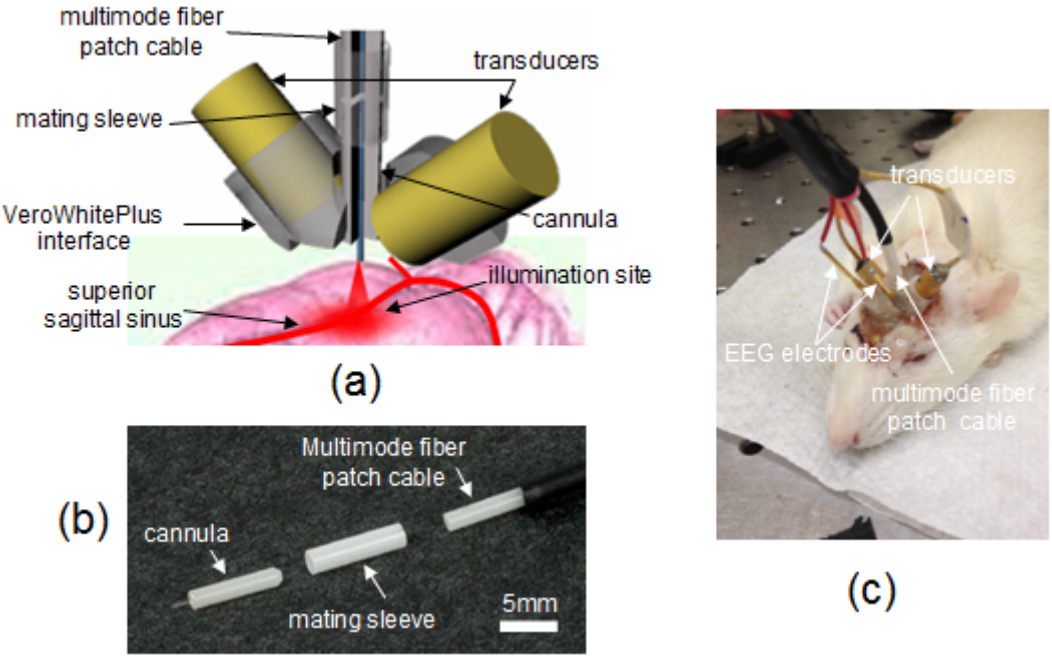

Fig. 2: (a) Schematic of the photoacoustic sensor in 3D. Laser is delivered to SSS through an optical cannula, which is implanted on rat skull. Then a pair of transducers receives the generated ultrasound signals. The diameter of the receiving transducers is approximately 5.5mm, and they are supported by a 3D printed VeroWhitePlus interface. (b) Photograph of optical cannula, mating sleeve and multimode fiber patch cable. The optical cannula has a diameter of 2.5mm, with a piece of core multimode fiber (0.4mm) in its center. (c) Photograph of rat head, with all detectors being connected, after surgery. The EEG electrodes are implanted in forehead of the rat, as indicated.

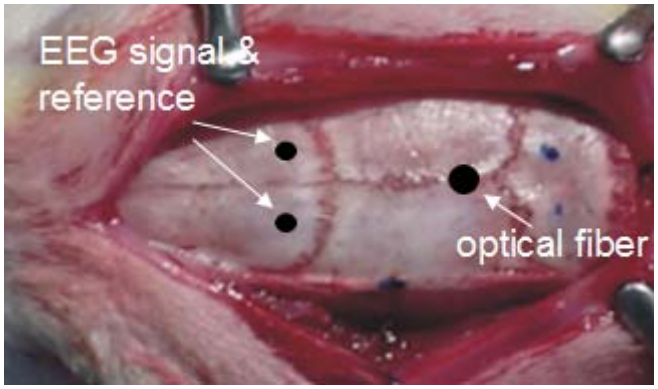

Fig. 3: Photograph of a rat skull while in surgery, with the positions of optical cannula and EEG electrodes as indicated by arrows.

(4) Data collection and processing

Phantom experiments were carried out to validate the photoacoustic signal from SSS. A tube with inner diameter 0.2mm was filled with ink, and embedded in a phantom (we employed agar phantom) at a depth of 2mm. Then VeroWhitePlus interface along with optical cannula and transducers was placed onto the phantom to record the photoacoustic signal from the tube. By comparing the resulting photoacoustic signal with that of rat experiments, the photoacoustic signal of SSS can be verified (amplitude vs. time was calculated). Because the optical absorption at wavelength 1064nm is dominantly sensitive to oxy-hemoglobin (HbO_2) as compared to that of deoxy-hemoglobin (HbR), the photoacoustic signal at this wavelength can be taken as the volume change of HbO_2 in SSS [13]. For each experiment, the signals from the two transducers were compared, and the better one was selected for recording.

There were two strong sources of noise in the collected EEG data. One is from the alternating current supply at 60Hz and other is from Q-switch of the laser at 10Hz (Fig. 4(b), blue line). The EEG data was firstly Fourier transformed and the alternating current noise of 60Hz was eliminated by filtering out the frequency band in the range 58Hz to 62Hz, and the Q-switch noise was removed by filtering out the frequency band of 10 ± 0.5Hz, 20 ± 0.5Hz, 30 ± 0.5Hz… and so forth (Fig. 4(a)). Then the filtered EEG data was inverse Fourier transferred back to obtain the time resolved data (red line as shown in Fig. 4(b)).

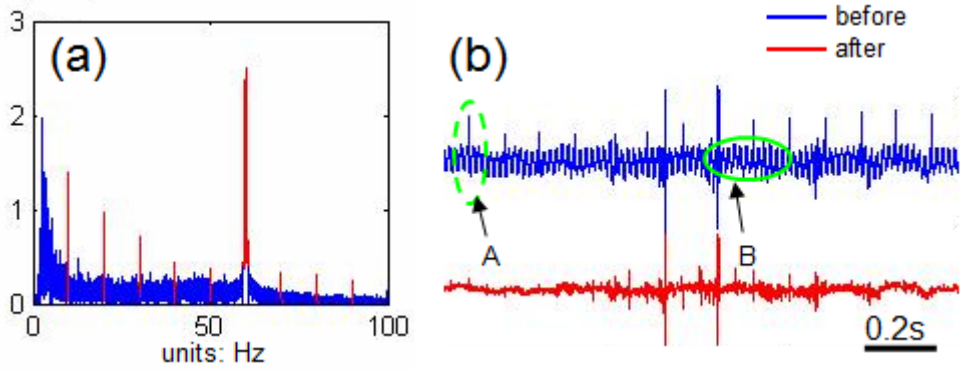

Fig. 4: EEG data de-noising in frequency domain. (a) Frequency power chart of EEG signal (before de-noise (red) and after de-noise (blue)). (b) EEG signal before (blue) and after (red) de-noise. The noises are indicated with arrow and green encircles: A (the Q-switch noise (10Hz) from the laser) and B (the alternating power supply noise (60Hz)).

(5) Rat experiments

All the rat experiments were carried out between 2:00pm and 5:00pm. The rats were first placed in an acrylic cage and acclimatized for at least one hour before the experiment. Then the rats were anaesthetized, and the EEG leads, the multimode fiber, and the transducers were connected to the head of rats for recording.

For free moving rat, the seizure experiment was initiated around 10min after the awake of rat, in

which seizures were generated by injecting PTZ of 30-75mg/Kg into abdomen [14]. Two kinds of control tests were performed. In first case, sterile saline of same volume was injected, and in other case, rats were continuously anesthetized with a PTZ dose of 120mg/Kg. The concentration for PTZ was fixed to 50mg/mL. The duration of recording is 30mins for each experiment, and the injection of drug was induced around 5mins. Behavioral seizures of all rats were scored using 5-graded Racine Score system [15], and the score was based on the severest behavior of rats. A total number of 22 experiments (n=22) were carried out using 4 rats, as shown in Table 1. The time interval between two experiments for the same rat was at least 3 days. All the results were confirmed by experts in neurology.

Table 1: Experiment design. The number in brackets indicates the number of rats that were successfully video recorded through 30mins. The star mark indicates that the rat died after experiment.

case number	rat1	rat2	rat3	rat4
anaesthetized	1*	1*	1	0
30mg/Kg PTZ	2(2)	1(1)	0	1(1)
50mg/Kg PTZ	2	4(1)	3(2)	0
75mg/Kg PTZ	0	0	0	1
control	2	1	2	0

Results

(1) Photoacoustic signal verification

Photograph of a phantom (employed in experiment) is shown in Fig. 5(a) and photoacoustic signals for phantom experiment (blue line) and rat experiment (red line) are shown in Fig. 5(b). Both the curves show strong and sharp bipolar signals at the instant around 3us with clear background, which is equivalent to about 5.3mm in tissue. We conclude that the photoacoustic signal from SSS is about 3us in rat experiment.

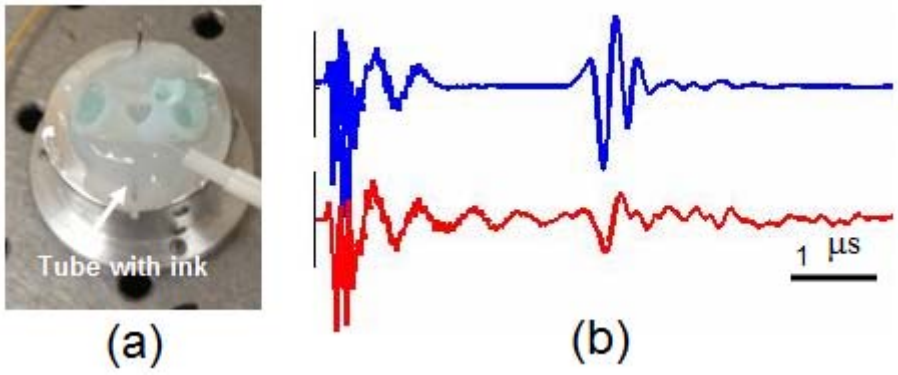

Fig. 5 Phantom experiment for validating photoacoustic signal of SSS. (a) Photograph of phantom. (b) Photoacoustic signals in phantom experiment (blue), and in rat experiment (red). The signal for SSS is at instant about 3.5us.

(2) Dose and behavior

In all unanesthetized rat experiments, the rat was put into an uncovered acrylic cage, as shown in Fig. 6. The dose of PTZ was carefully administrated ranging from 30~75mg/Kg. One rat died

shortly after a dose of 75mg/Kg, while all the rats injected with 50mg/Kg or under survived. During the seizure process, the rats showed behavior of facial clonus, head nodding, forelimb clonus, rearing and falling (loss of postural control; See supplemental video S. 1). The video was recorded about 0.5m in front of the cage with iPhone 4S. In some experiments, the rats in the cage were well trapped. In this case, the rats only turned around the two ends of the cage, and then the operator needed to turn the cage in opposite direction to prevent the multimode fiber from twisting. However, in other experiments, the rats jumped out of the box, or torn off the optical fiber and/or transducers. Thus, only 33% (3 out of 10) of the freely moving rat experiments with more than 50mg/Kg PTZ can be fully recorded all through the experiment (Table 1). No seizure was observed in the rats injected with sterile saline. In general, the severity of seizure tended to be higher with a higher dose of PTZ injection (see Fig. 7). For anesthetized rat experiments, the rats were continuously anesthetized with isoflurane breathing circuit, and the body temperature of the rats was maintained at 37^0C with a thermo pad.

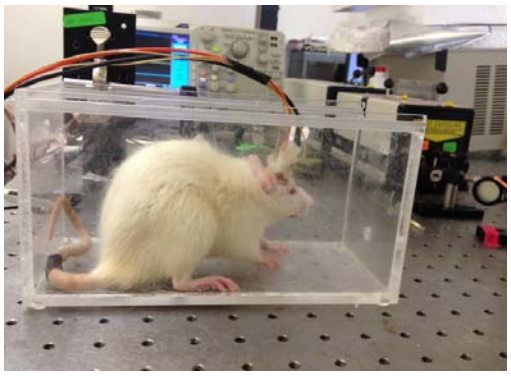

Fig. 6: Awake and freely moving rat in acrylic cage for experiments.

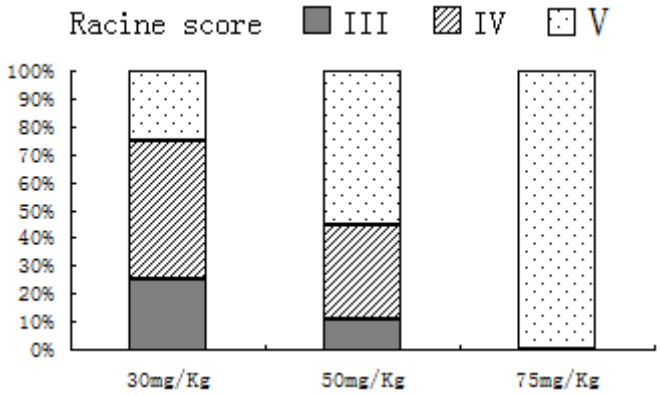

Fig. 7: Distribution of Racine score (in %) in freely moving rat seizure experiments for each PTZ dose.

(3) Simultaneous EEG and hemodynamic response study

Fig. 8 shows the experiment results of three different rat models: anaesthetized seizure model (Fig. 8(a)), control model (Fig. 8(c)), and freely moving seizure model (Fig. 8(b) using rat2 and Fig. 8(d) using rat3) respectively. All the injections were administrated at the instant 5min. By comparing these curves, we noted that these three different rat models showed distinguishable features for both HbO_2 (red) and EEG (blue) signals.

For anesthetized rats (with 120mg/Kg PTZ injection, Fig. 8(a)), there are few sharply isolated waves in the EEG signals before the administration of PTZ, and at the same time some fluctuations in HbO_2 are observed. The PTZ injection causes some high amplitude spikes in the EEG signal at 5min. After seizure begins, the EEG signal slowly increases in amplitude and frequency, and in the mean while, the HbO_2 signal first shows a sudden drop, and then gradually increases. Sooner after, some hypoxia gaps appear in the HbO_2 signal, which becomes wider and deep as seizure evolves. It's noted that two anesthetized rats were killed due to overdose of PTZ when they got awake after taking isoflurane breathing circuit away with completion experiments.

For freely moving rats (with 50mg/Kg PTZ injection) in Fig. 8(b), the EEG signal is active before the PTZ injection, while HbO_2 level is relatively stable. When the rats were caught and taken out for injection at 5min, the EEG signal activity becomes low, and the HbO_2 signal increases remarkably for a short interval of time. The seizure onset is about 3min after the injection. At the same time, the HbO_2 level increases significantly and then gradually gets lower, and the EEG signal displays continuous high amplitude that shows bursting activities. The result in Fig. 8(d) (with 0.5mg/Kg PTZ injection) is much different from that in Fig. 8(b). The fluctuation of HbO_2 signal in Fig. 8(d) is much larger (all through the experiments) than that in Fig. 8(b). The overall activity of EEG signal is prominently increased due to seizure onset in Fig. 8(d), but not in Fig. 8(b). Apparently, the results for freely moving rat experiments seemed more individual and case dependent.

For the test experiment under control (Fig. 8(c)), in which the rats were injected with 0.4mL of 0.9% sterile saline, no dramatic change is seen both in HbO_2 and EEG signals after the PTZ injection as compared to the signals before injection. It's also noted that the injection itself doesn't influence much either the HbO_2 signal or EEG signal as shown in Fig. 8(c), which is much different from the results for freely moving rat experiments in Fig. 8(b) and Fig. 8(d). This may be due to individual difference of rats.

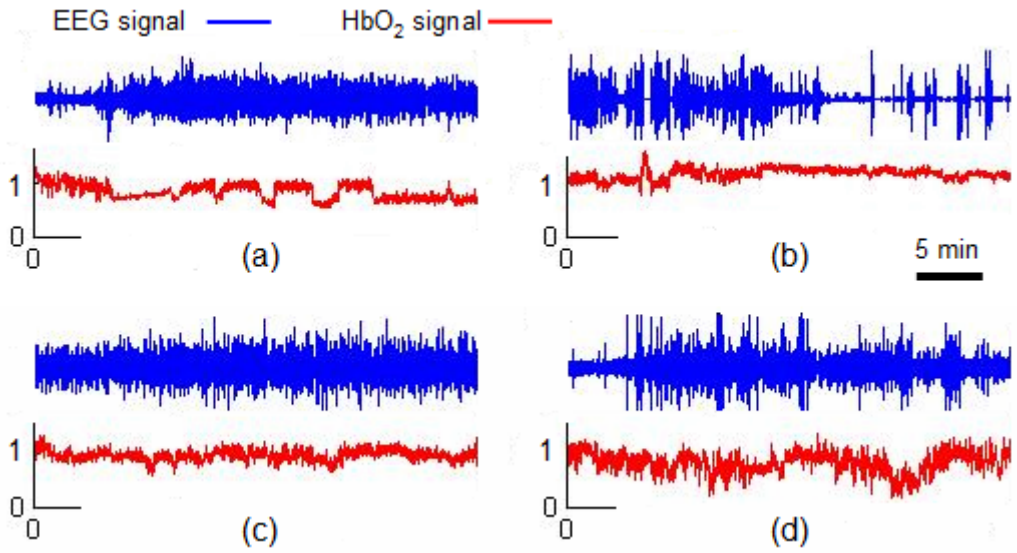

Fig. 8: EEG (blue) and HbO_2 (red) signals for rat experiments of different models. (a) Anaesthetized rat with 120mg/Kg PTZ injection. (c) Freely moving rat with 0.4mL injection of 0.9% sterile saline. (b) and (d) Freely

moving rats with 50mg/Kg PTZ injection.

Discussion

(1) The photoacoustic sensor design

Photoacoustic technologies have gained much attention for their diverse applications in biomedical imaging, but it's seldom used as a single sensor. In this work, we aim to integrate a photoacoustic sensor and EEG system in a small device for the dual modality study of epilepsy in free moving rats. By utilizing ultrasound as means of detection, the penetration depth of PAT can be much deeper than that of pure optical imaging while keeping high spatial resolution. Thus non-invasive detection of blood vessels in small rat brain can be achieved. However, in this work, small hole is required to be drilled in rat skull because laser light from multimode fiber can't penetrate scalp and skull of mature rat. Small rat can not be employed here because fiber and transducers can not be firmly attached to the loose scalp of small rats. There are other limitations in this work as well. For example, we only used one wavelength, but it can be easily adapted to dual wavelength measurement with the same Q-switch Nd:YAG laser; and multiple illumination and detection sites in the brain can also be realized too. All these can be improved in future work.

(2) Dual modality study with video monitoring

When rat was anesthetized, the fiber, transducers, and EEG leads were swayed but no notable fluctuations was observed in both the photoacoustic and the EEG signals, proving the reliability of the system. Video monitoring was used to confirm the presence of a motor component associated with an EEG seizure and to score the severity of motor seizures. We noticed that there are some artifacts in both the photoacoustic signal and EEG signal before the injection of drug, which are absolutely not related to seizure. These artifacts could not be discriminated without video monitoring.

For simultaneous monitoring of EEG and photoacoustic signals, the results for anesthetized rats are generally similar in which hypoxia gaps can be easily observed in the HbO_2 signal in all the cases. In contrast, results in freely moving rats are more case dependent and complicated than that of anaesthetized rats. In some experiments with freely moving rats, we also observed the proceeds of hemodynamic signal to the EEG signal; and EEG signals of different frequencies are decoupled sometimes. However, in this study, no statistic-based analysis is derived due to limited number of cases. The EEG and hemodynamic signal recordings after seizure (which we missed to carry out in this work) are also important and interesting issues for epilepsy study. As a result, more detailed study is required (in future) with more cases and longer observation time. But it is beyond the scope of this communication.

Conclusion

This study demonstrates the practicality of photoacoustic detection combined with EEG and video monitoring of epilepsy in freely moving rats. Rats with different seizure model were tested, and we found that the EEG and hemodynamic signals during seizure in freely moving rats are more complicated than that of anesthetized rats, which requires more detailed research in future. With the detachable design of fiber and transducers in this type of recording system, one rat can be used many times, allowing long-term studies of epilepsy. In our experiments, rats survived more than

one month until they were killed. With appropriate modifications, this technology can easily find other applications related to hemodynamic study than epilepsy, in which freely moving rat model is preferred.

Acknowledgement

This research was supported in part by a grant from the US Department of Defense Congressionally Directed Medical Program.

References

[1] Browne TR, Holmes GL. Epilepsy. New Engl J. Med. 344 (15): 1145-51, 2001.

[2] Theodore H Schwartz. Neurovascular Coupling and Epilepsy: Hemodynamic Markers for Localizing and Predicting Seizure Onset. Epilepsy Curr. 7 (4): 91–94, 2007.

[3] Theodore H. Schwartza, Seung-Bong Hongb, Andrew P. Bagshawc, Patrick Chauveld, Christian-G. Bénar. Preictal changes in cerebral haemodynamics: Review of findings and insights from intracerebral EEG. Epilepsy Res. 97: 252-266, 2011.

[4] Hongtao Ma, Mingrui Zhao, Theodore H. Schwartz. Dynamic Neurovascular Coupling and Uncoupling during Ictal Onset, Propagation, and Termination Revealed by Simultaneous In Vivo Optical Imaging of Neural Activity and Local Blood Volume. Cereb. Cortex. 23 (4): 885-899, 2013.

[5] Melissa M. Eberle, Carissa L. Reynolds, Jenny I. Szu, Yan Wang, Anne M. Hansen, Mike S. Hsu, M. Shahidul Islam, Devin K. Binder, and B. Hyle Park. In vivo detection of cortical optical changes associated with seizure activity with optical coherence tomography. Biomed. Opts. Exp. 3 (11): 2700-2706, 2012.

[6] A. Perks, S. Cheema, R. Mohanraj. Anaesthesia and epilepsy. British J. Anaesthesia. 108 (4): 562-571, 2012.

[7] Philip Williams, Andrew White, Damien Ferraro, Suzanne Clark, Kevin Staley, F. Edward Dude. The use of radiotelemetry to evaluate electrographic seizures in rats with kainate-induced epilepsy. J. Neuro. Meths. 155 (1): 39-48, 2006.

[8] Damien Lapray, Jürgen Bergeler, Erwan Dupont, Oliver Thews, Heiko J. Luhmann. A novel miniature telemetric system for recording EEG activity in freely moving rats. J. Neuro. Meths. 168 (1): 119-26, 2008.

[9] Qizhi Zhang, Zhao Liu, Paul R Carney, Zhen Yuan, Huanxin Chen, Steven N Roper, Huabei Jiang. Non-invasive imaging of epileptic seizures in vivo using photoacoustic tomography. Phys. Med. Biol. 53(7): 1921-1931, 2008.

[10] Bo Wang, Liangzhong Xiang, Max S. Jiang, Jianjun Yang, Qizhi Zhang, Paul R. Carney, Huabei Jiang. Biomed. Opt. Exp. 3(6): 1427–1432, 2012.

[11] E. Z. Zhang, J. G. Laufer, R. B. Pedley, P. C. Beard. In vivo high-resolution 3D photoacoustic imaging of superficial vascular anatomy. Phys. Med. Biol. 54 (4): 1035-1046, 2009.

[12] Jiaying Xiao, Lei Yao, Yao Sun, Eric S. Sobel, Jishan He, Huabei Jiang. Quantitative two-dimensional photoacoustic tomography of osteoarthritis in the finger joints. Opts Exp. 18 (14): 14359-14365, 2010.

[13] W.G Zijlstra , A. Buursma. Spectrophotometry of Hemoglobin: Absorption Spectra of Bovine Oxyhemoglobin, Deoxyhemoglobin, Carboxyhemoglobin, and Methemoglobin. Comparative Biochemistry and Physiology Part B: Biochem. Mol. Biol. 118 (4): 743-749, 1997.

[14] Kliouеva IA, van Luijtelaar EL, Chepurnova NE, Chepurnov SA. PTZ-induced seizures in rats: effects of age and strain. Physiol. Behav. 72 (3):421-426, 2001.
[15] Racine RJ. Modification of seizure activity by electrical stimulation: II. Motor seizure. Electroencephalogr Clin. Neurophysiol. 32 (3): 281–294, 1972.

Simultaneous real-time 3D photoacoustic tomography and EEG for neurovascular coupling study in an animal model of epilepsy

Bo Wang, Junli Zhou, Paul Carney, Huabei Jiang*

Department of Biomedical Engineering
University of Florida

*Corresponding author: hjiang@bme.ufl.edu

***Abstract*—Neurovascular coupling in epilepsy is poorly understood, the study of which requires simultaneous monitoring of hemodynamic changes and neural activity in the brain. Here we for the first time present a combined real-time 3D Photoacoustic tomography (PAT) and electro-physiology/electroencephalography (EEG) system for the study of neurovascular coupling in epilepsy, whose ability was demonstrated with a pentylenetetrazol (PTZ) induced generalized seizure model in rats. Two groups of experiments were carried out with different wavelengths to detect the changes of oxy-hemoglobin (HbO_2) and deoxy-hemoglobin (HbR) signals in the rat brain. We extracted the average PAT signals of the superior sagittal sinus (SSS), and compared them with the EEG signal. Results showed that the seizure process can be divided into three stages. A 'dip' lasting for 1-2 minutes in the first stage and the following hyperfusion in the second stage were observed. The oxy-hemoglobin (HbO_2) signal and the deoxy-hemoglobin (HbR) signal were generally negatively correlated. The change of blood flow was also estimated. All the acquired results here were in accordance with other published results. Compared to other existing functional neuroimaging tools, the proposed method here enables reliable tracking of hemodynamic signal with both high spatial and temporal resolution in 3D, so it's more suitable for neurovascular coupling study of epilepsy.**

I. Introduction

Neurovascular coupling refers to relationship between neuronal activity and hemodynamic related changes in the brain, which are closely coupled in time, spatial, and amplitude. In epileptic seizures, the synchronous excessive neuron discharges caused an enormous increase in the metabolic rate of oxygen, which will place supra-normal demands on the brain's auto-regulatory mechanisms, thus the normal neurovascular coupling can be greatly changed [1, 2]. In order to precisely characterize and understand the mechanisms of neurovascular coupling during seizures, which is still poorly understood, and potentially benefit the predication and diagnosis of epilepsy, simultaneous recording of hemodynamic related signals and neuronal activities is required.

Although some investigators have tried new technologies such as membrane voltage sensitive dye to image the animal cortex [3], EEG still serves as the most common and classic way for neural activity recording [4]. The biggest problem with current practice of the neurovascular coupling study is the lack of an effective way to read out the hemodynamic changes in the whole brain with high spatiotemporal resolution. The disadvantages with currently available neuroimaging technologies that detect the hemodynamic related signals are obvious. Traditional clinical modalities such as functional magnetic resonance imaging (fMRI), positron emission tomography (PET), and single-photon emission computed tomography (SPECT) suffer from their limited spatial and temporal resolutions [5, 6]; while more recently optical mapping methods such as recording of intrinsic signals (ORIS) can only see superficial cortical changes due to the limited penetration depth [7]. Thus there is a growing interest in developing new techniques for neurovascular coupling study, a good understanding of which will in return help the interpretation of the acquired results of these modalities.

Photoacoustic tomography (PAT) is a hybrid method that is capable of imaging optical absorption of tissue through the detection of ultrasound waves generated by a short laser pulse due to transient thermoelastic expansion [8-11]. It enables the label-free vascular imaging with a high signal-to-noise ratio (SNR) by utilizing the optical absorption of hemoglobin as contrast, the primary carrier of oxygen in the blood. Besides, compared with pure optical imaging, it uses less scattered ultrasound as its probing signal and thus offers a much deeper penetration and offers 3D imaging ability with high spatial resolution. With high repetition laser and multi-wavelength method, hemodynamic parameters such as oxy-saturation, total blood volume, and even blood flow can also be detected in real-time. With all these merits, PAT is more suitable for neurovascular study.

PAT can be implemented in many ways, but most of these systems are based on 2D. To get 3D images, mechanical scanning along one direction is needed [8, 9], and the frame rate is limited by the repetition rate of the laser used. Besides, some of these systems will have a limited imaging depth or scanning area [9], while most seizure involves rapid changes of widespread cortical networks in 3D [12]. The most effective way for real-time 3D imaging is to use 2D transducer array with multi-channel acquisition system. Although 2D planar array is easy for fabrication, it has a low transverse resolution due to the limited aperture, and the features with high aspect ratio or with orientations oblique to the transducer surface will suffer from distortion [13]. Comparatively, a spherical array can offer more complete angular views of the object, providing both high resolution and accurate feature definition regardless of shape or location of the object.

Small animal brain imaging is one of the major directions of the PAT, but most works there are mainly focused on vascular structural imaging, tracking single blood vessel

signals, or brain functional mapping [9], and research in epilepsy is relatively rare. PAT in 2D with concurrent EEG for epilepsy study has been reported, but the conclusions in conflict with the existing knowledge may be due to wrong interpretation of the data [14]. Previously, we for the first time reported a sparse spherical array based PAT system operating at a frame rate of 3.3f/s for focused seizure monitoring but without concurrent EEG [10]. Here we modified the system by incorporating EEG system into it for the study of neurovascular coupling of pentylenetetrazol (PTZ) induced generalized seizure in rats. Two groups of experiments were conducted at two different wavelengths to test the combined system, and the acquired PAT and EEG datas were jointly analyzed.

II. MATERIALS AND METHODS

A. System setup

The real-time 3D photoacoustic system has already been reported, and the main feature of this system is the sparse spherical array which is consisted of 192 discrete transducers, as shown in Fig. 1. The transducers were mounted on a custom fabricated white ABS spherical interface with a distance of 71.6mm from the center of the array, and formed into seven layers. Each transducer had a central frequency of 5MHz and a reception bandwidth of greater than 80%, resulting in an almost isotropic spatial resolution about 0.2mm. The active area of the transducer was 3mm in diameter, and the angular acceptance was about 15 degree. The signal from the 192 transducers was amplified by 16 homemade preamplifier boards and coupled into a 64 channel parallel data acquisition system with 3:1 multiplexing, as indicated with three different colors.

Rats were elevated to the center of the spherical interface through a chamber fixed at the tank bottom, whose top was about 15mm beneath the interface center, and a transparent plastic wrap was used to cover the chamber top. Ultrasound gel was used to couple the sound from the animal to the plastic wrap. The ultrasonic transducer array with the spherical interface, placed in the water bath, was therefore acoustically coupled to the mouse tissues. The laser light was delivered through a concave lens giving a homogenous illumination on the head of the rat. In this study, two wavelengths were used, 1064nm and 710nm. The 1064nm light was from a pulsed Nd:YAG (5~20ns pulse width), and the 710nm light was from a Q-switched Nd:YAG pumped Ti:sapphire laser. The final laser intensity on the rat head was about 50mJ/cm^2 for 1064nm, and 4mJ/cm^2 for 710nm, all below the ANSI exposure limits. Both the two lasers operate at 10Hz, so that the system could record one complete set of 3D PAT data in 0.33s.

Two injection needles, inserted into the front cortex of rat brain about 3mm below the scalp, were served as EEG electrodes as shown in Fig. 1(b). One electrode was picked for reference and ground signal, while the other electrode was to record EEG signal. The EEG signal was amplified (RA16PA, TDtucker-Davis Tech.) and recorded (RZ5 Bioamp Processor, TDtucker-Davis Tech.) with a sampling rate about 50kHz. Both the two electrodes were firmly glued on the rat head and the wires were tightly attached to the animal holder using glue tapes, so as to avoid noise induced by any possible unnecessary movement of the rat or experiment operators. The PAT system gave an output synchronized signal to the EEG system, so that the two systems were well synchronized.

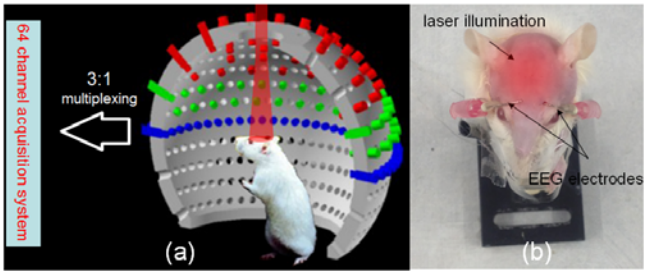

Figure 1. Experimental setup of the combined system. (a) Schematic of the photoacoustic system; (b) Rat with two electrodes in the brain; and the laser illumination is also indicated

B. Animal preparation

Two groups of rats (n=16 rats, each about 35~45g, with 8 rats for 1064nm and the other 8 rats for 710nm) were used. The rats were anaesthetized with about 0.25ml Urethane (0.25g/mL) and got hair on the head shaven. Before mounting the rats on the homemade plastic holder, a syringe containing 0.04g/ml PTZ with a scalp needle was inserted in the abdomen and fixed with glue. PTZ was used to induce generalized seizure in rat brain, which has already been established [15]. Then the two electrodes were inserted, and the rats were elevated into the transducer array center of the photoacoustic system for scanning. Each experiment lasted 25min, and PTZ was administrated with a dose of 0.5mL at 5min. All rats were kept alive through the experiment. All the animal procedures performed were in accordance with the approved University of Florida IACUC protocols.

C. Data processing

With a frame rate of 3.3f/s, 5000 complete sets of PAT data were recorded. Before doing 3D reconstruction and processing, 2D PAT images were reconstructed with data collected by the 64 transducers in the lowest layer of the array, which were indicated with blue in Fig. 1. The 2D images were carefully checked to avoid the possible motion artifact induced by the movement of the rat head during the experiment. 3D images were calculated using delay&sum algorithm, which was accelerated by GPU parallel technique. Then the negative pixel values in were set to zero. Each set of the reconstructed 3D images had a voxel number of 201×201×101 representing a 10×10×5mm^3 volume, which could be calculated in 0.97s. Amira (from Visage Imaging, Inc.) was used to render the 3D images.

There were two sources of noise in the EEG signal, a strong sharp 10Hz noise from the Q-switch of the laser, and the 60Hz alternating current noise. For de-noising, the deteriorated data by the Q-switch was replaced with adjacent data, and the 60Hz alternating current noise was removed by filtering out 58-62Hz in frequency domain (Fig. 2). Then the EEG data was applied with a low pass filter of 100Hz, and

transformed into a 300000 point signal for the 25min EEG recording, corresponding to sampling rate of 200Hz.

For neurovascular coupling study, we first extracted the averaged PAT signals of the superior sagittal sinus (SSS) of each rat from the reconstructed 3D images and compared it with the corresponding EEG signal. We choose the PAT signals of the SSS because it has the highest SNR and is highly distinguishable in the reconstructed 3D image. Because 1064nm and 710nm are mainly absorbed by oxy-hemoglobin (HbO_2) and deoxy-hemoglobin (HbR), the acquired results for these two wavelengths can be taken as the changes of HbO_2 and HbR respectively [16]. All the acquired results were examined by experts in the neurology.

III. RESULTS

A. *Data preprocessing*

Representative time frames of 2D images through the experiment are displayed in Fig. 2(a) with a time interval of 1min, compared with a rat brain photo taken after the experiment (Fig. 2(b)). Although the image quality is not excellent due to the limited transducer positions (only 64 transducers are averaged once), the SSS and two transverse sinuses (TS) are clearly reconstructed, and some other small blood vessels are also revealed. In Fig. 2(a) it is observed that there is no palpable shift of the rat brain which is a prerequisite for the following data processing. In our experiments, 3 out of 8 rats with 1064nm moved, but all the rats in the second group remained still. We also notice that it's hard to tell when the seizure begins just by eyes from these 2D images, so quantitative analyze is needed.

EEG signals were recorded to confirm the onset, duration, and morphology of the seizure, which is shown in Fig. 3(a). The EEG signal is stable before the drug injection at 5min, when isolated high amplitude spikes can be easily seen in the EEG signal. After this spontaneous fast discharges begin to show and increase in amplitude in the following 2 to 3 minutes. The seizure onset comes about 142 ± 45s after the drug injection, which is defined to be the first signal that exceeds 6 times the standard deviation (SD) of the baseline (the average signal in the first 4min). As the seizure evolves, the firing frequency generally gets lower, but the EEG signal begins to decrease in and keeps firing through the experiment. Fig. 3(b) shows the EEG signal in a short time window (blue), compared with the original data before preprocessing (red). We can see that both the noises from the Q-switch and the alternating power supply are removed.

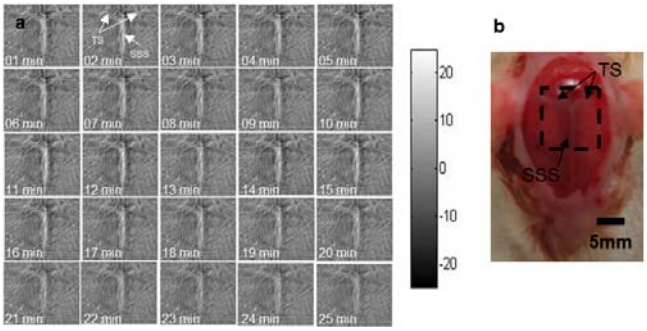

Figure 2. Representative time frames of 2D PAT images of the rat brain, compared with an anatomical image. (a) Representative time frames of 2D PAT images of the rat brain with 1064nm. The time interval is 1min, and each image covers $10 \times 10 mm^2$ with 201×201 pixels. (b) Photo of rat brain with hair and scalp being removed. The SSS, TS, and the reconstruction area is indicated. Scale bar is 5mm through the figure.

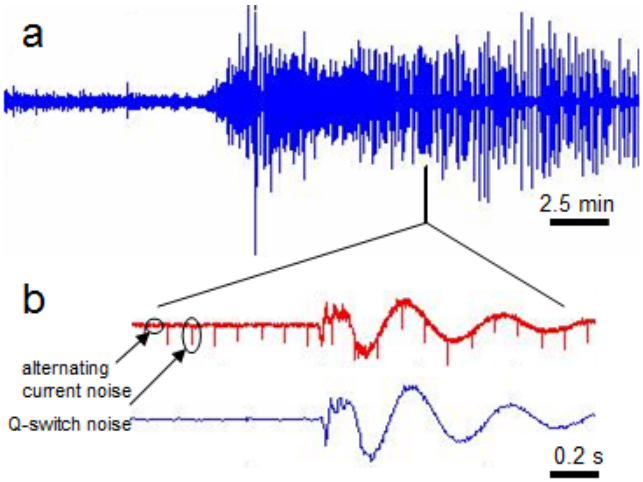

Figure 3. EEG signal for PTZ-induced seizure. (a) Typical EEG signal after processing. (b) The original (blue) and processed (red) EEG signal in a short time wiondow..

B. *3D image reconstruction*

Fig. 4 shows the reconstructed 3D images from different views. The reconstructed volume is 10 x 10 x $5mm^3$ with a 0.05mm voxel size. Similar to the 2D images, the SSS and TS can be clearly revealed both in the 3D images of HbO_2 and HbR, although the SNR of HbR is not as good as that of HbO_2 due to relatively low laser intensity of 710nm, as well as the low concentration of HbR in the blood vessels compared to that of HbO_2. It is also noticed that in the 3D images of HbO_2, we can see the Ostia end of the straight sinus (SS) below the SSS which can not be seen in the 2D images. All these demonstrate the excellent positioning ability of our 3D PAT system.

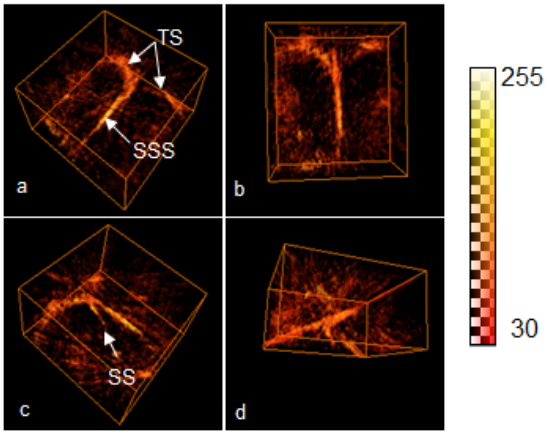

Figure 4. Reconstructed 3D PAT images of the rat brain with 1064nm from different views. SSS, TS, and SS can be seen in the image. The image domain is $10 \times 10 \times 5mm^3$ with $201 \times 201 \times 101$ pixels. Colarbar is indicated.

C. *Neurovascular coupling study*

For each set of PAT data, the average signal in a ROI that could enclose the SSS was extracted and taken as the change of the SSS (Fig. 5(a) and Fig. 5(b)), which was further converted into percentage changes to the baseline. For all the rat datas analyzed (n=14), the EEG signals looked the same in shape and timing (Fig. 5(c) and Fig. 5(d)). This means our PTZ induced generalized seizure modal is quite stable and the drug administration is well controlled, so that all the rat results are comparable. The two PAT curves in Fig. 5(c) and Fig. 5(d) are also representatives. The PAT signals for HbR is smoothed using a moving window of 3 seconds to improve the SNR. The neurovascular coupling of our rat model can be obtained by comparing these two groups of PAT curves and the corresponding EEG signals.

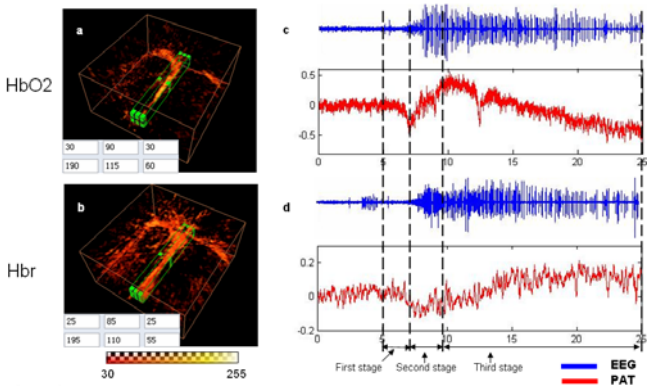

Figure 5. Typical results for HbO_2 (a and c) and HbR (b and d) respectively, with the ROI for the SSS indicated in the 3D PAT images. The reconstruction domain for the 3D images (a and c) are $10\times10\times5mm^3$ with $201\times201\times101$ pixels. c and d are the EEG and PAT signals of SSS for a and b respectively. The EEG signals (blue line) are in arbitrary units, and the PAT curves (red line) are represented as the change with respect to the baseline. The whole seizure process after the injection of PTZ can be divided into three stages. The PAT signal for HbR has been smoothed using a moving window of 3 seconds. The time units in c and d is minutes.

Both the EEG and PAT signals in these two datas remain quite stable before the drug injection. After that the time course of the experiment can be generally divided into three stages, as indicated. In the first stage, the EEG signal increases in amplitude as seizure initiates. At the same time, there's a prominent sudden decrease in the HbO_2 signal while the HbR signal just slightly increases. This indicates that for this period of time, the increase of blood supply was inadequate for the metabolism of neurons. In the second step, we can see that the EEG signals continue to increase as the seizure evolves. However, the HbO_2 signal begins to increase and the HbR begins to decrease at the same time. Thus we conclude that the blood supply is greatly increased due to dilation of arteries and increasing of blood flow. In the third step, although the EEG signal gradually decreases in firing frequency, the HbO_2 signal is still decreased, while the HbR signal increases. This means the blood flow is decreased.

Through the whole seizure process, we see the coincidence that the two PAT signals are well negatively correlated. When the HbO_2 reaches its peak the HbR just drops to its minimum, or otherwise. To make it more convincing, we calculate the average changes of HbO_2 and HbR across all the rat experiments, as shown in Fig. 6. The two curves there are achieved by first normalizing the data in a single experiment to the baseline, and then averaging the data of all rats in the same group. The final data are further averaged every 30secs, with the corresponding SD indicated. The correlation coefficient of these two signals is calculated to be -0.705.

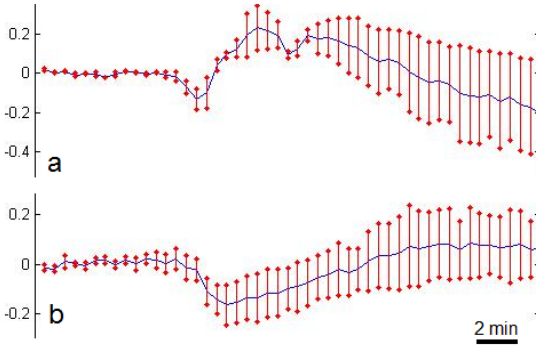

Figure 6. Full timecourses of mean percent changes of the HbO_2 (a) and HbR (b) signals, which are negatively correlated with each other. The SD for each signal is indicated every 30s. Vertical bar represents the amplitude of the PAT signal changes to the baseline.

IV. DISCUSSION

Neurovascular coupling study of epilepsy requires simultaneous recording of neuronal activity and macroscopic hemodynamic signals in the brain, bringing significant challenges in terms of experimental paradigm and instrument performance. We successfully integrated the EEG system into our real-time 3D PAT system that is based on a 64-channel parallel data acquisition system and a spherical transducer array, and realized the simultaneous recording of neuron activity and hemodynamic signal in the whole rat brain over the entire epileptic seizure process.

The neurovascular coupling of the intraperitoneal PTZ rat model here is studied with the HbO_2 and HbR signals of the SSS. PTZ has been used experimentally to induce generalized seizure, where hemodynamic changes can be found all over the brain [17]. As one of the main blood vessels in the brain, SSS is highly involved in the PTZ-induced seizures. When the seizure begins, we observed a sudden decrease in HbO_2 for 1 to 2 minutes, followed by a dramatic increase. The 'dip' observed here is much similar to the reported 'epileptic dip' with ORIS, but found on the cerebral cortex. It's different from the 'initial dip' which only lasts several seconds. In the second stage of the seizure, the HbO_2 signal keeps on increasing and finally succeeds the baseline, which supports the idea that the increase of cerebral blood flow oversupplies the increased metabolic demands of the neurons in epileptic seizures. And the negative correlation we observed between the HbO_2 and HbR signals in SSS here can be explained by the fact that the veins don't usually dilate as much as the arteries.

There are limitations in our work. We only studied the PAT signals of SSS, but in-depth information of the vascular coupling is more embedded in the local hemodynamic changes. Thus the signals of different regions in the brain

tissue need to be extracted, based on which, the neural network analysis can be carried out.

V. CONCLUSION

We for the first time present a combined real-time 3D PAT and EEG system to study the neurovascular coupling of epilepsy, which is demonstrated using a PTZ induced generalized seizure model in rats. PAT data was collected at two different wavelengths, and average PAT signals of SSS were compared with the corresponding EEG signals. We find a long time 'dip' in the HbO_2 signal at the seizure beginning, followed by a profound increase, and the HbO_2 and HbR signals are negatively correlated. All these are in accordance with other published results. This indicates that our system is capable for the non-invasive neurovascular coupling of epilepsy in small animal brain.

This research was supported in part by a grant from the US Department of Defense Congressionally Directed Medical Program.

REFERENCES

[1] Browne TR, Holmes GL. Epilepsy. New Engl J. Med. 344 (15): 1145-51, 2001.

[2] Theodore H. Schwartz. Neurovascular Coupling and Epilepsy: Hemodynamic Markers for Localizing and Predicting Seizure Onset. Epilepsy Curr. 7 (4): 91–94, 2007.

[3] Hongtao Ma, Mingrui Zhao, Theodore H. Schwartz. Dynamic Neurovascular Coupling and Uncoupling during Ictal Onset, Propagation, and Termination Revealed by Simultaneous In Vivo Optical Imaging of Neural Activity and Local Blood Volume. Cereb Cortex. 23 (4): 885-899, 2013.

[4] Theodore H. Schwartza, Seung-Bong Hongb, Andrew P. Bagshawc, Patrick Chauveld, Christian-G. Bénar. Preictal changes in cerebral haemodynamics: Review of findings and insights from intracerebral EEG. Epilepsy Research. 97: 252-266, 2011.

[5] Tyvaert L., LeVan P., Dubeau F., Gotman J. Noninvasive dynamic imaging of seizures in epileptic patients. Hum. Brain Mapp., 30: 3993-4011, 2009.

[6] Van Paesschen W., Dupont P., Sunaert S., Goffin K., Van Laere K. The use of SPECT and PET in routine clinical practice in epilepsy. Curr. Opin. Neurol., 20 (2): 194-202, 2007.

[7] Zhao M., Suh M., Ma H., Perry C., Geneslaw A., Schwartz T.H. Focal increases in perfusion and decreases in hemoglobin oxygenation precede seizure onset in spontaneous human epilepsy. Epilepsia, 48: 2059-2067, 2007.

[8] Qizhi Zhang, Zhao Liu, Paul R Carney, Zhen Yuan, Huanxin Chen, Steven N Roper, Huabei Jiang. Non-invasive imaging of epileptic seizures in vivo using photoacoustic tomography. Phys. Med. Biol. 53 (7): 1921-1931, 2008.

[9] E.Z. Zhang, J.G. Laufer, R.B. Pedley, P.C. Beard. In vivo high-resolution 3D photoacoustic imaging of superficial vascular anatomy. Phys. Med. Biol. 54 (4): 1035-1046, 2009.

[10] Bo Wang, Liangzhong Xiang, Max S. Jiang, Jianjun Yang, Qizhi Zhang, Paul R. Carney, Huabei Jiang. Photoacoustic tomography system for noninvasive real-time three-dimensional imaging of epilepsy. Biomed. Opts. Exp. 3 (6): 1427–1432, 2012.

[11] Jiaying Xiao, Lei Yao, Yao Sun, Eric S. Sobel, Jishan He, Huabei Jiang. Quantitative two-dimensional photoacoustic tomography of osteoarthritis in the finger joints. Opts. Exp. 18 (14): 14359-14365, 2010.

[12] Kramer MA, Eden UT, Kolaczyk ED, Zepeda R, Eskandar EN, Cash SS. Coalescence and fragmentation of cortical networks during focal seizures. J. Neurosci. 30: 10076-10085, 2010.

[13] S. Manohar, A. Kharine, J. Hespen, W. Steenbergen, T. Leeuwen. Photoacoustic mammography laboratory prototype: imaging of breast tissue phantoms. J. Biomed. Opt. 9 (6): 1172-1181, 2004.

[14] V. Tsytsarev, Bi. Raoa, K. Maslova, L. Li, L.V. Wang. Photoacoustic and optical coherence tomography of epilepsy with high temporal and spatial resolution and dual optical contrasts. J. Neurosci. Meths. 216: 142-145, 2013.

[15] Kliouеva IA, van Luijtelaar EL, Chepurnova NE, Chepurnov SA. PTZ-induced seizures in rats: effects of age and strain. Physiol. Behav. 72 (3):421-426, 2001.

[16] W.G. Zijlstra, A. Buursma. Spectrophotometry of Hemoglobin: Absorption Spectra of Bovine Oxyhemoglobin, Deoxyhemoglobin, Carboxyhemoglobin, and Methemoglobin. Comparative Biochemistry and Physiology Part B: Biochemistry and Molecular Biology. 118 (4): 743-749, 1997.

[17] N. Camp, R. Hooge, M. Verhoye, R. Peeters, P. Deyn, and A. Linden. Simultaneous electroencephalographic recording and functional magnetic resonance imaging during pentylenetetrazol-induced seizures in rat. Neuro Image 19: 627–636, 2013.